Q-SORT

Q-SORT International Conference on Quantum Imaging and Electron Beam Shaping

Tuesday 2 — Friday 5 July 2019

Max Planck Institute for the Science of Light

Staudtstraße 2
91058 Erlangen
Germany

This project has received funding from the European Union's Horizon 2020 research and innovation programme under Grant Agreement No. 766970

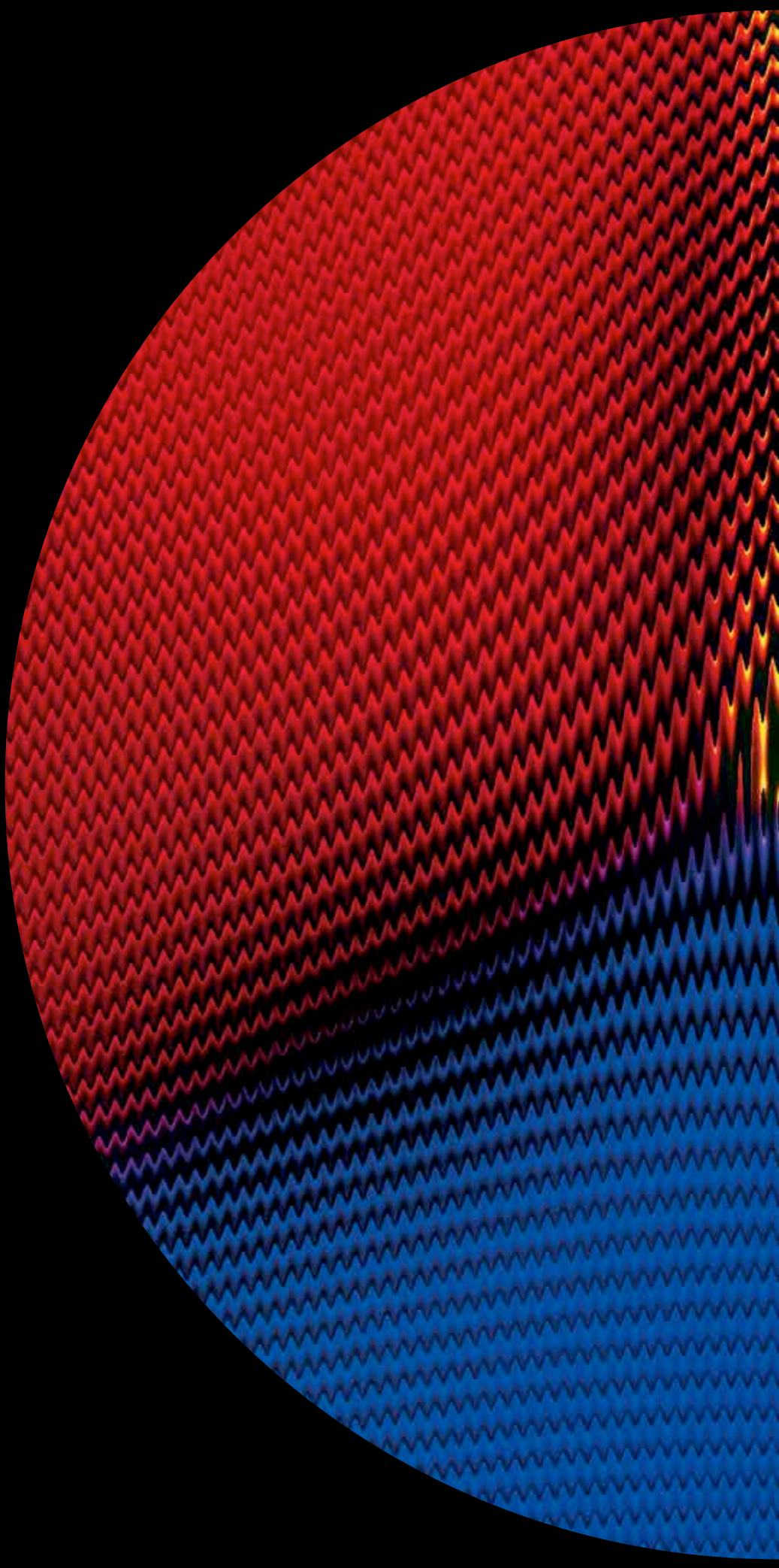

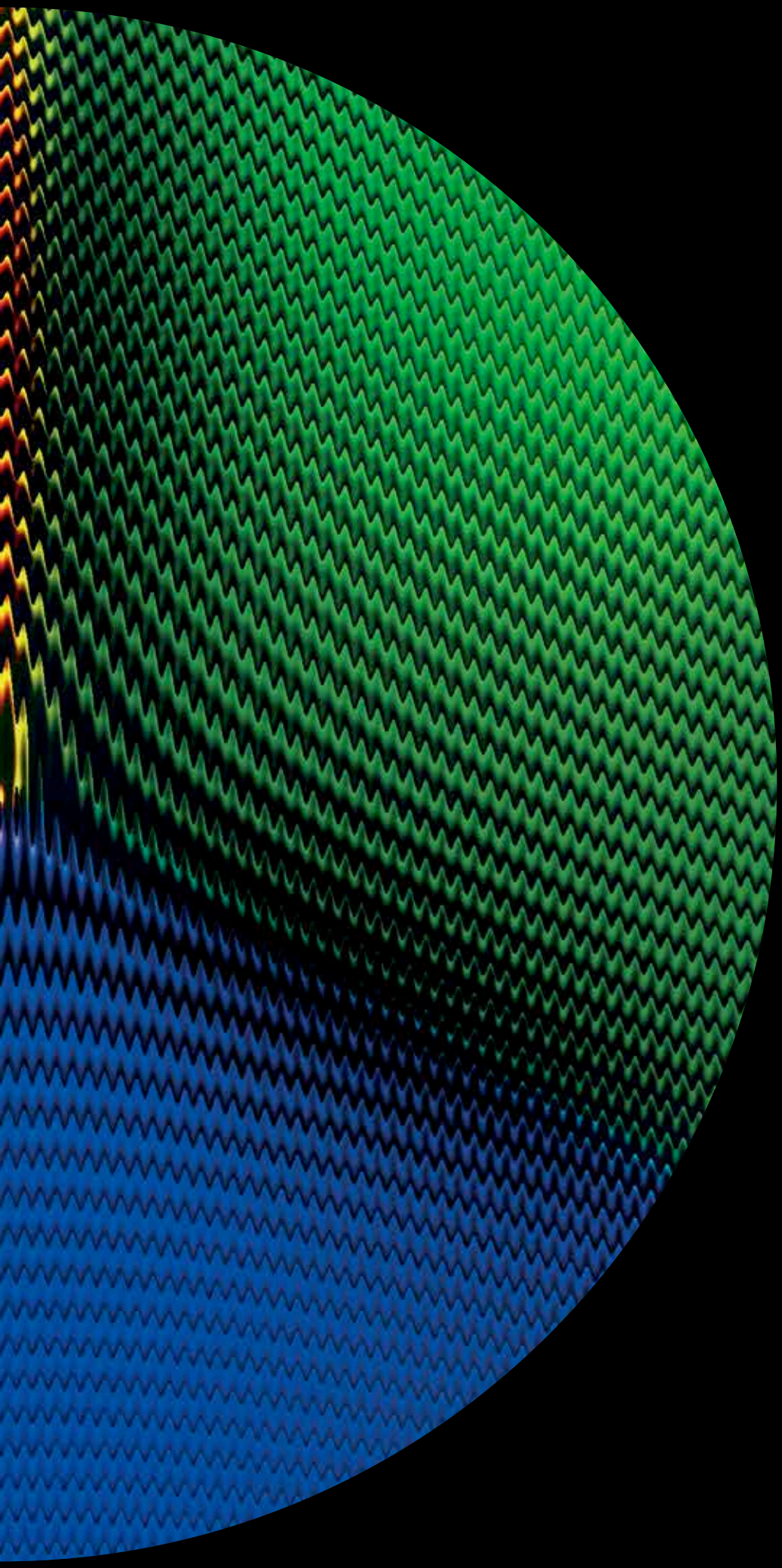

Table of contents:

Index

Programme

Abstracts

Programme

Tuesday 2 July

Leuchs-Russell Auditorium
Max Planck Institute for the Science of Light
Staudtstraße 2 — 91058 Erlangen — Germany

14:00 — 14:30	Registration	
14:30 — 15:00	Welcome and Institutional Delegates	
	Keynote Speech: **1st Q-SORT Webinar**	***Chair:*** *Gerd Leuchs* *Max Planck Institute for the Science of Light (Germany)*
15:00 — 16:00	Design and potential applications of patterned electron mirrors	*Pieter Kruit* *Delft University of Technology (The Netherlands)*
16:0 — 16:30	Coffe Break	
	Special Seminar	***Chair:*** *Rafal Dunin-Borkowski* *Forschungszentrum Jülich GmbH (Germany)*
16:30 — 17:15	Making open science work for you	*Najla Rettberg* *University of Gottingen (Germany) /* *Tim Smith* *CERN (Switzerland)*
	Session A: **Phase effects in inelastic scattering (Plasmons)**	***Chair:*** *Gerd Leuchs* *Max Planck Institute for the Science of Light (Germany)*
17:15 — 17:35	A1 — Innovative 4D STEM approaches towards mapping transient electrical fields and strain at the nanoscale	*Giulio Guzzinati* *University of Antwerp (Belgium)*
17:35 — 18:00	A2 — Orbital angular momentum and energy loss characterization of plasmonic excitations in metallic nanostructures in TEM	*Matteo Zanfrognini* *University of Modena and Reggio Emilia (Italy)*
18:00 — 18:25	A3 — Dihedral plasmonics: from optical skyrmions to novel spin-orbit interaction of light	*Shai Tsesses* *Technion, Israel Institute of Technology (Israel)*

Wednesday 3 July

Leuchs-Russell Auditorium
Max Planck Institute for the Science of Light
Staudtstraße 2 — 91058 Erlangen — Germany

8:30 — 9:00	Registration	
	Session B: **Quantum Imaging**	***Chair:*** *Pieter Kruit* *Delft University of Technology (The Netherlands)*
9:00 — 9:15	B1 — Quantum correlations in electron microscopy	*Chen Mechel* *Technion, Israel Institute of Technology (Israel)*
9:15 — 9:30	B2 — Implementing Conditional Re-illumination for Low-Damage Electron Microscopy	*Akshay Agarwal* *Massachusetts Institute of Technology (USA)*
9:30 — 9:45	B3 — Improving Image Contrast with 2-Pass Electron Microscopy	*Navid Abedzadeh* *Massachusetts Institute of Technology (USA)*
9:45 — 10:00	B4 — Spiral Phase Contrast Imaging in Cryo-Electron Microscopy	*Yue Zhang* *Maastricht University (The Netherlands)*
10:00 — 10:15	B5 — A proposal for a basis change paradigm to optimally look at proteins	*Vincenzo Grillo* *National Research Council (Italy)*
10:15 — 10:30	B6 — Structured detection and structured illumination in constant-dose particle counting experiments	*Wouter Van den Broek* *Humboldt University of Berlin (Germany)*
10:30 — 10:45	B7 — Atomic Resolution Dynamics for Soft-Materials: from Low Dose to Interaction-Free “Electron Microscopy"?	*Fu-Rong Chen* *National Tsing Hua University (Taiwan)*
10:45 — 11:15	Coffe Break	
	Keynote Speech: **2nd Q-SORT Webinar**	***Chair:*** *Vincenzo Grillo* *National Research Council (Italy)*
11:15 — 12:15	Quantum aspects of the interaction between beam electrons and optical near fields	*Javier García de Abajo* *ICFO, The Institute of Photonic Sciences (Spain)*
12:15 — 13:15	Lunch	
	Session C: **Time-resolved and near-field excitation**	***Chair:*** *Avraham Gover* *Tel Aviv University (Israel)*
13:15 — 13:40	C1 YR — Quantum coherent optical transverse and longitudinal shaping of free electron beams	*Armin Feist* *University of Göttingen (Germany)*
13:40 — 14:05	C2 YR — Polarization-controlled photon-induced near-field electron microscopy	*Tyler Harvey* *University of Göttingen (Germany)*

Leuchs-Russell Auditorium
Max Planck Institute for the Science of Light
Staudtstraße 2 — 91058 Erlangen — Germany

14:05 — 14:30	C3 YR — Sub-cycle electron pulse shaping with terahertz control fields	*Dominik Ehberger* *Ludwig Maximilian University of Munich (Germany)*
14:30 — 14:55	C4 YR — Ultrafast coherent manipulation of a free-electron wave function by electron-light quantum interaction	*Giovanni Maria Vanacore* *Swiss Federal Institute of Technology in Lausanne (Switzerland)*
	Keynote Speech: **3rd Q-SORT Webinar** **1st Q-SORT Women in Science Lecture Series**	***Chair:*** *Vincenzo Grillo* *National Research Council (Italy)*
15:00 — 16:00	Coherent control of single electron wave packets with light and nanostructures	*Nahid Talebi* *Max Planck Institute Solid State Research (Germany)*
16:00 — 16:30	Coffe Break	
	Session D: **Beam Shaping**	***Chair:*** *Ebrahim Karimi* *University of Ottawa (Canada)*
16:30 — 16:55	D1 YR — Optimizing blazed efficiency of electron diffractive optics with ion beam gas-assisted etching for structured electron spectroscopy	*Cameron Johnson* *University of Oregon (USA)*
16:55 — 17:10	D2 YR — Tuning of off-axis vortex beam using Pancharatnam-Berry phase	*Philip Jacob* *Indian Institute of Technology Kharagpur (India)*
17:10 — 17:25	D3 YR — Realization of a holographic fan-out e-beam OAM sorter	*Paolo Rosi* *University of Modena and reggio Emilia (Italy)*
17:25 — 17:40	D5 YR — The role of spatial coherence for the creation of and imaging with atom size electron vortex beams	*Darius Pohl* *Dresden University of Technology (Germany)*
17:40 — 17:55	D6 YR — Wavefront modulation by inverted Gabor holography	*Tatiana Latychevskaia* *University of Zurich (Switzerland)*
	SL **Round Table**	***Chair:*** *Vincenzo Grillo* *National Research Council (Italy)*
17:55 — 18:55	How much information can a quantum system carry?	*Ebrahim Karimi* *University of Ottawa (Canada)*
19:00	Social Dinner: Kitzmann Bräuschänke	Südliche Stadtmauerstraße 25, 91054 Erlangen

Thursday 4 July

Leuchs-Russell Auditorium
Max Planck Institute for the Science of Light
Staudtstraße 2 — 91058 Erlangen — German

8:30 — 9:00	Registration	
	Session E: **Phase Plates**	***Chair:*** *Pieter Kruit* *Delft University of Technology (The Netherlands)*
9:00 — 9:25	E1 YR — A programmable phase patterning device for electron beams	*Stewart Koppell* *Stanford University (USA)*
9:25 — 9:50	E2 YR — Design and implementation of a tunable phase plate for electron microscopy based on Ampere's law	*Peng-Han Lu* *Forschungszentrum Jülich GmbH (Germany)*
9:50 — 10:05	E3 — Towards an electrostatic OAM sorter	*Amir Tavabi* *Forschungszentrum Jülich GmbH (Germany)*
10:05 — 10:20	E4 — Progress on the realization of a pixelated programmable phase plate for electrons	*Armand Béché* *University of Antwerp (Belgium)*
10:20 — 10:35	E5 — Nanofabrication of spiral phase plate for electron microscopy	*Stefano Frabboni* *University of Modena and Reggio Emilia (Italy)*
10:35 — 10:50	E6 — Optimal electrode design for programmable phase plates for use in electron microscopes	*Helmut Soltner* *Forschungszentrum Jülich GmbH (Germany)*
10:50 — 11:30	Coffe Break	

Heinrich-Schliemann Gymnasium
Königstraße 105 — 90762 Fürth — Germany

	Q-SORT Science Bash ***(Outreach event for schools)***	
11:20 — 12:30	Does God Play Dice?	*Miles Padgett* *Glasgow University (United Kingdom)*

Leuchs-Russell Auditorium
Max Planck Institute for the Science of Light
Staudtstraße 2 — 91058 Erlangen — Germany

	Session F: **Cathodoluminescence**	***Chair:*** *Vincenzo Grillo* *National Research Council (Italy)*
11:30 — 11:45	F1 — High spectral resolution EELS and CL to probe optical properties at the nanometer scale	*Luiz Tizei* *French National Center for Scientific Research (France)*
11:45 — 12:00	F2 — Time-, and phase-resolved cathodoluminescence spectroscopy	*Albert Polman* *AMOLF (The Netherlands)*
12:00 — 12:15	F3 — FEL: quantum effects in phase space	*Moritz Carmesin* *University of Ulm (Germany)*
	Session G: **Electron-Light Interaction**	***Chair:*** *Peter Hommelhoff* *University of Erlangen-Nuremberg (Germany)*
12:15 — 12:40	G1 — Spontaneous radiation from a wide quantum electron beam	*Aviv Karnieli* *Tel Aviv University (Israel)*
12:40 — 12:55	G2 — Towards a quantum electron microscope: microwave based interferometer and resonator for electrons	*Robert Zimmermann* *University of Erlangen–Nürnberg (Germany)*
13:00 — 14:00	Lunch	
	Session G: **Electron-Light Interaction (Continued)**	
14:00 — 14:25	G3 — Sub-relativistic electrons in dielectric acceleration and ultrafast interactions	*Roy Shiloh* *University of Erlangen–Nürnberg (Germany)*
14:25 — 14:40	G4 — Towards direct imaging of GHz magnetic dynamics with sub-100-nm resolution in a transmission electron microscope	*Yoshie Murooka* *Forschungszentrum Jülich GmbH (Germany)*
14:40 — 14:45	G5 — Controlled generation of higher order vortex arrays using a Microlens Array	*B.S. Harshith* *Indian Institute of Science Education Research Pune (India)*
	SL **Roundtable**	***Chair:*** *Gerd Leuchs* *Max Planck Institute for the Science of Light (Germany)*
14:45 — 15:45	When only one pixel is more	*Miles Padgett* *Glasgow University (United Kingdom)*
15:45 — 16:15	Cofee Break	

Thursday 4 July (Continued)

Foyer on 1st floor
Max Planck Institute for the Science of Light
Staudtstraße 2 — 91058 Erlangen — Germany

16:15 — 18:30 **Poster Exhibition**

Chair: *Enzo Rotunno*
National Research Council (Italy)

P1 — Control of free electrons in the vicinity of dielectric nanostructures
Norbert Schönenberger
University of Erlangen–Nürnberg (Germany)

P2 — Structured detection and structured illumination in constant-dose particle counting experiments
Wouter Van den Broek
Humboldt University of Berlin (Germany)

P3 — Tuning of Off-axis Vortex Beam using Pancharatnam-Berry Phase
Philip Jacob
Indian Institute of Technology Kharagpur (India)

P4 — High spectral resolution EELS and CL to probe optical properties at the nanometer scale
Luiz Tizei
French National Center for Scientific Research (France)

P5 — Controlled generation of higher order vortex arrays using a Microlens Array
B.S. Harshith
Indian Institute of Science Education Research, Pune (India)

P6 — A proposal for a basis change paradigm to optimally look at proteins
Vincenzo Grillo
National Research Council (Italy)

P7 — Orbital angular momentum and energy loss characterization of plasmonic excitations in metallic nanostructures in TEM
Matteo Zanfrognini
University of Modena and Reggio Emilia (Italy)

P8 — Nanofabrication of spiral phase plate for electron microscopy
Stefano Frabboni
University of Modena and Reggio Emilia (Italy)

P9 — Electron magnetic chiral dichroism using the orbital angular momentum sorter
Enzo Rotunno
National Research Council (Italy)

P10 — Design and implementation of a tunable phase plate for electron microscopy based on Ampere's law
Peng-Han Lu
Forschungszentrum Jülich GmbH (Germany)

Bibliothek Room
Max Planck Institute for the Science of Light
Staudtstraße 2 — 91058 Erlangen — Germany

16:15 — 18:30 | **Wikipedia Edit-a-thon**

Chair: *Alessandro Marchetti*
Expert Wikimedia User and Researcher (Italy)

Friday 5 July

Leuchs-Russell Auditorium
Max Planck Institute for the Science of Light
Staudtstraße 2 — 91058 Erlangen — Germany

8:30 — 9:00	Registration	
	Keynote Speech: **4th Q-SORT Webinar**	***Chair:*** *Peter Hommelhoff* *University of Erlangen - Nuremberg (Germany)*
9:00 — 10:00	The reality of the quantum electron wavefunction in interactions with light and matter	*Avraham Gover* *Tel Aviv University (Israel)*
10:00 — 10:30	Cofee Break	
	Session H: **Phase effects in inelastic scattering EMCD**	***Chair:*** *Pieter Kruit* *Delft University of Technology (Germany)*
10:30 — 10:55	H1 YR — Vortex filter EMCD: experimental evidence and for sub nanometre resolution	*Thomas Schachinger* *Vienna University of Technology (Austria)*
10:55 — 11:10	H3 — Electron magnetic chiral dichroism using the orbital angular momentum sort	*Enzo Rotunno* *National Research Council (Italy)*
11:10 — 11:25	H4 — Atomic-plane-resolved electron magnetic chiral dichroism using a defocused electron beam	*Dongsheng Song* *Forschungszentrum Jülich (Germany)*
11:25 — 11:40	H5 — A simple procedure for the optimization of classical electron magnetic circular dichroism measurements	*Sebastian Schneider* *Leibniz Institute for Solid State and Materials Research in Dresden (Germany)*
	Session I: **Electron-Light Interaction**	***Chair:*** *Nahid Talebi* *Max Planck Institute Solid State Research (Germany)*
11:40 — 11:55	I1 — Attosecond electron bunch creation in optical traveling waves via ponderomotive scattering	*Norbert Schönenberger* *Friedrich–Alexander University Erlangen–Nürnberg (Germany)*
11:55 — 12:10	I2 — Quantized interaction of free electrons with cavity photons stimulated by pJ laser pulses	*Kangpeng Wang* *Technion-Israel Institute of Technology (Israel)*
12:10 — 12:25	I3 — The classical-to-quantum transition of measurements from linear particle accelerators to photon-induced near-field electron microscopy	*Yiming Pan* *Weizmann Institute of Science (Israel)*

Leuchs-Russell Auditorium
Max Planck Institute for the Science of Light
Staudtstraße 2 — 91058 Erlangen — Germany

12:25 — 12:40 **Thermofisher Best Poster Award**

Chair: *Peter Tiemeijer*
Thermofisher (The Netherlands)

- Concluding Remarks

Gerd Leuchs, Max Planck Institute (Germany)
Vincenzo Grillo, National Research Council (Italy)

12:45 — 13:45 Lunch

Bibliothek Room
Max Planck Institute for the Science of Light
Staudtstraße 2 — 91058 Erlangen — Germany

13:40 — 18:30 **Wikipedia Edit-a-thon**

Chair: *Alessandro Marchetti*
Expert Wikimedia User and Researcher (Italy)

Abstracts

by first author

Improving Image Contrast with 2-Pass Electron Microscopy

N. Abedzadeh[1], C-S. Kim[2], A. Agarwal[1], J. Simonaitis[1], M. Turchetti[1], M. Kasevich[3], K.K. Berggren[1]

[1]MIT, Cambridge, MA, USA
[2]Samsung group, South Korea
[3]Stanford University, Stanford, CA, USA
E-mail: navid@mit.edu

Introduction

Multipass electron microscopy is envisioned to provide increased signal-to-noise ratio (SNR) compared to conventional phase-contrast imaging for a given amount of beam-damage to the sample [1]. In this scheme, a phase object such as a biological sample placed in between two electron mirrors is illuminated M times with the same electrons confined in this electron cavity. Every pass through the sample leads to additional phase accumulation and hence contrast enhancement. As such, demonstration of multipass electron microscopy is perhaps best performed inside a modified TEM at high acceleration voltages (e.g. 200 keV). However, due to various challenges, the most significant of which being the inaccessibility of high-voltage electron mirrors to form the cavity, such an experiment is not trivial. We are currently involved in a collaborative effort towards the construction of a lower-energy (10 keV) analog of this TEM experiment[*]. In the meantime, however, a carefully designed experiment inside an SEM, may reveal the first signs of electron phase accumulation after passing through a sample twice (M=2). This experiment would involve a thin nanofabricated phase-grating placed at the image plane of a tetrode electron mirror inside an SEM. Operating under two-beam condition, observation of increased relative signal intensity in the first-order diffraction spot after two passes would point towards phase accumulation due to M=2 multipassing. Analysis of beam-induced damage, however, requires more elaborate experiments. We propose an experiment involving the use of electron-sensitive resist as the sample and the consequent measurement of line-edge roughness after resist development as a proxy for shot noise.

Experimental design

A complete demonstration of multipass electron microscopy must address two aspects: (1) increased image contrast due to additional phase accumulation, (2) reduced beam-induced damage for a fixed SNR. In this section, we address these two aspects in two separate proposed experiments.

Figure 1a shows a schematic of the proposed experiment for demonstration of multipassing in SEM. An electrostatic tetrode electron mirror is placed inside an SEM with its optical axis aligned to that of the SEM objective lens. A nanofabricated phase grating (sample) is placed below the objective lens and overlapping the image plane of the tetrode mirror. The electron beam, focused by the objective lens, would be incident on the phase grating oriented

[*] The Quantum Electron Microscopy (QEM) project is a collaborative effort between Stanford University, MIT, University of Erlangen, and TU Delft, supported by Gordon and Betty Moore Foundation.

at the appropriate tilt to operate under two-beam condition. The 0th and 1st order diffracted beams (with their intensities dependent on the efficiency of the grating [2]) would be reflected by the mirror and re-imaged onto the grating. Passing through the grating again, on the way up, would increase the intensity of the 1st order diffracted beam [2]. In this scheme, we would be relying on the intensity of the diffracted beam as proxy for phase accumulation. We justify this choice in the Discussion section.

To measure the beam intensities, we propose two alternative detection schemes: (1) a copper plate in the form of an annulus, or (2) an annular multi-channel plate (MCP). In both cases, the primary beam would pass through the aperture undetected. In the first approach, only the beam current of the diffracted beam is measured (bucket detector) while in the second approach, an image of the diffraction spot would form onto a scintillator.

Two separate intensity measurements are necessary in order to compare diffracted beam intensities after one and two passes since measuring the beam current or imaging the diffracted beam after the first pass would prevent subsequent measurements following reflection. Therefore, a mechanism for selectively including *M*=1 intensity measurement without altering any other aspect of the experimental setup is necessary. Next, a detector placed above the phase grating and below the SEM objective lens could then measure the intensity of the 1st-order diffracted beam in the far-field after the second pass (*M*=2).

To experimentally demonstrate the damage-reduction aspect of multipass microscopy, we propose a separate experiment. In this experiment, we would expose a thin layer of electron-sensitive resist spun atop an electron-transparent film e.g. SiN in a 2-pass experiment. Next, under similar conditions, but with the mirror turned off, another resist sample would be exposed to the exact same electron dose. An area in the shape of a disk would be exposed in either case. After developing the two samples, we would measure the line edge roughness of the exposed features by either atomic force microscopy or TEM. Since shot noise in electron beam lithography is known to exacerbate line-edge roughness in the exposed features [3], a reduction in line-edge roughness in the sample exposed with the mirror turned on (*M*=2) could point towards higher SNR (i.e. lower damage) of multipass microscopy.

Discussion

An electron plane wave $\psi_i(x,y) = \exp(\mathrm{ikz})$ transmitting through a sinusoidal phase grating described by the transmission function $t(x,y) = \exp\left(im\sin\left(2\pi x/p\right)/2\right)$ would produce a function $\psi_t(x,y) = \exp\left(im\sin\left(2\pi x/p\right)/2\right)$ on the other side of the grating ($z = 0$). m and p are the phase contrast and the pitch of the grating, respectively. After the re-imaged wave $\psi_t(x,y)$ transmits through the grating for the second time, the wave $\psi_{tt}(x,y) = \exp\left(im\sin\left(2\pi x/p\right)\right)$ is formed (see Fig. 1a). The accumulated phase shift after two passes is twice that of a single pass. By calculating the square of the Fourier transforms of the waves $\psi_t(x,y)$ and $\psi_{tt}(x,y)$, their far-field intensities could be compared. It can be shown that $\left|\Psi_{tt_1}\right|^2 = 4\left|\Psi_{t_1}\right|^2$, where Ψ_{tt_1} and Ψ_{t_1} denote the 1st diffraction order of the beam that transmitted through the sample twice and one time, respectively. In other words, by passing the beam through the sample twice and accumulating twice the phase shift, the diffraction intensity quadruples.

Preliminary work

As proof of principle, we obtained simultaneous images of the top and bottom surfaces of a sample in an SEM using a tetrode electron mirror as shown in Fig. 1b-d. The top-surface image is produced as a focused beam is scanned over the top surface of a TEM copper grid with micrometer-sized features comprised of tin nanoparticles and carbon strands. Due to the nature of the sample, at certain pixels, the electrons transmit through the sample-plane undisturbed and downward towards the mirror. They are then reflected by the mirror and re-imaged onto the bottom side of the sample, producing secondary electrons which lead to formation of a scanned image.

The fact that the direct and reflected images shown in Fig. 1b,c do not fully overlap points towards electron optics misalignment, possible sources for which include stage tilt and misalignments in the lens assembly. By adding a tilt stage and by tightening the margins on machining tolerances of the tetrode mirror apertures, we hope to achieve adequate optical alignment necessary for a multipass experiment.

References

[1] T. Juffmann, *et al.*, Scientific Reports, pp. 1–7 (2017)

[2] Y. Yang, et al., Physical Review A **98**, pp. 1–8 (2018)

[3] P. Kruit *et al.*, J. Vac. Sci. Technol. B **22**, 2948 (2004)

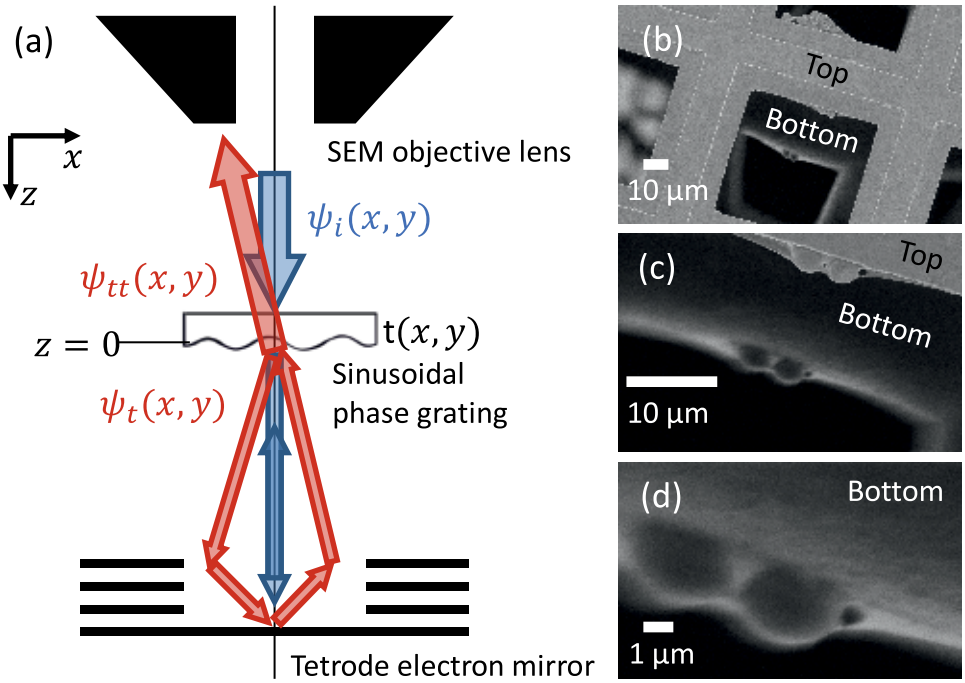

Figure 1. (a) Schematic of the proposed 2-pass electron microscopy inside a conventional SEM. Blue beam represents the primary (zeroth-order) beam. Red beam represents the first-order diffracted beam. Due to the added phase after the second pass through the sinusoidal phase grating, the intensity of the diffracted beam increases. (b),(c) Simultaneous images of top (direct) and bottom (reflected) surfaces of a sample in an SEM using a tetrode mirror. (d) Reflected image of two tin particles wrapped in carbon strands.

Implementing Conditional Re-illumination for Low-Damage Electron Microscopy

A. Agarwal[1], J. Simonaitis[1], N. Abedzadeh[1], V. Goyal[2] and K. K. Berggren[1]

[1]Massachusetts Institute of Technology, Cambridge, USA
[2] Boston University, Boston, USA
E-mail: akshayag@mit.edu

Introduction

Adaptive imaging techniques have been increasingly used in transmission and scanning electron microscopy, particularly in applications where low electron dose is necessary [1-3]. Recently, we introduced an adaptive imaging scheme that conditionally re-illuminates sample pixels based on the electron counts already collected at the electron imaging detectors [4]. Combined with interaction-free imaging [5], this scheme could potentially reduce the required imaging dose by an order of magnitude. However, our analysis was limited to opaque-and-transparent samples, and did not account for semi-transparency of the sample. In this work, we will develop the formalism for applying conditional re-illumination to semi-transparent samples. We will also discuss progress in experimental implementation of conditional re-illumination in an SEM.

Methods

We can treat the transparency $\alpha \in [0,1]$ of a sample as a continuous random variable. We used the counts at the imaging detectors to form an estimate of α, and analyzed the performance of the estimator by looking at its mean squared error (MSE). For unbiased estimators, the inverse of the classical Fisher Information (FI) forms a lower bound for this MSE (Cramér-Rao (CR) bound). We compared the performance of IFM and STEM by calculating the MSE for different estimators of α, and comparing it to the CR bound.

A major requirement in implementing conditional re-illumination is the ability to count detected electrons. We outcoupled the signal from the Everhart-Thornley (ET) secondary electron detector of a Zeiss LEO SEM, using a 50 Ω impedance line onto a 2 GHz oscilloscope, and recorded the signal pulses. To obtain these pulses, the electron beam was held stationary and the ET signal recorded. Then, we created a histogram of the pulse heights, from which we hope to determine the signal level corresponding to single secondary electrons. Similar techniques have been previously used to count secondary electrons in SEM [6] and scattered electrons in STEM [7-9].

Results

We found that the FI per incident electron on the sample was identical for STEM and IFM, shown by the solid blue curve in figure 1(a), (STEM imaging) and figure 1(b) (IFM imaging). Figure 1(a) shows the MSE of two STEM estimators for α: $\widehat{\alpha_1}$ and $\widehat{\alpha_2}$, calculated using Monte-

Carlo simulations. These estimators use the counts from the STEM imaging detectors (dark- and bright- field) in different ways - $\widehat{\alpha_1}$ (purple dashed curve) averages over these counts to estimate α, while $\widehat{\alpha_2}$ (orange dashed-dotted curve) uses the ratio between the counts at the bright-field detector and the total counts at both detectors. Compared to $\widehat{\alpha_1}$, $\widehat{\alpha_2}$ has a lower MSE, and it meets the CR bound (solid blue curve). Figure 1(b) shows the MSE for two IFM estimators for α: $\widehat{\alpha_3}$ and $\widehat{\alpha_4}$. $\widehat{\alpha_3}$ (purple dashed curve) averages over the counts at different IFM imaging detectors to estimate α, while $\widehat{\alpha_4}$ (orange dashed-dotted curve) uses the square of the difference between the counts. Again, $\widehat{\alpha_4}$ is a better estimator for α and is close to the CR bound.

Figure 2(a) shows the histogram of secondary electron pulse heights from the ET detector of a Zeiss LEO SEM. Since we held the beam stationary over a hole in the sample, the detector should nominally have no signal. The signal recorded on the detector can have two sources - detector amplifier noise, and secondaries generated by the beam striking the walls of the microscope chamber. The histogram shows two peaks – a narrow peak at 0.4 V, which is also present when the gun is turned off, indicating that it is due to amplifier noise. A second, broad peak is present around 1.5 V. This peak is also present when the beam is held stationary over a thin carbon membrane, indicating that it arises due to secondaries. Such peaks have been previously attributed to the signal from single secondary electrons [5]. We are currently working on verifying the origin of this peak, and trying to obtain two- and three- electron peaks.

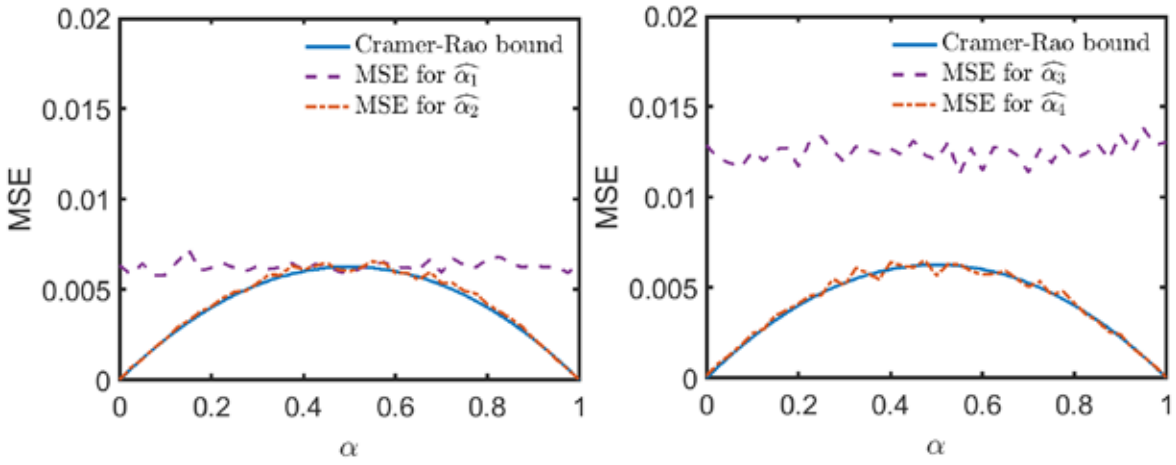

(a) (b)

Figure 1: Mean square error (MSE) vs transparency α, for (a) conventional STEM imaging, and (b) IFM imaging. MSE depends on how the estimators use the counts at various imaging detectors. This analysis is important for establishing the best estimator for the pixel transparency.

Conclusions

We are developing theoretical tools to analyze the information and error probability in semi-transparency measurements using STEM and IFM. We have also outcoupled the secondary electron signal from the ET detector on an SEM. If the histogram peak we have observed can be attributed to single secondaries, we can use its voltage level to count the number of secondaries produced on every sample pixel as the beam scans over it. This count would then

be used to infer the pixel's brightness (or transparency) using the estimators developed here, and a decision on re-illumination made using the expected MSE for the estimators developed in this work. Future work towards the implementation of conditional re-illumination for semi-transparent samples will entail refining these tools to account for loss of signal due to imperfect detection, and implementing customized scanning protocols to control the position of the beam (similar to vector scanning in electron beam lithography) and the pixel dwell time.

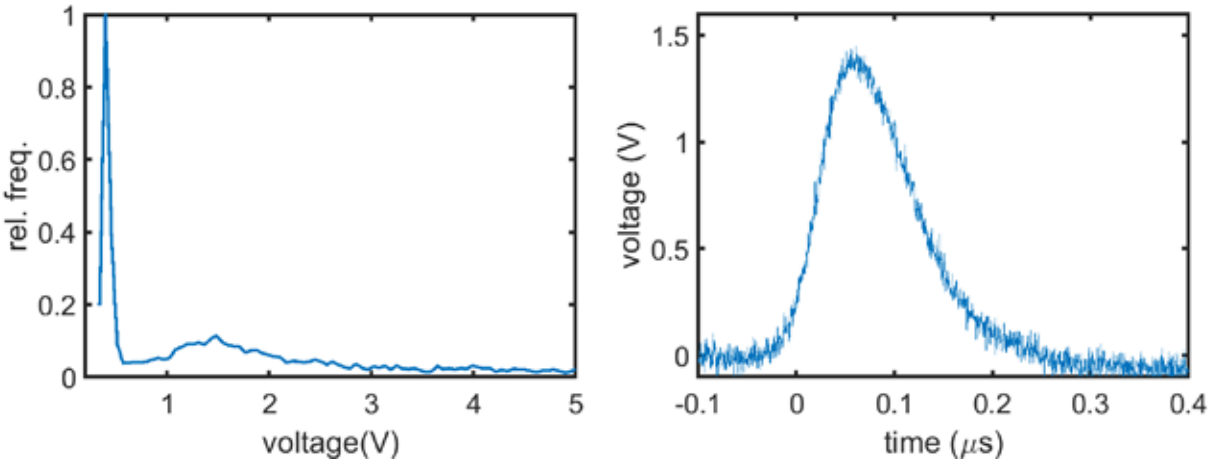

(a) (b)

Figure 2: Outcoupling signal from ET detector on SEM. (a) Histogram of secondary electron pulse heights, showing a sharp peak near 0.4V due to amplifier noise, and a broad peak at 1.5V, possibly due to single electron pulses. (b) Example of a signal pulse that contributes to the broad peak.

References

[1] Stevens et al. (2018), Applied Physics Letters, **112**, 043104

[2] Trampert et al. (2018), Ultramicroscopy, **191**, 11–17

[3] Dahmen et al. (2016), Scientific Reports, **6**, 25350

[4] Agarwal et al. (2019), arXiv:1901.09702 [physics.ins-det]

[5] Elitzur and Vaidman (1993), Foundations of Physics, **23**(7), 987–997

[6] Uchikawa et al. (1992), Journal of Electron Microscopy, **41**(4), 253–260

[7] Ishikawa et al. (2014), Microscopy and Microanalysis, **20**, 99–110

[8] Mittelberger et al. (2018), Ultramicroscopy, **188**, 1–7

[9] Sang at al. (2016), Ultramicroscopy, **161**, 3–9

Progress on the realization of a pixelated programmable phase plate for electrons

A. Béché[1], G. Guzzinati[1], D. Jannis[1] and Jo Verbeeck[1]

[1]EMAT, University of Antwerp, Groenenborgerlaan 171, 2020 Antwerp, Belgium
E-mail: armand.beche@uantwerpen.be

Introduction

Light optics highly profited from the appearance and development of programmable phase plates over the last decades. Such device freely modulates the phase of an optical wave in a computer controlled manner, which gave rise to the realisation of exotic beams such as non-diffracting beams, vortex beams and so on, with applications spanning from astrophysics to advanced light microscopy and particle manipulation in optical tweezer setups.
By the wave optics analogy, electron waves could potentially be manipulated in a similar way. Many devices already exist to manipulate the phase of electron beams, such as static phase plates, with applications ranging from contrast enhancement (Zernike, Hilbert or Volta phase plates) to the creation of vortex, Airy or Bessel beams. These static phase plates are using microscopic electrostatic fields, produced by transmission through thin objects, local charging, or magnetic fields. In spherical aberration correctors, the control of the electron wave is more versatile, thanks to the presence a large number of electromagnetic and electrostatic multipoles. However, the design of such correctors, with active elements placed outside the area containing the beam, only allows control of the phase of the electron in a continuous way, due to constraints stemming from the Laplace equation.
In order to gain more control over the phase of the electron wave, we are developing a pixelated programmable phase plate for electron beams based on an array of independent einzel lenses. We show here the latest update on this development.

Description

Einzel lenses are composed of a cylindrical electrode located between two ground planes. By applying a voltage on the electrode, the electron experiences a temporary change in velocity during its flight through the cylinder, which results in a phase shift. The two ground planes shield the electrostatic field created by the electrode, allowing to place the einzel lenses on an array with limited interactions between each other. Each einzel lens is then connected to an external power supply for control. With this design, each einzel lens acts as an independent pixel with a phase that can be freely manipulated within the full [0, 2π] range. A schematic of the design is displayed in Fig. 1a.

As a proof of principle, we first focused on the realization of a version limited to a 2x2 pixels square array [1]. Starting from a 200 nm thick SiN grid, a 1 μm gold layer was deposited on the back side and a 200 nm gold layer on the top side. The bottom layer provides one ground electrode and the top layer will act as contact for the core of the einzel lens. Pt pillars (1.5 μm thick, 1 μm high which center separated by 2 μm) were then grown on the gold top surface by

Focus Ion Beam Induced Deposition (FIBID). The pillars were then FIB drilled from the top to create a path for the electron beam. As the realization of the top ground electrode proved to be too unreliable by FIB technique, it was not used in this simplified version. The final design of the phase plate is displayed in Fig. 1b. The phase plate was finally mounted on a 4 contacts Dens Solutions chip heating holder and introduced in the sample plane of an FEI Titan³ transmission electron microscope operating at 300 kV in Lorentz mode. Switching off the objective lens allowed to reach an extended camera length while keeping good beam coherence over the size of the device.

Results

In the far field plane of the phase plate, the electron waves passing through the four einzel lenses interact, forming a 4 slits experiment (see Fig. 1c). By modifying the different potentials, one can change the symmetry of the pattern. Defocusing the far field image gives rise to a slightly more complex pattern, but allows visualizing better the interactions between the different pixels. In Fig. 1c, different symmetries were tested, such as the left/right and up/down Hilbert phase plate, diagonal symmetry, and a crude representation of an electron vortex beam. In the defocused images, the region of destructive interference, when the phase is jumping abruptly from 0 to π are clearly visible with a dark contrast appearing whereas a bright contrast is present in the case that no phase difference is applied between the neighboring pixels.

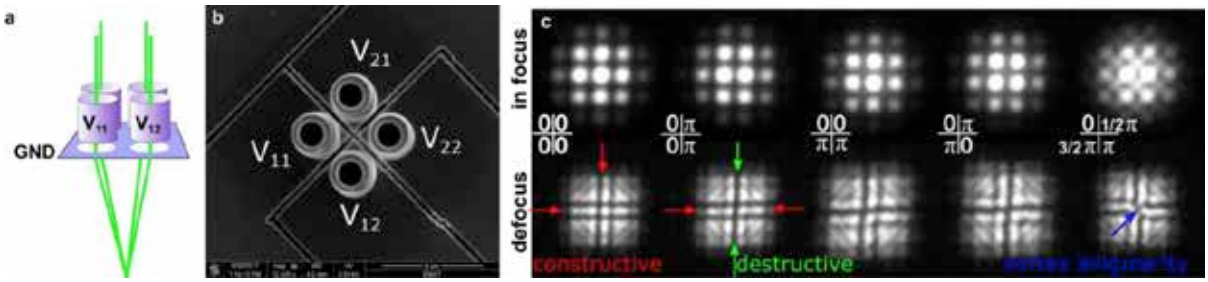

Fig. 1 a) Schematic set up of the 2x2 phase programmable array. b) SEM image of the device showing 4 cylindrical electrodes that can be put on separate electrostatic potentials Vij. c) Resulting interference pattern when mounted in the TEM showing the complete control of the phase of the 4 interfering beams resulting in different interference patterns.

Discussion

The successful realization of a 2x2 phase plate is driving us towards the realization of a more complex design, which will allow more complex electron waves to be obtained. Simulations predict that the use of 30 to 60 pixels could already provide sufficient flexibility to create interesting beams (Fig. 2) and could even provide a crude Cs corrector.

Thanks to a recently granted started ERC proof of concept grant (ADAPTEM) [2], we are developing a lithographic process to create such phase plate (Fig. 3). First results from these efforts will be provided .

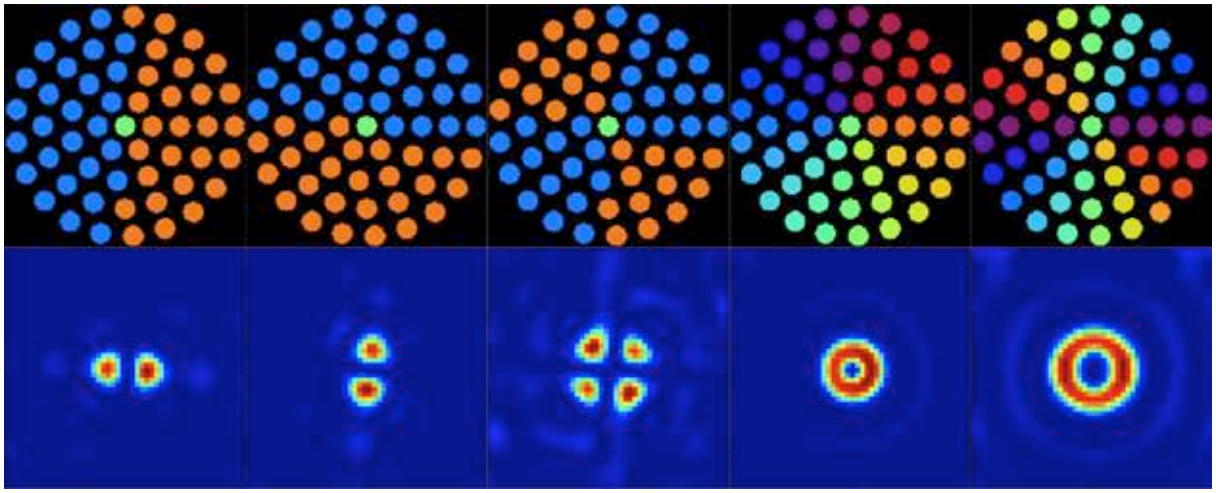

Fig. 2 A simulated upscaled version of an electron phase plate could serve as an attractive tool to study exotic electron beams. From left to right HG10, HG01, HG11LG01, LG02 beams.

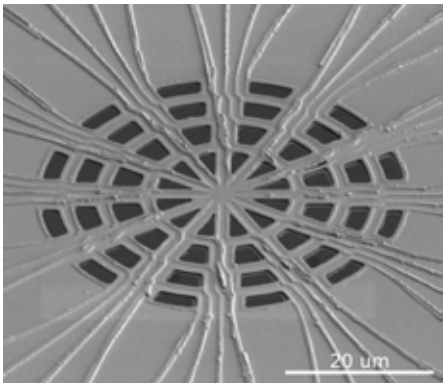

Fig. 3 Lithographically processed phase plate composed of 48 pixels designed in a segmented fashion. This is one of the multiple designs we are currently testing.

References

[1] J. Verbeeck, A. Béché, K. Müller-Caspary, G. Guzzinati, M. Anh Luong, M. Den Hertog, Ultramicroscopy **190**, 58 -65 (2018) and https://arxiv.org/abs/1711.11373F.

[2] J.V. and A.B. acknowledge funding from the Fund for Scientific Research Flanders FWO project G093417N and the European Research Council, ERC Starting Grant 278510 VORTEX and ERC proof of concept project DLV-789598 ADAPTEM. The Qu-Ant-EM microscope was partly funded by the Hercules fund from the Flemish Government.

FEL: Quantum Effects in Phase Space

C. Moritz Carmesin[1,2], Peter Kling[1,2], Enno Giese[1], Roland Sauerbrey[2], Wolfgang P. Schleich[1,3]

[1] Institut für Quantenphysik and Center for Integrated Quantum Science and Technology (IQST), Universität Ulm, 89081 Ulm, Germany

[2] Helmholtz Zentrum Dresden Rossendorf, 01328 Dresden, Germany

[3] Hagler Institute for Advanced Study, Institute for Quantum Science and Engineering (IQSE), and Texas A&M AgriLife Research, Texas A&M University, College Station, TX 77843-4242, USA

e-mail: moritz.carmesin@uni-ulm.de

Introduction

A free-electron laser (FEL) is usually considered a classical device since its dynamics can be fully described within classical physics. The reason for this fact is the parameter regime wherein the state-of-the-art devices operate. However, there exists a quantum regime [1, 2], where a quantum mechanical model of the process is mandatory for an accurate description.

Starting from the quantum mechanical description of the FEL in Wigner phase space, we study the emergence of quantum effects depending on specific parameters, in particular the strength of the fields compared to the recoil energy and the initial momentum spread.

Methods

We solve analytically the classical dynamics of a distribution function in phase space and compare it to the time evolution of the quantum mechanical Wigner function, which is obtained by a semi-analytical approach [3].

Results

The smaller the initial width of the momentum distribution and the smaller quantum parameter α, describing the ratio of the field strength and the recoil energy, the more differ the classical distribution and the Wigner function, cf. Figure 1. Moreover, after sufficient time both distributions disagree due to the nonlinear dynamics, even if the requirements of a narrow momentum distribution and a small value of α are not satisfied.

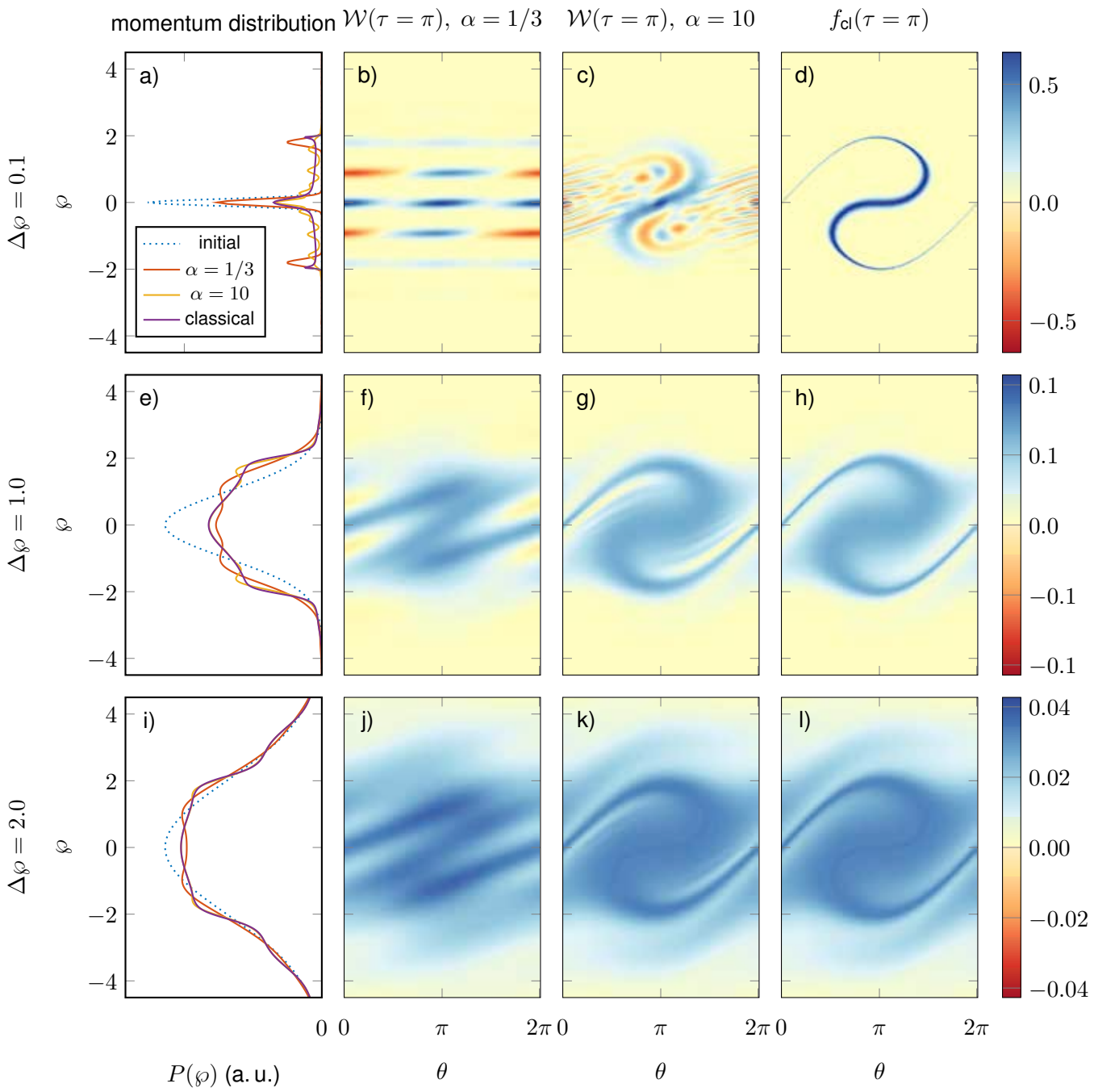

Figure 1: Comparison of momentum distributions, Wigner functions and corresponding classical phase space density for different values of the quantum parameter α and different initial momentum widths $\Delta_\wp$ with mean momentum $\bar{\wp} = 0$. Each row corresponds to a different momentum width $\Delta_\wp = 0.1$, 1.0, or 2.0. The left column shows the initial momentum distribution and the evolved ones at dimensionless time $\tau = \pi$ for the quantum parameters $\alpha = 1/3$ and 10 as well as the corresponding classical result. The second and third column show the Wigner functions $\mathcal{W}(\theta, \wp, \tau)$ at time $\tau = \pi$ for $\alpha = 1/3$ and $\alpha = 10$, respectively. The rightmost column depicts the classical distribution function $f_{\mathrm{cl}}(\theta, \wp, \tau)$ at the same time $\tau = \pi$. Only in the case of a large α and $\Delta_\wp$ classical and quantum mechanical distribution resemble each other.

References

[1] R. Bonifacio, N. Piovella, G. R. M. Robb, and A. Schiavi. 2006. *Phys. Rev. STAB* **9** 090701

[2] P. Kling, E. Giese, R Endrich, P. Preiss, R. Sauerbrey and W. P. Schleich. 2015. *New J. Phys.* **17** 123019

[3] C. M. Carmesin, P. Kling, E. Giese, R. Sauerbrey and W. P. Schleich. *in preparation*

Atomic Resolution Dynamics for Soft-Materials: from Low Dose to Interaction-Free "Electron Microscopy?

Fu-Rong Chen[1], Stig Helveg[2], Hector Calderon[3], Christian Kisielowski[4] and Dirk Van Dyck[5]

1. Department of Materials Science and Engineering, City University of Hong Kong, Kowloon, Hong Kong.
2. Haldor Topsoe A/S, Haldor Topsøes Allé 1, DK-2800 Kgs. Lyngby, Denmark.
3. Instituto Politécnico Nacional, Mexico
4. Lawrene Berkeley National Laboratory, The Molecular Foundry and Joint center for Artifical Photosynthesis, One cyclotron Road, Berkeley California 94720 USA
5. EMAT, Department of Physcis, University of Antwerp, Belgium

* Corresponding author: frchen@cityU.edu.hk

Introduction

Over the past decade, electron microscopy has become indispensable for studying nano-materials at the atomic-scale. The ability to acquire atomic-resolution images with single-atom sensitivity has opened up for unprecedented insight into materials science. However, It still has several bottlenecks, one of the most important one is radiation damage. Observations at the atomic-level require an intense electron illumination that generally alters the nano-structure during observation. The electron-induced alterations are particular pronounced at the nano-materials surface as they expose a variety of sites of reduced atomic coordination. In the quest to suppress electron-induced alterations and to enable chemical meaningful observations, it therefore becomes mandatory to exercise control over the electron dose, dose-rate and energy.

Here, we demonstrate low dose-rate in-line electron holography as a viable concept for dynamics observations of soft materials at atomic resolution in the genuine state. The imaging scheme employs bright field transmission electron microscopy (TEM) as the most efficient way to detect single atoms using the fewest elastically scattered electrons. The image acquisition is done with low electron dose-rates of down to 1-100 $e^{-}Å^{-2}s^{-1}$ to inflict the weakest object excitation and to offer time for reversible object restoration between successively delivered electrons. As a result, the individual atomic- resolution images are dominated by noise, and recovery of image signal can be accomplished by averaging over a series of consecutively acquired images of the object. For this purpose, in-line holography based on focal image series is particular attractive as residual aberrations are corrected and the exit wave (EW) function recovered with enhanced signal that is quantitatively interpretable. The dose rate can be precisely controlled via a gun monochromator and the pulse electron source TRACE (time-resolved aberration corrected environmental) TEM to be setup in city university via which we are able to record dynamics of soft materials with high space time resolution with preserving the sample in its pristine state. However, for the single molecule case, we may need to take one step further to even avoid the electron-sample interaction. I will discuss our implementation of interaction-free measurement in light optics to electron optics toward achieving the concept of "Quantum Seeing in the Dark" in "quantum electron microscope.

Methods

The dose rate can be precisely controlled via a gun monochromator [1] and the pulse electron source TRACE (time-resolved aberration corrected environmental) TEM to be setup
in city university of Hong Kong via which we are able to record dynamics of soft materials with high space time resolution with preserving the sample in its pristine state. It is reported that It takes about 500 e/A^2 to visualize a single Au atom and It takes about 10000 e/A^2 to visualize a single C atom. However, for a biological sample, the maximum sustainable dose is only 25 e/A^2. In our method, electron hologram the exit wave function is reconstructed from focal series images. The required total dose can be spread into many focal series images so that each snapshot can be received low level of electron dose to minimize the radiation damage. There are two advantages of our approach. First, good signal to noise can be recovered from focal series images acquired at low dose mode. Second, exit wave function offers 3D atomic structure [2,3].

I will demonstrate the analysis of 3D oleic acid molecules. It shows that even at 50keV and 5 e/A^2., we can only see the fragment of the oleic molecule which implicitly implies that an even strict dose condition is required for the single molecule. For the interaction free measurement, a beam splitter and electron resonator are required. In my talk I will show our preliminary thought to development quantum electron microscope based on a low kV TEM.

Results

In the present work, through focal series images of a nanoparticle made of NiO and Pt are recorded with TEAM05 at low dose mode. The dose rate was controlled by a monochromator in the downstream of electron gun. Fig. 1 show the phase images of three reconstructed exit wave functions. Each of them is reconstructed from 20 through focal series images. The dose rates associated with each reconstructed exit wave function are 56, 92, and 185e/Å^2.sec, respectively. The total times of particle under exposure of electron beam are 1, 6 and 9 minuets, respectively. As we can see that the particle not only changes the shape but also rotates as a function of time due to the electron beam interaction. The 3D shape of the particle at atomic resolution are reconstructed using the method given in one of our previous publication [3, 4].

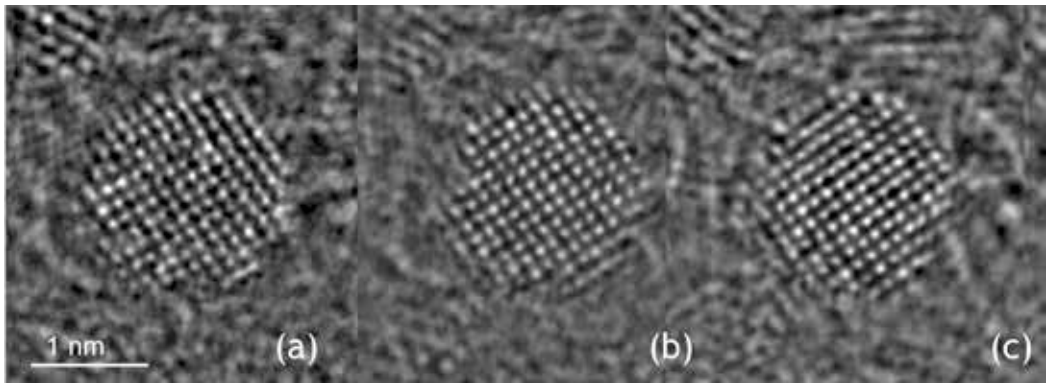

Figure 1. Phase images of three reconstructed exit wave functions. Each of them is reconstructed from 20 through focal series images. The dose rates for (a), (b) and (c) are 56, 92, and 185e/Å.sec, respectively. The total times of particle under exposure

of electron beam are 1, 6 and 9 minuets, respectively. The space/ time resolution is $\Delta x \Delta t \sim 10^{-10}$ m.sec in this case.

Discussion

In my talk I will show atomic resolution dynamics of graphene in 3D can be improved from $\Delta x \Delta t \sim 10^{-10}$ m.sec to 10^{-16} m.sec using a fast camera. And I will discuss a new setup of TEM with pulse electron source with a beam chopper and a tile camera in cityU of Hong Kong which is expected to improve to space/ time resolution even better that the graphene case. In regular a Mach-Zehnder interferometer for interaction free measurement, beam splitters and an electron beam resonator [4] are two critical components. As shown in the figure 2, a preliminary design of electron beam splitter is composed of a quadrupole and hybrid dipole/ hexapole for electron beam splitter is proposed for a 15keV low voltage electron microscope. To facilitate the concept of interaction-free measurement into an "imaging" instrument, we need focus device in the path of the Zeno quantum resonator. This will be discussed in my talk.

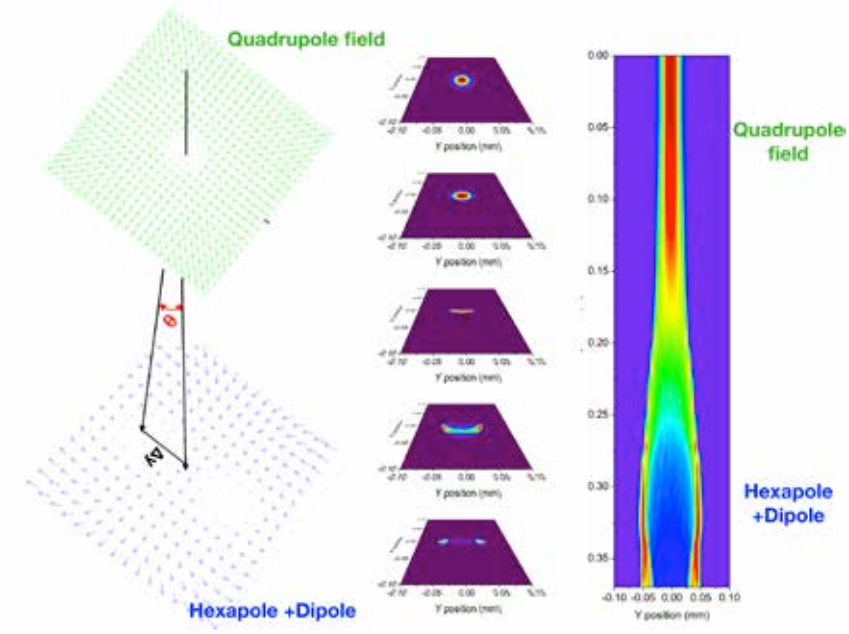

Fig. 2. A preliminary design of beam splitter that is composed of a quadrupole and a hybrid hexapole and dipole fields.

References

1. C. Christian et al., Micron 68, 186-193 (2015)
2. Dirk Van Dyck, Joerg R. Jinschek & Fu-Rong Chen, NATURE, 486, 243 (2012)
3. F.-R. Chen, D. Van Dyck & C. Kisielowski, NATURE COMMUNICATIONS | 7:10603 | DOI: 10.1038/ncomms10603
4. Vittorio Giovannetti, Seth Lloyd, Lorenzo Maccone, SCIENCE 1330-1336, 306 (2004)

Sub-cycle electron pulse shaping with terahertz control fields

Dominik Ehberger[1,2] and Peter Baum[1,2,3]

[1]*Ludwig-Maximilians-Universität München, Am Coulombwall 1, 85748 Garching, Germany.*

[2]*Max-Planck-Institute of Quantum Optics, 85748 Garching, Germany*

[3]*Fachbereich Physik, Universität Konstanz, Universitätsstr. 10, 78467 Konstanz, Germany.*

e-mail: dominik.ehberger@physik.uni-muenchen.de

The experimental techniques of ultrafast electron diffraction and microscopy (UED/UEM) rely on short electron pulses to resolve structural and electronic dynamics on their fundamental length and time scales. Dispersion of sub-relativistic electron pulses in vacuum as well as space-charge effects, however, limit the duration of uncompressed electron pulses to well above hundred femtoseconds. Therefore, the ability to shape electron pulses in time is indispensable when it comes to the investigation of the fastest atomic and electronic motion on the few-femtosecond level and below. The emerging capabilities to control electron pulses by all-optical means bear the potential to revolutionize time-resolved imaging techniques with electrons.

Here, we report an electron pulse compression and characterization concept that is based on the interaction with a terahertz electromagnetic wave on sub-cycle time scales [1]. Key to this level of control are suitable modulation elements to transfer momentum from the optical wave to the charged particles in the pulse. An element as simple as a plain electron-transmissive and optically reflecting planar membrane enables a broad range of electron pulse manipulation capabilities by harnessing the complex interplay of transverse and longitudinal forces acting on an electron crossing the mirror [2].

By virtue of the unique combination of this element with a terahertz single-cycle pulse, we demonstrate the compression of an electron pulse by a factor of > 17 down to a duration of 28 fs (FWHM), which is among the shortest reported to date [3]. The all-optical implementation features inherent, passive temporal stability on a few-fs level. In particular, the concept is largely independent of the electron beam size and therefore also suited for electron beams of limited transverse emittance.

Furthermore, this control scheme features the possibility to generate compressed electron pulses with a defined tilt angle [2]. This additional degree of freedom promises to facilitate future UED and UEM experiments in constrained geometries. Our experiments reveal that the tilt angle of an electron pulses is related to angular dispersion, which before was only known for optical pulses.

Simulations show a route towards the generation of isolated sub-femtosecond electron pulses via terahertz compression at a planar metal membrane [3]. Electron pulses of such short duration will allow the investigation of sample dynamics induced by the cycles of light rather than its intensity envelope. First diffraction and microscopy studies with attosecond electron pulse trains demonstrate the feasibility of this approach [4]. Isolated attosecond electron pulses will furthermore allow novel electron microscopy concepts to resolve electromagnetic fields in complex optical materials at frequencies of visible light [5].

Lastly, we show that our all-optical electron pulse compression and streaking scheme cannot only be used to compress electron pulses, but also to measure electron spectra in a time-of-flight fashion [6]. This approach features few-eV and potentially meV energy resolution, which we demonstrate in a proof-of-principle experiment on Plasmon loss from an aluminum sample.

References

[1] C. Kealhofer, W. Schneider, D. Ehberger, A. Ryabov, F. Krausz, and P. Baum, Science **352**, 429 (2016)

[2] D. Ehberger, A. Ryabov, and P. Baum, Phys. Rev. Lett. **121**, 094801 (2018)

[3] D. Ehberger, K. J. Mohler, T. Vasileiadis, R. Ernstorfer, L.Waldecker, and P. Baum, Phys. Rev. Applied **11**, 024034 (2019)

[4] Y. Morimoto and P. Baum, Nat. Phys. **14**, 252 (2018)

[5] A. Ryabov and P. Baum, Science **353**, 374 (2016)

[6] D. Ehberger, C. Kealhofer, and P. Baum, Struct. Dyn. **5**, 044303 (2018)

Nanofabrication of Spiral Phase Plate for electron microscopy

P. Rosi[1], S. Frabboni[1], Peng-Han Lu[3], E. Rotunno[1], G.C. Gazzadi[1], A. Tavabi[3], Robert Nijland[4], Peter Tiemeijer[4] ,Rafal Dunin Borkowski[3], V.Grillo[1]

[1] Dipartimento FIM Universitá di Modena e Reggio Emilia, Via G Campi 213/a, I-41125 Modena, Italy.
[2] CNR-Istituto Nanoscienze, Centro S3, Via G Campi 213/a, I-41125 Modena, Italy
[3]Ernst Ruska-Centre for Microscopy and Spectroscopy with Electrons Forschungszentrum Jülich GmbH, De52425 Jülich, Germany
[4]Thermo Fisher Scientific, Achtseweg Noord 5, 5651 GG Eindhoven, Netherland
E-mail: stefano.frabboni@unimore.it

Introduction

In cryo- and high resolution electron microscopy imaging methods of weak phase specimens, there is a need to increase the image contrast, minimizing the electron dose for given beam current. It is known that this can be achieved by use of phase plates [1], designed to change the difference between the phases accumulated by scattered and direct electron waves in their transit from the specimen to the detector. Here we present the advances in the nanofabrication of a Spiral Phase Plate (SPP) spatial Fourier filter which adds an angularly dependent phase shift to the wave function in the objective focal plane of the form $e^{il\varphi}$ [2]. Assuming unit amplitude incident plane wave, this transmittance is obtained by a spiral staircase thickness profile imparted to a transparent silicon nitride membrane by Focused Ion Beam (FIB) milling. An additional top-hat amplitude filter, to control the transmitted intensity present close to the zero spatial frequency, is added to the SPP in order to obtain annular dark field (ADF) images of the weak phase specimen.

Methods

The image of phase-object, when a phase plate is inserted in the back focal plane of the objective lens, is given by the square modulus of the convolution between the object wave function and the inverse Fourier transform of the phase plate transmittance.

It has been already demonstrated [2] that the SPP spatial Fourier filter acts selectively on electrons scattered into the directions corresponding to the phase gradients (or amplitude and phase gradients in more complicate cases) of the transmitted electron wave function adding a π phase shift across any diameter of the phase plate. It works as a two dimensional radially symmetric Hilbert phase plate [1], thus expected to symmetrically enhance the edges of the image [2,3]. A critical step in the realization of the SPP is the control of the unscattered

part of the transmitted wave that should be focused in the region of the zero spatial frequency at the center of the SPP, a point which contains the major amount of the intensity and where the phase of the SPP transmittance is undefined.
Here we propose to control the transmittance of this portion of the filter with an “electron absorber” formed by a Au island deposited at the center of the SPP in order to obtain high contrast ADF images.
The SPP have been fabricated by Focused Ion Beam milling of a Si_3N_4 membrane using a Ga+ ion beam at an energy of 30keV. Before patterning the Si_3N_4 membrane has been covered with approximately 150nm of Au, the milling process can then be carried on in 2 step: the first one involved the removal of the Au from a circular region with diameter equal to 20um and pre-thinning on the 200nm to about 110nm with an ion current equal to 0.8 - 1 nA; the second step involved reproducing the spiral pattern on the membrane and this has been done using an approximately 24pA ion current. The Au island in the center has been obtained during the first step, where we also selected an inner diameter of approx 150nm making the “removal plus pre-thinning” region effectively a ring shaped one. The radius of the SPP, considering an objective focal length of the order of 1mm, corresponds to a spatial frequency of approximately $4nm^{-1}$.

Results.

In Fig.1 are reported two SPP’s for BF imaging (a) and ADF imaging (b). The small dark dot, barely visible at the center of the SPP in (b), enlarged in the inset in upper right corner, is the the Au island approximately 100nm in diameter. The inset in the upper left corner shows the Fraunhofer diffraction pattern of this SPP.

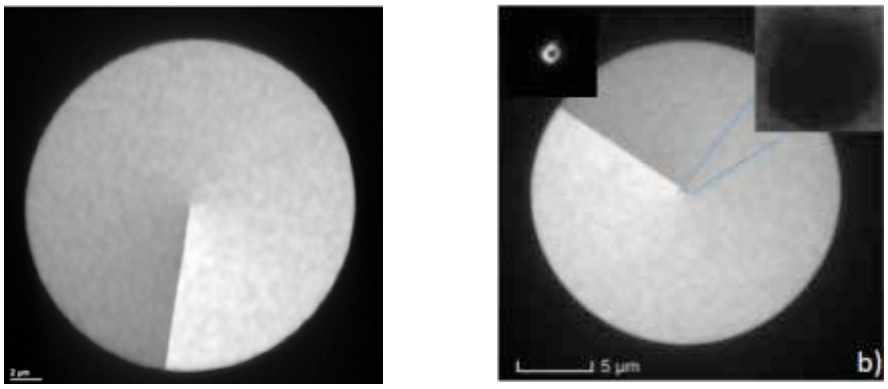

Fig. 1 a) SPP for BF imaging, and b) SPP for ADF imaging. The Au dot, approximately 100nm in diameter is visible in the inset. The Fraunhofer diffraction pattern is also shown in the upper left corner of the figure.

Discussion

Images of proteins with SPP in BF and ADF modes have been simulated by the STEM-cell software [4] in order to evaluate the image contrast of in-focus images. In BF mode a constant phase shift, given by the thickness of the unpatterned membrane in the central pixel of the SPP, has been assumed. Images in ADF mode have been simulated by setting zero amplitude over an area at the center of the SPP.

In Fig 2 are reported the simulated protein images obtained with a SPP for ADF, a) to e), with increasing radius of the cut in the low spatial frequencies. In Fig 2f) is shown a BF image. These simulations show that the ADF images have a decreasing amount of low frequency details as the inner radius increases and the expected isotropic edge enhanced contrast. The BF image in f), obtained with a central area of the SPP acting as a transmissive phase shifter shows a relief-like shadow profile. This, as suggested by Barnet [5] in optics, can be ascribed to the presence of a preferred orientation in the SPP defined by the radial direction where the phase plate values correspond to the phase value of the central pixel.

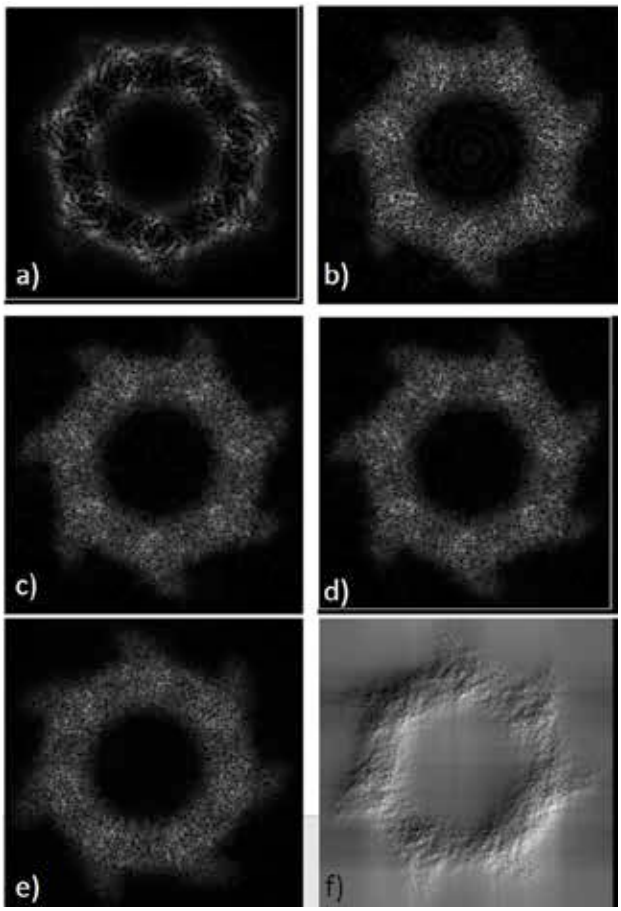

Fig.2 Simulated protein images with different SPPs. ADF, a) to e), and BF, f) images. The inner radius of the annular apertures is: 0.1532 nm^{-1} a); 0.9193 nm^{-1} b); 2.451 nm^{-1} c); 3.983 nm^{-1} d); 8.58 nm^{-1} e). In the BF image, f), the radius of the phase plate is 8.58 nm^{-1} .

References

[1] R. M. Glaeser, Review of Scientific Instruments **84**, 111101 (2013).

[2] R. Juchtmans, L. Clark, A. Lubk and Jo Verbeeck, Phys. Rev. A **94**, 023838 (2016).

[3] A.M. Blackburn, J.C. Loudon, Ultramicroscopy **136**, 127 (2014).

[4] V. Grillo et. al. Ultramicroscopy **125,** 97 (2013).

[5] S. Barnet et al. Optics Express **14**,3792 (2006).

Quantum coherent optical transverse and longitudinal shaping of free electron beams

A. Feist[1], K. E. Priebe[1], T. Rittmann[1], C. Rathje[1,2], T. Harvey[1], S. V. Yalunin[1], T. Hohage[3], S. Schaefer[1,2] and C. Ropers[1]

[1] IV. Physical Institute, University of Göttingen, Göttingen, Germany
[2] Institute of Physics, University of Oldenburg, Oldenburg, Germany
[3] Institute for Numerical and Applied Mathematics, University of Göttingen, Göttingen, Germany
E-mail: armin.feist@uni-goettingen.de

Introduction

Ultrafast transmission electron microscopy (UTEM) is a powerful tool to study the dynamics of nanoscale systems, combining the versatile imaging, diffraction and spectroscopy capabilities of state-of-the-art TEM with femtosecond temporal resolution of a laser pump/electron probe scheme [1,2]. To further extend the UTEM methodology, electron pulses with enhanced coherence properties are desirable [3], as required for the quantitative local probing of laser-excited dynamics in nanostructures. In particular, the inelastic scattering between high energy electron pulses and strong optical near fields [4] allows for a coherent manipulation of the free-electron quantum state [5].

Methods

The Göttingen UTEM instrument is based on a JEOL 2100F Schottky field emission TEM, which we modified to allow for optical sample excitation and the generation of ultrashort electron pulses (Fig. 1a) [3,5].

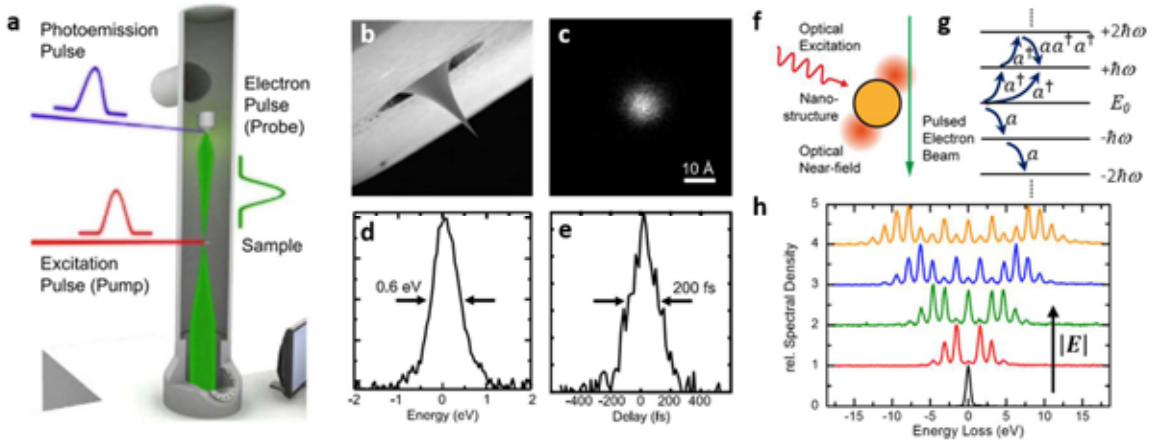

Fig. 1. a) Experimental scheme: Ultrashort coherent electron pulses, generated by nanotip photoemission (b), are accelerated and focused in the sample plane of the microscope (beam properties: c-e). f) The electron beam interacts with an intense optical near field, (h) with its kinetic energy distribution evolving into a comb of multiple spectral sidebands spaced by the photon energy. g) Energy level diagram of ladder states with spacing ħω coupled to the initial state at E_0. Multi-level Rabi oscillations are observed in the sideband occupations due to sequential multistate population transfer and interfering quantum paths (indicated by arrows). Figures adapted from Refs. [3,5].

The nanoscopic photoelectron source (Fig. 1b) employs localized single-photon photoemission from the front facet of a tip-shaped ZrO/W(100) Schottky field emitter. This source produces highly coherent ultrashort electron pulses (up to 200-keV electron kinetic energy) with a normalized emittance of a few nm·mrad. Electron focal spot sizes down to 0.8 nm, an electron pulse width of 200 fs (full-width-at-half-maximum) and a spectral bandwidth of 0.6 eV are demonstrated [3] (Fig. 1c-e).
The excellent coherence properties of the pulsed electron beam allow for investigating the optical manipulation of free-electron quantum states [5] by inelastic scattering in localized electromagnetic fields (cf. Fig. 1f) [4-9]. In this mechanism, the light field imprints a sinusoidal phase modulation onto the electron wavefunction, enabled by the broadened momentum spectrum of confined optical fields. As a consequence, the ensemble-averaged electron kinetic energy distribution evolves into a comb of spectral sidebands (cf. Fig. 1h). Furthermore, the quantum coherent nature of this interaction is evidenced by the observation of multi-level Rabi oscillations (cf. Fig. 1g) in the associated momentum state populations [5], and by coherent interactions with multiple, spatially separated light fields in a Ramsey-type geometry [10].

Results and Discussion

In one experiment, the electrons simultaneously interact with two optical near-fields of different frequencies [11] (Fig. 2a). They experience a non-sinusoidal phase modulation, giving rise to a rich variety of non-trivial free-electron momentum superposition states, e.g. depicted by highly asymmetric kinetic energy spectra (Fig. 2b). Coherent control of the free-electron wavefunction is demonstrated by tuning the amplitude and relative phase of these interactions.

In a second experiment, we employ two subsequent near-field interactions (Fig. 3a) to demonstrate the temporal structuring of free-electron beams on the attosecond timescale [5]. Dispersive propagation of the initial phase-modulated electron wave function results in an electron density modulation (Fig. 3b). After the second interaction, we record spectrograms with accurately controllable phase delay (Fig. 3c), which allows us to reconstruct the temporal shape of the electron density by employing our newly developed quantum state tomography

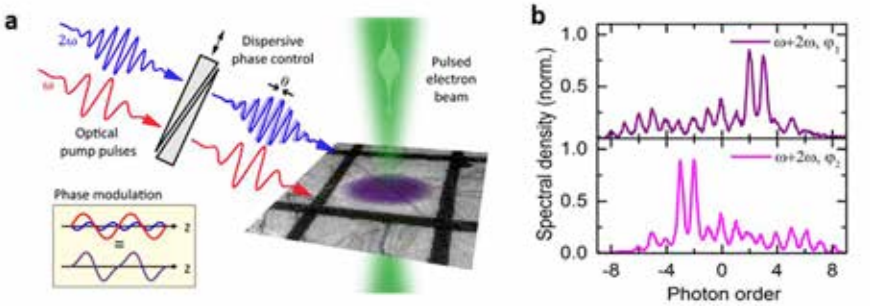

Fig. 2. a) A pulsed electron beam is overlapped with optical pump pulses at frequencies ω (λ = 800 nm) and 2ω (λ = 400 nm) on a single-crystalline graphite flake. Fused-silica wedges are used to control the relative phase between the laser pulses. For two-color laser fields, the phase modulation becomes non-sinusoidal (purple curve), b) giving rise to highly asymmetric electron energy spectra ($\varphi_1 = \pi$, $\varphi_2 = 0$). Figures adapted from Ref. [11].

technique ‘SQUIRRELS’ [11]. We experimentally demonstrate the temporal focusing of the electron pulses into a train of attosecond bursts (Fig. 3d).

In a third experiment, we will present recent data on the observation of quantized transverse momentum transfer. The high degree of coherence of the employed ultrashort electron pulses enables the full separation of individual momentum states in reciprocal space [12].

In conclusion, we demonstrate the three-dimensional optical manipulation of free-electron wavefunction by coherent interaction with intense optical near-fields. The ability to optically phase-modulate electron beams and quantitatively map electron quantum states will be a cornerstone of future free-electron quantum optics technology, e.g. enabling the programmable shaping of free-electron wave packets.

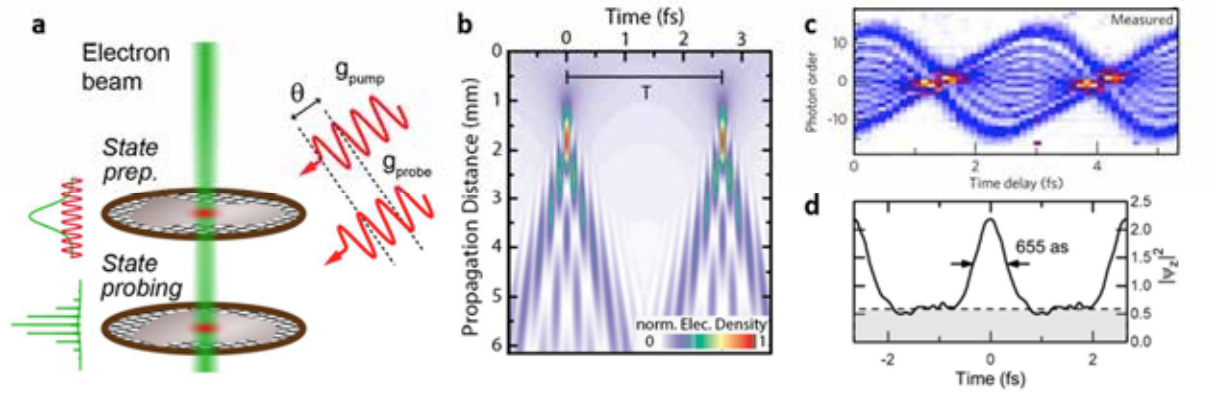

Fig. 3. a) Sketch of the experimental setup employing two graphite flakes for the preparation and characterization of attosecond electron pulse trains. b) Electron density as a function of propagation distance, revealing sub-optical cycle modulations. c) Experimental spectrogram after sequential interactions recorded over two optical cycles. d) Reconstructing its quantum state, the longitudinal free-electron wavefunction exhibits density modulations with a FWHM of 655 as. Figures adapted from Ref. [5,11].

References

[1] A. H. Zewail, Science **328**, 187 (2010).
[2] J. S. Kim *et al.*, Science **321**, 1472 (2008)
[3] A. Feist *et al.*, Ultramicroscopy **176**, 63 (2017).
[4] B. Barwick, D. J. Flannigan, and A. H. Zewail, Nature **462**, 902 (2009).
[5] A. Feist *et al.*, Nature **521**, 200 (2015).
[6] F. J. García de Abajo, A. Asenjo-Garcia, and M. Kociak, Nano Lett. **10**, 1859 (2010).
[7] S. T. Park, M. Lin, and A. H. Zewail, New J. Phys. **12**, 123028 (2010).
[8] L. Piazza *et al.*, Nat. Commun. **6**, 6407 (2015).
[9] G. M. Vanacore *et al.*, Nat. Commun. **9**, 2694 (2018).
[10] K. E. Echternkamp, A. Feist, S. Schäfer, and C. Ropers, Nat. Phys. **12**, 1000 (2016).
[11] K. E. Priebe et al., Nat. Photonics **11**, 793 (2017).
[12] A. Feist, *in preparation*

Quantum aspects of the interaction between beam electrons and optical near fields

F. Javier García de Abajo,[1,2] Valerio Di Giulio,[1] and Vahagn Mkhitaryan[1]

[1]Institut de Ciencies Fotoniques, The Barcelona Institute of Science and Technology, 08860 Castelldefels (Barcelona), Spain
[2]Institució Catalana de Recerca i Estudis Avançats, Passeig Lluís Companys, 23, 08010 Barcelona, Spain
javier.garciadeabajo@nanophotonics.es

Electron beams are ideal tools to controllably excite and probe plasmons and other nanoscale optical excitations with an unparalleled combination of space and energy resolutions. Spectroscopy performed through the analysis of electron energy loss and cathodoluminescence are widely used to obtain snapshots of these excitations. Additionally, access to the ultrafast sample dynamics is possible by recording photoelectrons excited with femtosecond light pulses, while several experiments demonstrate optical pumping followed by electron-beam probing with similar temporal resolution. In this talk, we will review recent advances in these techniques and present a unified theoretical description, along with several potential directions for improving the space-time-energy resolution and accessing quantum aspects of the samples.

As a first challenge, we will discuss fundamental limits to the coupling between electrons and optical excitations based on suitably tailored beam-electron wave functions, thus opening new directions for further increase in time resolution and the exploration of nonlinear phenomena with nanometer resolution.

Additionally, we will discuss recent theoretical results on fundamental aspects of the interaction of fast electrons with localized optical modes that are made possible by the noted advances. Using a quantum-optics description of the optical field, we predict that the resulting electron spectra strongly depend on the statistics of the sample excitations (bosonic or fermionic) and their population (Fock, coherent, or thermal), whose autocorrelation functions are directly retrieved from the ratios of electron gain intensities. We further explore feasible experimental scenarios to probe the quantum characteristics of the sampled excitations and their populations.

A proposal for a basis change paradigm to optimally look at proteins

V.Grillo[1], E. Rotunno[1], M. Zanfrognini[1], and S. Frabboni[2], P. Rosi[2], F. Troiani[1]

[1]CNR-Istituto Nanoscienze, Centro S3, Via G Campi 213/a, I-41125 Modena, Italy
[2] Dipartimento FIM Universitá di
Modena e Reggio Emilia, Via G Campi 213/a, I-41125 Modena, Italy.
E-mail: vincenzo.grillo@nano.cnr.it

Introduction

Most TEM techniques are limited to the imaging and energy spectroscopy of the electron wavefunction. Imaging in terms of quantum mechanics means to analyze in the position representation.

However, when a single sample property is sought, most of the image information is useless, a waste that cannot be afforded in dose-sensitive materials. We wonder if it is possible to extract the sought information, or maybe just recognize a specific object between a narrow list, without the need to actually image it.

We propose that a change of basis could possibly solve this problem. Here we show how an explicit change of basis can be done using 3 phase elements strongly based on the OAM sorter working principles.

We will also discuss quantitatively the limit of sorting specific images and the gain in terms of useful information with respect to normal imaging.

Methods

Fig 1 shows the scheme of lenses and phase elements based on an OAM sorter [1] [2] that should allow us to improve the recognition of specific proteins.

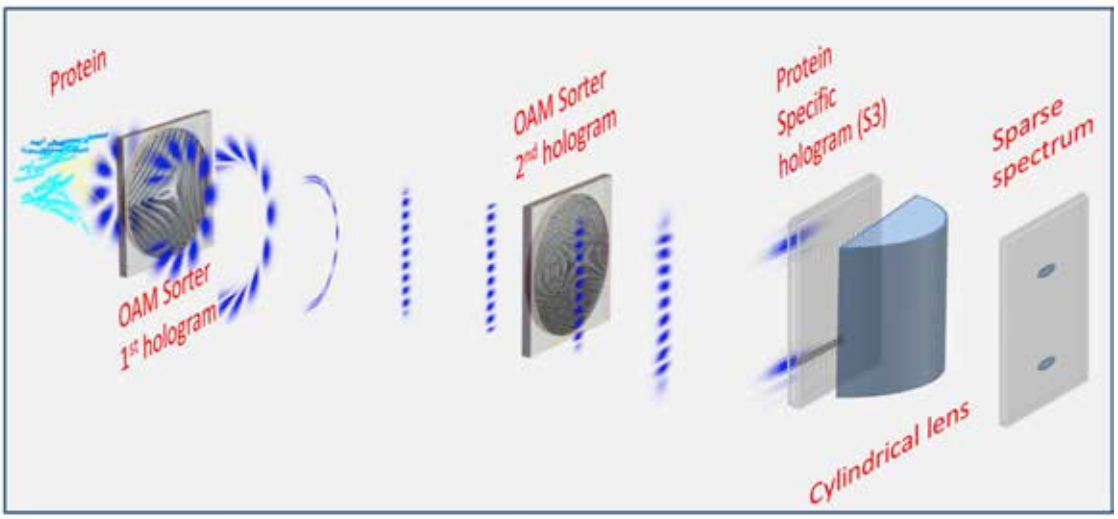

Fig. 1 Scheme of the electro-optic configuration for a 3 element generalized sorter (based on OAM sorter) that permits a single protein identification regardless of the in plane rotation.

The peculiar problem about proteins is that we are interested in their structure regardless of their in plane (and out of plane) orientation. A part of the information in imaging is therefore lost in encoding the orientation information.
The OAM sorter can suggest how to circumvent at least part of the problems. The OAM sorter uses a conformal transformation to lead to the angular basis formed by OAM, indicated by the integer quantum number m, and Log-Radial momentum here simply indicated as p. As a consequence, it transforms a vortex beam in a peak in the OAM space. It should be then noticed that a rotation $\Delta\theta$ produces an extra phase in each OAM peak in the OAM spectrum equal to $\phi = \ell\Delta\theta$ but no amplitude change. This is analogous to the fact that the intensity in a diffraction pattern is independent of the protein x,y position.
If we suppose that we can know a-priori the position of the protein for example by a low mag imaging, the problem remains on the rotation. However, the problem can be further developed by enforcing sparsity of the representation for specific proteins. To do this, without losing the desired property of rotational invariance, we can add a specific element S3 at the end of the sorter in the plane of the OAM and p as in Fig 1
In fact, we can add a phase element and a cylindrical lens in order to diffract only in the p direction. This can be obtained by a stigmator coupled with a lens.
The aim of this kind of process is to produce a sorter for the following prototype of wavefunction:

$$\psi_m = R_m(\rho)\exp(im\theta)$$

Where $R_m(\rho) = \int \psi_{ew}(\rho,\theta)\exp(im\theta)d\theta$. Where ψ_{ew} is the aimed wavefunction after our best guess or a-priori knowledge of the protein that needs to be tested. In practice such eigenstates are vortexes in the azimuthal part but they have a radial function that is fitted to the protein.
The spectrum after an ideal OAM sorter is $\widetilde{\psi}_{EW}(p,m) = \sum \widetilde{R}_m(p)\delta(m-m')$
The way to sort these state is to use the additional phase element S3 to compensate for the phase of $\widetilde{R_m(p)}$ and ideally obtain a diffraction after the third element in the mixed real, reciprocal space as $\widetilde{\psi}_{EW}(p,m) = \sum \delta_m(\rho)\delta(m-m')$.

Results

Fig 2 show two protein images. The phase of the element S3 has been optimized to recognize the protein as in Fig 2, so when such a protein is sent to the new generalized sorter as in Fig 1 we obtain a very sparse and protein specific response that can be safely recognized with 10 e/A^2 (Fig 2b) or even only 1 e/A^2 (Fig 2c). Of course the result is insensitive to the in-plane protein orientation.
Conversely if a wrong wave as in Fig 2d is sent to the above lens system the image is completely different and contains almost no feature.

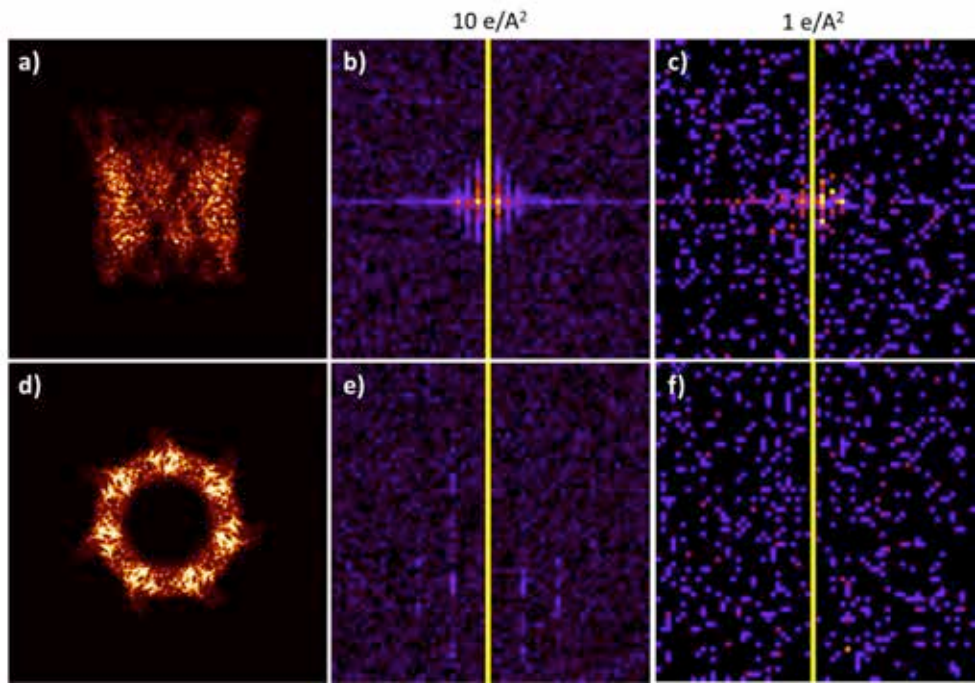

Fig 2: Two possible protein images (a,d) to be sorted by a generalized sorter. The sorter produces a well-defined pattern when the “right protein” is introduced (b,c) but a featureless image if the “wrong” wave is analyzed (e,f).

Discussion

The above example shows an explicit example of basis change that partially optimizes the recognition of a protein. Can we do better? Can the protein image be transformed to a peak specific for that protein while a different protein transforms to a different one?
We found that when the protein are weak phase objects such transformation is in general impossible: in other words the proteins are not sufficiently different. The main limitation is indeed that a large part of the intensity is lost in the central peak that contains almost no information.
Still with the appropriate metrics we can demonstrate a quantitative advantage of this method in recognizing specific proteins.

References

[1] G. C. Berkhout, M. P. Lavery et al Phys. Rev. Lett. **105**, 153601 (2010).
[2] V.Grillo, A.H. Tavabi et al Nature Comm. **8**, 15536 (2017)

Innovative 4D STEM approaches towards mapping transient electrical fields and strain at the nanoscale

G. Guzzinati[1] A. Béché[1], J. Krehl[2], J. Schultz[2], A. Lubk[2], C. Mahr[3], A. Rosenauer[3] and J. Verbeeck[1]

[1]EMAT, University of Antwerp, Antwerp, Belgium
[2] IFW Dresden, Dresden, Germany
[3] Institute for Solid State Physics, University of Bremen, Bremen, Germany
[4] MAPEX Center for Materials and Processes, Univ. of Bremen, Bremen, Germany

E-mail: giulio.guzzinati@uantwerpen.be

Introduction

The increasing ability to quickly process large amounts of data is changing the field of Transmission Electron Microscopy by paving the way to a variety of new measurement techniques, including those based on so-called 4D STEM / diffraction imaging. There, an entire diffraction pattern is recorded for each point in a raster scan. 4D STEM is now rapidly gaining popularity, thanks to the development of faster and more sensitive direct detection cameras. In this lecture, we will introduce some more unconventional examples of this approach.

Results

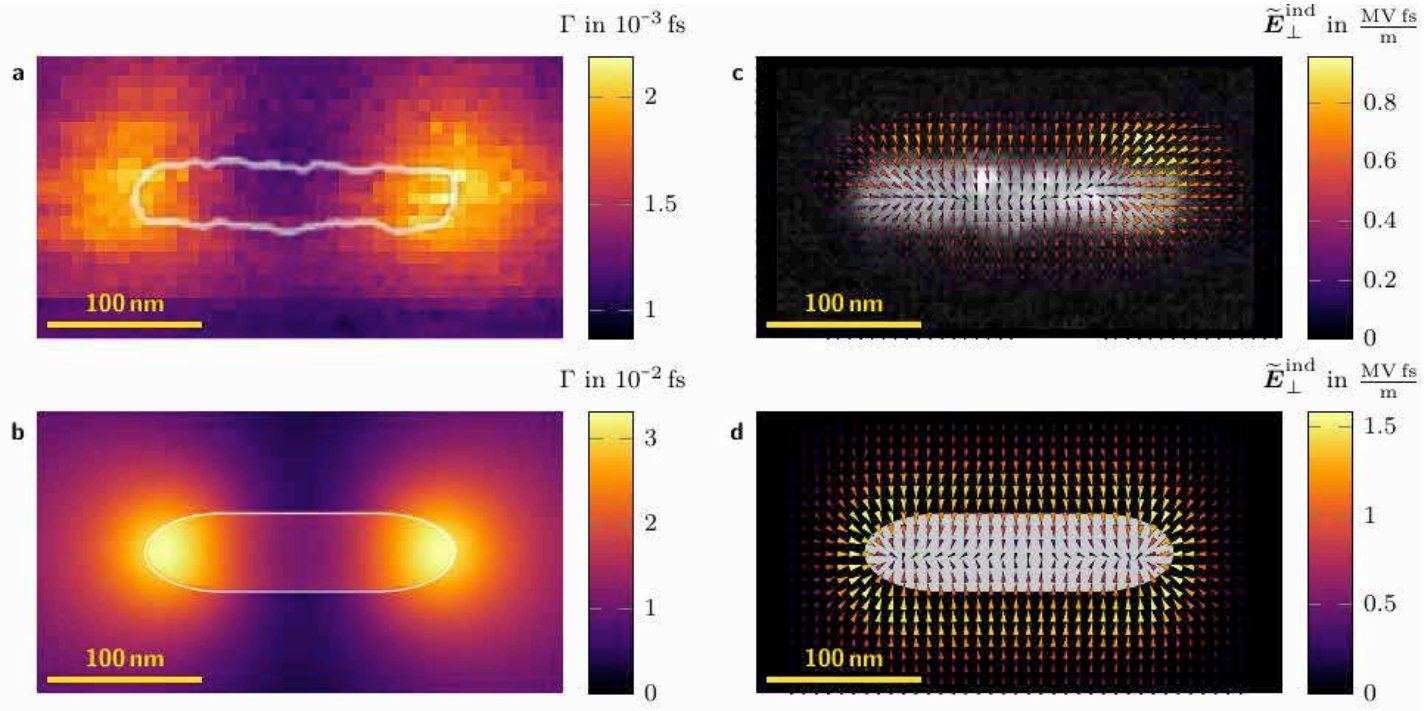

Fig. 1 Experimental and simulated maps of loss probability and transverse fields for a plasmonic excitation from [1].

In a first 4D STEM setup, an energy filter is used to record energy filtered diffraction patterns i.e. the momentum distribution of inelastically scattered electrons. Analogously to how conventional DPC is used to measure transverse electrostatic fields, this technique gives quantitative access to the transverse fields of plasmonic excitations, a previously inaccessible property.We will present here the experimental realization of this technique on an Al nanorod (Fig. 1) and discuss its the further possibilities.

In a second part, a custom made annular aperture is introduced in the condenser plane of a TEM. This creates conical illumination conditions, analogue of precession electron diffraction, where, however, the illumination from all directions is present at once. Such setup is particularly interesting to quantitatively measure strain while minimizing costly hardware modifications to the microscope. The resulting patterns, composed of overlapping rings, are much harder to interpret than the ones acquired in the more conventional Nanobeam Electron Diffraction (NBED) setup. A dedicated procedure is presented, capable of extracting strain information from the diffraction patterns and potentially applicable in real time. The method is also shown to outperform conventional NBED, and to approach the performance of nano beam precession electron diffraction (Fig. 2).

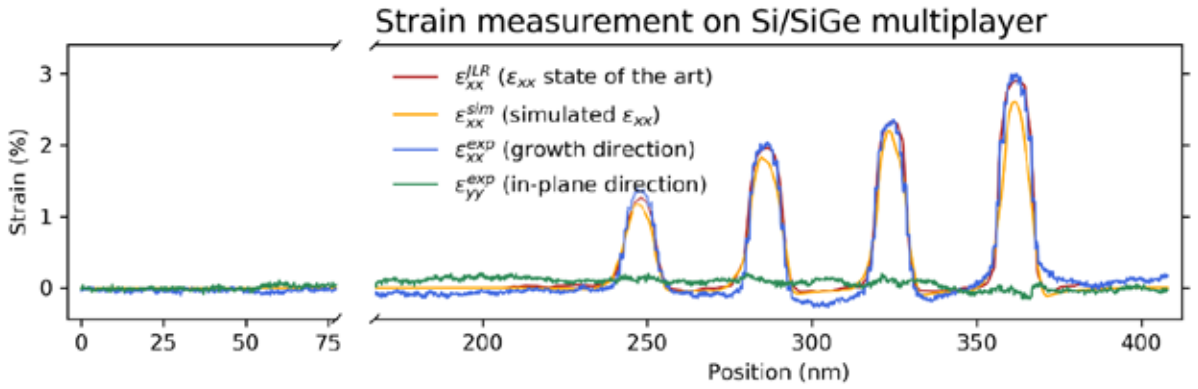

Fig. 2 Experimental and simulated strain in a Si/SiGe multilayer test structure, also compared with state of the art data from the literature collected using precession electron diffraction [2,3]

References

[1] Krehl et al., Nature Communications, 9, 4207 (2018)

[2] Rouviere et al. Applied Physics Letters 103, 241913 (2013)

[3] Guzzinati et al., Applied Physics Letters, in review, arXiv:1902.06979 (2019)

Controlled generation of higher order vortex arrays using a Microlens array

B. S. Harshith[1, 2, *] and G. K. Samanta[1]

[1]Photonic Sciences Laboratory, Physical Research Laboratory, Navrangpura, Ahmedabad, Gujarat 380009, India,
[2] Indian Institute of Science Education and Research Pune, Dr. Homi Bhabha Road, Pashan, Pune, Maharashtra 411008, India,
**e-mail: ssharshith.bachimanchi@gmail.com*

Optical Vortices, doughnut-shaped optical beams carry orbital angular momentum (OAM) per photon. Typically, optical vortices are generated by impinging a helical phase $exp(il\varphi)$, (where φ is the azimuthal phase and l is the toplogical charge or the order of a vortex beam) to the Gaussian beams with help of spatial mode converters including spiral phase pales (SPP), q-plates and holographic spatial light modulators. Since their discovery, the vortex beams have found a great deal of attention for their wide variety of applications in particle trapping and micromanipulation, quantum information, and lithography [1]. However, the recent advancements on multiple particle trapping, fast micromachining and multiplexing in quantum information, demand an array of vortex beams in a simple experimental scheme. Efforts have been made to generate optical beamlet arrays from SLMs, fresnel zone plates and ampltide gratings, however, the power loss and the stringent dependence of input strucutral parameters, often offer limited or no control on the properties of the arrays. Here we report, a simple experimental scheme based on a dielectric microlens array (MLA) and a plano-convex lens, to generate high power array beams carrying the spatial property of the input beam. The schematic of the experimental scheme in shown in Fig.1.

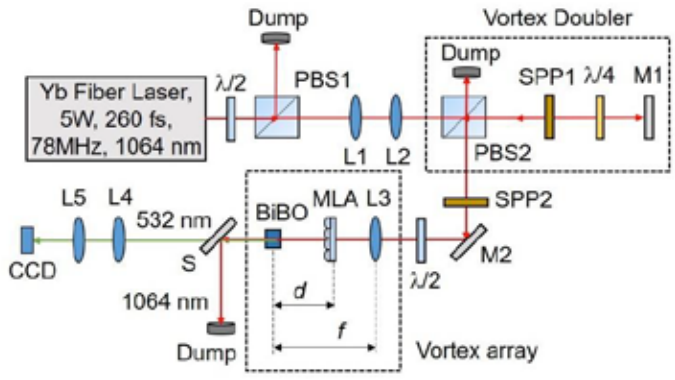

Fig. 1. Schematic of the experimental setup for the generation of vortex arrays.

A 5 W, Yb-fiber laser with spectral linewidth of 15 nm centred at 1064 nm providing femtosecond pulses of width ~260 fs at a repetition rate of 78 MHz is used as the pump laser. The input power to the setup is varied using a half waveplate (λ/2) and polarizing beam splitter cube (PBS1). The input beam is expanded and collimated using a telescopic combination of lenses, L1 and L2 of focal lengths, f = 50 mm and f =100 mm, respectively. Using two spiral phase plates, SPP1 and SPP2, with phase winding corresponding to vortex orders l= 1 and l= 2, respectively and the vortex doubler [2] comprised with the PBS2, quarter-wave plate (λ/4) and mirror, M1, we have converted the Gaussian beam into vortex beams of orders, l_p=1 - 6. The pump vortex beam of order, l_p, on propagation through the lens L3 of focal length, f= 300 mm, and the microlens array (MLA) (Thorlabs MLA 300-14AR) consisting with 391 lenslets of focal length, f_{MLA} =18.6 mm resembling a 2D sinusoidal phase pattern, is Fourier transformed to produce vortex array at the back focal plane of lens L3. The distance, d, of the MLA from the back focal plane of L3

modulates the pitch of the vortex array and the focal length, f, of the lens L3 determines the diameter of individual vortices in the array. Additionally, a 1.2 mm thick BiBO crystal [2] cut for type-I phase matching is placed at the Fourier plane to frequency-double the vortex arrays at 1064 nm into green vortex arrays at 532 nm. The λ/2 before the lens, L3, controlls the polarization of the input beam with respect to the crystal orientation for phase-matching.The green beam is extracted from the undepleted pump using the wavelength separator, S, and subsequently imaged in the CCD plane using the lenses L4 and L5, each of focal lengths, f = 150 mm respectively.

To understand the formation of vortex arrays, we have approximated the MLA as a 2D sinusoidal phase grating of pitch, Λ and sinusoid amplitude thickness, s. According to Fourier transformation theory [3], any object (MLA) can be Fourier transformed at the back focal plane of a lens of focal length f, by placing the object after the lens at an arbitrary distance, $(f-d)$ after the lens (see Fig. 1). Here, d is the distance of the MLA from the back focal plane. The transverse field amplitde distribtuion of vortex arrays at the back focal plane of lens L3 for an input Gaussian embedded vortex beam of order, l, can be written as [3],

$$E \sim \sum_{p,q=-\infty}^{\infty} J_{p,q}(m)\ \delta_{x,y}(d,\lambda)\ \otimes\ \mathcal{F}(E_l) \tag{1}$$

where,

$$\delta_{x,y}(f,d,\lambda) = \delta\left(\frac{1}{f\lambda}\left[x - p\left(\frac{\lambda d}{\Lambda}\right)\right],\ \frac{1}{f\lambda}\left[y - q\left(\frac{\lambda d}{\Lambda}\right)\right]\right) \tag{2}$$

$$\mathcal{F}(E_l) = \left[\frac{\left(r\sqrt{2}\right)^{l}}{(w_0)^{l+1}} exp\left(\frac{-r^2}{{w_0}^2}\right) exp(il\varphi)\right] \tag{3}$$

$$J_{p,q}(m) = J_p\left(\frac{m}{2}\right) J_q\left(\frac{m}{2}\right) \tag{4}$$

As evident from Eq. (1), the convolution of $\mathcal{F}(E_l)$, with the 2D delta function, $\delta_{x,y}(d,\lambda)$, as represented by Eq. (2), replicates $\mathcal{F}(E_l)$ at positions determined by the individual delta peaks as a function of the input wavelength, λ, and distance, *d*. Therefore, one can generate array beams of desired intensity distribution by using suitable spatial profile of the input beam. Given that $\mathcal{F}(E_l)$, the Fourier transform of input Gaussian embedded vortex beam of order l, as presented in Eq. (3) resulting into a vortex beam with Gaussian beam waist, $w_0 = f\lambda/\pi w_g$ (w_g is the beam width of input vortex beam on to the lens L3), we expect an array of vortex beams at the Fourier plane of lens, L3. On the other hand, $J_{p,q}(m)$, the Bessel functions of first kind of orders *p* and *q* as represented in Eq. (4), determine the overall intensity distribution of the vortex array as a function of the phase contrast, *m*, of the grating. Therefore, by changing the value of $m = 2\pi(n-1)\,s/\lambda$, with the change of any of the parameters, *s* and λ, one can control the overall intensity distribution of the vortex array. To confirm the control in overall intensity pattern of the vortex array, we have used a MLA of lenslet thickness, s = 1.31 μm and pitch, Λ = 300 μm and numerically calculated the variation in the intensity pattern of vortex arrays for input wavelengths, λ=1064 nm and λ= 532 nm, corresponding to the phase contrasts, m = 1.11π and m = 2.27π respectively. The results are shown in Fig. 2. As evident from the first

column, (a)-(b), of Fig. 2, we clearly see the change in the overall intensity pattern of the vortex array with the change in the phase contrast, m, of the MLA. Similarly, we have experimentally recorded the intensity pattern of the vortex array by using laser beams at 1064 nm and 532 nm as shown in second column, (c)-(d), of Fig. 2, in close agreement with the theoretical results. It is also interesting to note that, the decrease in the pitch, $\Lambda_{exp} = \lambda d/\Lambda$, of the vortex array with the decrease of laser wavelength from 1064 nm to 532 nm, increases the total number of vortices in the array. In addition, the same intensity pattern can also be achieved by varying thickness, s, of the lenslets of MLA. To verify the control in the pitch and sizes of the vortex arrays, we have positioned the MLA at different positions after the lens L3 and recorded the patterns. We have measured that the pitch of the vortex array, Λ_{exp}, increases from 434 μm to 866 μm with the increase of MLA separation, d, from 120 mm to 240 mm, while maintaning the size of the vortex at a constant diameter of ~ 430 μm. Similarly, by changing the focal length of lens L3 from f=50 mm to f = 300 mm, we were able to control the vortex sizes in the array from 103 μm to 460 μm for the vortex array of order, l= 1. With successful generation and control of the vortex arrays of different orders, we have also studied their frequency-doubling characteristics, by placing the 1.2 mm BiBO crystal at the Fourier plane. As evident from first column, (a,b), of Fig. 3, both pump and SH beam have array of vortices. Using tilted lens technique to split the vortices into $n = l + 1$ number of charactersitic lobes as shown in second column, (c,d), of Fig. 3, we confirm the pump vortex order to be 6 and the SHG vortex orders to be 12, twice that of the pump vortex order.

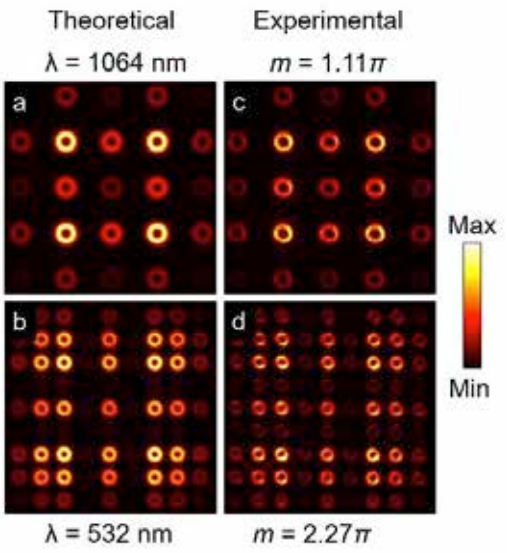

Fig. 2. Intensity distributions of vortex arrays for different values of phase contrast, *m*.

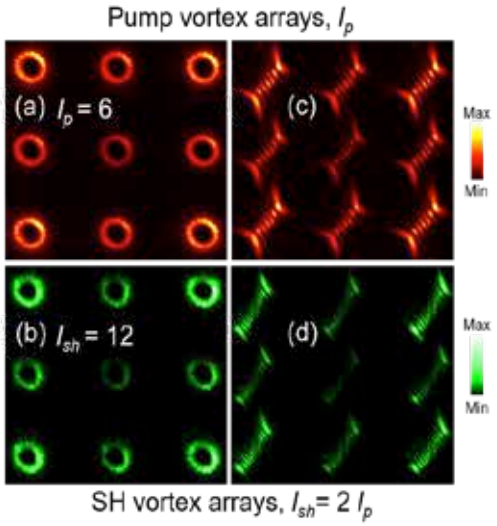

Fig. 3. Intensity distributions of vortex arrays for different values of phase contrast, *m*. mention about each column.

In conlusion, we have demonstrated a generic experimental scheme to generate array beams of any desired spatial profile. Using vortex beam as input, we have generated array of vortex beams of different orders and successfully controlled the parameters of the vortex array. Further results on frequency doubling characteristics will be presented.

References:

1. Omatsu, T., Chujo, K., Miyamoto, K., Okida, M., Nakamura, K., Aoki, N. and Morita, R. Opt. Express, 18, 17967-17973 (2010).
2. Apurv Chaitanya, N., Aadhi, A., Jabir, M. V., & Samanta, G. K. *Opt. Lett.* **40**, 2614-2617 (2015).
3. Goodman, J. W. Introduction to Fourier Optics. 81-83, 106-107 (2005).

Polarization-Controlled Photon-Induced Near-Field Electron Microscopy

T. R. Harvey[1], J.-W. Henke[1], M. Sivis[1], A. Feist[1], H. Lorenço-Martins[1], O. Kfir[1] and C. Ropers[1]

[1] *IV. Physical Institute, University of Göttingen, Göttingen, Germany*

e-mail: tyler.harvey@uni-goettingen.de

Introduction

Although absorption or emission of a single photon by an electron is forbidden in free space by energy-momentum conservation, this interaction is possible in the presence of a material. A material breaks translation symmetry and allows for coupling between electron momentum and the electromagnetic field amplitude [1, 2, 3, 4]. The strength of this coupling depends on the shape and optical response of the material, as well as the incident optical power. Because electron beams can be focused to sub-nanometer spots in modern electron microscopes, it is possible through this interaction to probe the optical response of materials with nanometer spatial resolution. This technique, called photon-induced near-field electron microscopy (PINEM), can be employed to efficiently image plasmonic modes, electronic states, magnetic materials, molecules and cells [5] with arbitrary incident polarization. In particular, circularly-polarized-photon-induced near-field electron microscopy offers access to chiral optical states in the electron microscope.

Chirality is central to a number of open scientific questions and technologically relevant materials, including broken symmetry in the biochemistry of life, CP violation, magnetic skyrmions and metamaterials. Three-dimensional chirality can only be characterized by tomography or with a probe that has controllable helicity. The latter approach allows for investigation of chiral quantum states and transitions that have no direct link to three-dimensional structure. Some progress has been made toward such a technique with electron vortices [6, 7, 8]. Another approach is to use electrons to probe the interaction between circularly polarized light and chiral materials. This technique expands the capabilities of transmission electron microscopes by offering direct information about chirality.

Methods and Results

In order to demonstrate the technique, we prepared left- and right-handed spiral structures milled into gold as a prototypical chiral specimen (see Fig. 1a). We illuminated the spirals with an 800 nm wavelength optical field with peak strength 3.5 $\frac{\mathrm{V}}{\mathrm{nm}}$. We then probed the interaction of this optical field with the structures using pulsed electrons in the Göttingen ultrafast transmission electron microscope [9]. We raster-scanned the focused electron beam over the specimen and record an electron energy spectrum at each probe position. From this three-dimensional dataset, we calculated the coupling constant, g, at each probe position (see Fig. 1b). This coupling constant is related to the strength of the optical near field. We measure the dichroism, Δg, as the difference in g for incident left- and right-circularly polarized light (see Fig. 1d). We also performed finite-element simulations of the same structure and calculated g and Δg (see Figs. 1c and 1e).

Both simulation and experiment show clear dichroism in the average Δg across the structure, as well as spatial variations linked to the particular shape of this structure.

Discussion

We have demonstrated that PINEM with circularly polarized light offers direct access to chirality. With the addition of control of the incident optical wavelength, this technique will be able to offer full spectroscopic and high-spatial-resolution characterization of chiral nanostructures, electronic states, and potentially molecules. This new capability adds chiral sensitivity to the wide range of characterization techniques already possible in electron microscopes.

References

[1] B. Barwick et al., *Nature* **462**, 902 (2009).

[2] S. T. Park et al., *New J. Phys.* **12**, 123028 (2010).

[3] A. Asenjo-Garcia et al., *New J. Phys.* **15**, 103021 (2013).

[4] A. Feist et al., *Nature* **521**, 200 (2015).

[5] M. Kaplan et al., *Angew. Chem. Int. Ed.* **56**, 11498 (2017).

[6] A. Asenjo-Garcia et al., *Phys. Rev. Lett.* **113**, 066102 (2014).

[7] T. Harvey et al., arXiv:1507.01810 (2015).

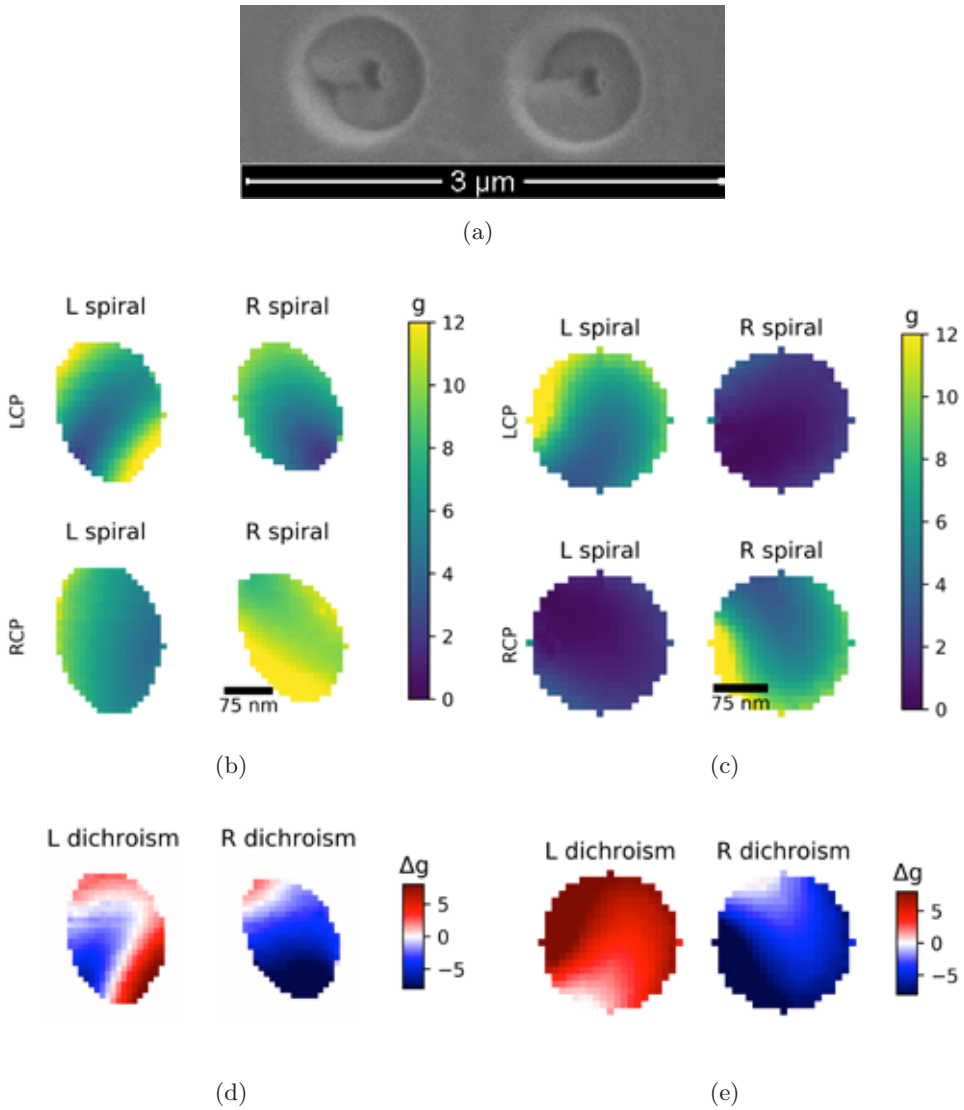

Figure 1: (a) Experimentally measured coupling constant, g, on left-handed spiral (L spiral) and right-handed spiral (R spiral) with left-circularly-polarized light (LCP) and right-circularly-polarized light (RCP). (b) Coupling constants calculated by finite-element simulation. (c) Experimentally measured dichroism, Δg, on left-handed spiral (L spiral) and right-handed spiral (R spiral), calculated as the difference between LCP and RCP g in (a). (d) Simulated dichroism.

[8] G. Guzzinati et al., *Nat. Comm.* **8**, 14999 (2017).

[9] A. Feist et al., *Ultramicroscopy* **176**, 63 (2017).

Tuning of Off-axis Vortex Beam using Pancharatnam-Berry Phase

Philip Jacob, Satyajit Maji and Maruthi M Brundavanam

Department of Physics, Indian Institute of Technology Kharagpur, West Bengal, India

e-mail: : bmmanoj@phy.iitkgp.ac.in

Introduction

In the 27 years after the idea of optical vortex (OV) beams carrying orbital angular momentum (OAM) was first introduced by Allen *et al.* [1], the study of such beams characterized by phase singularities and azimuthal phase dependences has developed significantly. Of recent, the properties of OV beams with non-integer average OAM are being investigated, due to the great potential of such beams in applications that include optical micro-manipulation [2], OAM entanglement [3], and anisotropic phase contrast imaging [4]. An optical vortex beam having non-integer average OAM can be generated using a fractional helicoidal phase step [5], using a spiral phase plate which has been shifted from the center of a Gaussian beam [6], or by superposing laser beam modes with different integer values of OAM [7]. The topological transformation of OV beams from fractional fork holograms induced by the modulation of Gouy phase has been demonstrated in a recent study in our group [8].

In this study, off-axis OV beams are generated by superposing a laser beam in the fundamental Gaussian mode on a symmetric OV beam containing a point of phase singularity at the beam center. We show that the radial position of the vortex can be controlled conveniently by varying the relative intensity of the Gaussian beam. In a previous study [9], we have demonstrated how the azimuthal position of the vortex can be controlled by introducing shifts in the Pancharatnam-Berry(PB) phase [10,11], which is the geometric phase associated with transformations in polarization-state space .

Methods

A Mach-Zehnder interferometer set-up is utilized to superpose a Gaussian beam on an OV beam. A spatial light modulator embedded with a computer generated hologram of a forked diffraction pattern is placed in one arm of the interferometer to generate an OV beam. In the other arm, where the beam propagates in the fundamental Gaussian mode, a polarizer pair (P_1 and P_2) is used to tune the beam intensity, while a quarter-wave plate(Q) - polarizer(P) - half-wave

plate(H) combination is used to introduce shifts in PB phase.

P_1 is oriented such that its pass axis makes an angle ψ with the horizontal while the pass axis of P_2 lies along the horizontal. The incident beam is in a state of horizontal linear polarization. On passing through P_1, the intensity of the beam reduces by a factor of $cos^2\psi$ and its axis of polarization is rotated by ψ. On passing through P_2, the intensity is further reduced by a factor of $cos^2\psi$ as the beam returns to its initial state of polarization. On passing through the Q-P-H combination, the beam's polarization state is transformed cyclically, first to right circular polarization, then to linear polarization with the polarization axis making an angle θ with the horizontal, and finally back to horizontal linear polarization. On representing the states of polarization as points on the Poincaré sphere, the magnitude of geometric phase can be equated to half the solid angle subtended by the closed loop of polarization states, at the center of the sphere. The experimental set-up is not shown here.

Results

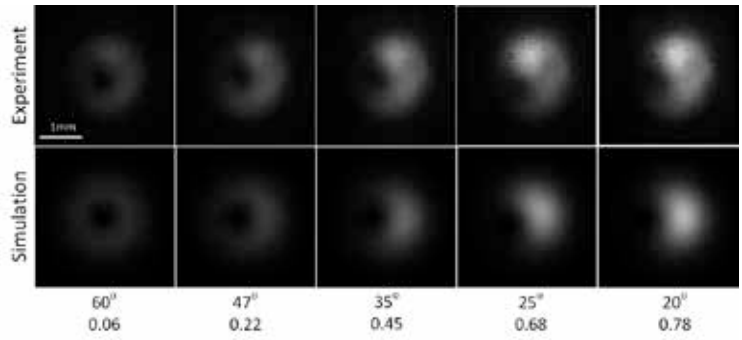

Figure 1: Variations in radial position of vortex as a function of ψ

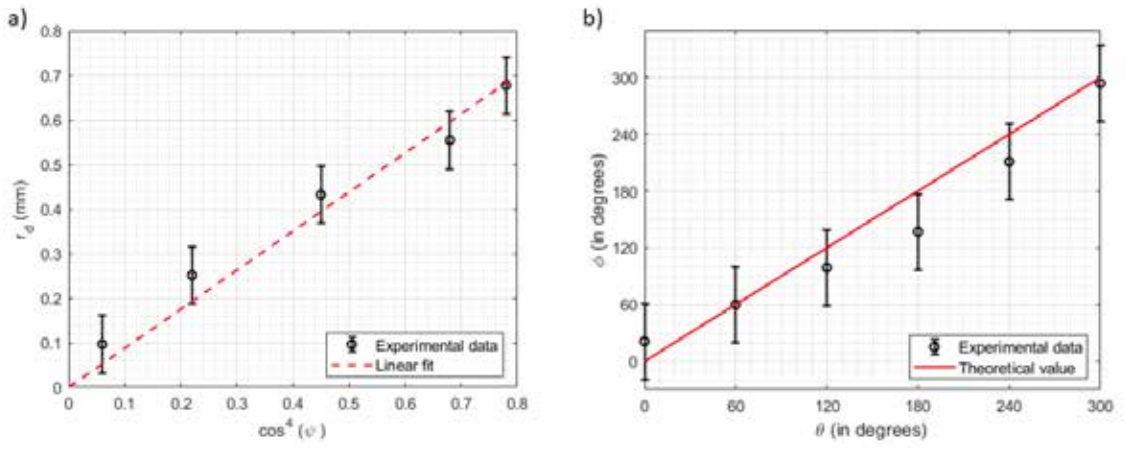

Figure 2: a) Radial position of vortex (r_0) vs. $\cos^4\psi$, b) Azimuthal position of vortex (ϕ) vs. θ

The position of the vortex is tuned experimentally, and the resulting intensity pattern is captured using a Charge Couple Device (CCD) camera. Experimental results are found to be consistent with the results obtained from numerical simulations. The radial displacement of the vortex from the center of the beam (r_0) is plotted against $\cos^4\psi$. The polarizers P_1 and P_2 each reduces the intensity by $\cos^2\psi$. Thus, the relative intensity of the Gaussian beam mode will be directly proportional to $\cos^4\psi$. As a result, a plot of r_0 with $\cos^4\psi$ accurately reflects the relationship between the radial displacement of the vortex and the relative intensity of the Gaussian beam. The plot (Figure 2a) suggests the existence of a linear relationship between r_0 and $\cos^4\psi$.

Conclusion

An off-axis OV beam is generated by superposing a fundamental Gaussian beam on an optical vortex beam of unit topological charge, with a Mach-Zehnder interferometer set-up. The position of the vortex is controlled by suitably tuning the intensity and PB phase of the Gaussian beam in one branch of the interferometer. The effect of varying the position of the off-axis vortex on the distribution of the transverse component of the beam's linear momentum would be investigated as an extension to the current study.

References

[1] L. Allen *et al.*, Phys. Rev. A **45**, 8185 (1992)

[2] S. H. Tao *et al.*, Opt. Express **13**, 7726 (2005)

[3] S. S. R. Oemrawsingh, Phys. Rev. Lett. **95**, 240501 (2005)

[4] J. Wang *et al.*, Scientific Reports **5**, 15826 (2015)

[5] M. V. Berry, J. Opt. A: Pure Appl. Opt. **6**, 259 (2004)

[6] Kotlyar *et al.*, Opt. Lett. **42**, 139 - 142 (2017)

[7] A. Valziri *et al.*, J. Opt. B: Quantum Semiclass. Opt. **4**, S47 (2002)

[8] S. Maji *et al.*, Opt. Lett. **44**, 2286-2289 (2019)

[9] P. Jacob *et al.*, Int. Conf. on Optical Angular Momentum (ICOAM-2019)

[10] S. Pancharatnam, Proc. Indian Acad. Sci. **A44**, 247 (1956)

[11] M. V. Berry, J. Mod. Opt. **34**, 1401 (1987)

Optimizing Blazed Efficiency of Electron Diffractive Optics with Ion Beam Gas-Assisted Etching for Structured Electron Spectroscopy

C. W. Johnson[1], T. R. Harvey[2] and B. J. McMorran[1]

[1]Department of Physics, University of Oregon, Eugene, Oregon, 97403, USA

[2]IV. Physical Institute, Georg-August-Universität, Göttingen, Germany

e-mail: cwj@uoregon.edu

Introduction

Structured electrons, specifically electron vortex beams (EVBs) that carry quantized amounts of orbital angular momentum (OAM), have had multiple proposed uses for studying new degrees of freedom in materials outside of what is detectable using conventional electron microscopy. One proposed use is to study chiral materials, in a way analogous to circular dichroism in light optics, with magnetic and plasmonic interactions [1]. However, advances exploiting these techniques have been hindered by the lack of efficiency, as well as modal purity in the generation EVBs. Here, we over come this barrier by adding a gas-assisted etching (GAE) process to the focused ion beam (FIB) milling technique to fabricate the largest and highest reported efficiency holograms that produce off-axis EVBs [2, 3]. Furthermore, we apply a variant to the theoretical model from Asenjo-Garcia and Garcìa de Abajo [4] that predicts plasmonic dichroism in chiral clusters of metallic nanoparticles to interperet experimental results [5].

Methods

FIB GAE keeps all the positive attributes of FIB milling such as reproducibility, and spatial depth variability, while simultaneously increasing resolution, and scalability, as well as decreasing process time, defect implantation, and material redeposition [6]. Consequently, we can produce 30-50 µm diameter holograms with binary, sinusoidal, and blazed grating profiles with as small as 100 nm pitch.

In addition to producing EVB probes with higher efficiency, we also develop new theoretical tools to understand how they transfer OAM to excited modes in target samples. Modelling a chiral cluster of Al nanparticles as point dipoles, we use Fermi's golden rule to calculate the

energy dependent transition probability $\Gamma(E)$ to transfer one $\hbar$ of OAM from an $\langle L_z \rangle = \hbar$ EVB to the cluster of nanoparticles via the Coulomb interaction Hamiltonian.

Results

We present arrays of binary, sinusoidal, and blazed 12 µm diameter, 200 nm pitch straight gratings with increasing groove depth exhibiting diffraction efficiencies relative to the total transmitted current near the theoretical maximum for pure phase gratings. The blazed grating arrays exhibit up to 76% relative diffraction efficiency into one of the 1st diffraction orders, and we have made 30 µm diameter, 1 OAM gratings at 200 nm pitch with as high as 62% relative diffraction efficiency into one of the 1st diffraction orders Figure 1.

These gratings can be used to produce EVBs for improved chiral dichorism experiments. In our model of plasmons excited by EVBs, we show that when geometry and nanoparticle sizes in experimental systems are input to the model, the predicted energy dependent transition probability shows a good qualitative agreement to the experimental spectra Figure 2.

Discussion

Provided this nanofabrication method, able to make highly efficient EVB producing holograms large enough to fill a condenser aperture of an electron microscope, coupled with a theoretical model agreeing with experiment results for plasmonic dichroism, we expect an increase in the signal-to-noise ratio enough to be able to verify all the plasmonic dichroism properties predicted in chiral clusters of metallic nanoparticles. More broadly, these highly efficient holograms could have a significant impact in structured electron microscopy, spectroscopy and interferometry, as well as illuminating the physics of fundamental properties of free electrons.

References

[1] S. M. Lloyd, *et. al.*, Rev. Mod. Phys., 89, 035004 (2017)

[2] V. Grillo, *et. al.*, Appl. Phys. Lett., 104, 043109 (2014)

[3] T. R. Harvey, *et. al.*, New J. of Phys., 16, 093039 (2014)

[4] A. Asenjo-Garcia and F. J. Garcìa de Abajo, Phys. Rev. Lett., 113, 066102 (2014)

[5] T. R. Harvey, *et. al.*, arXiv:1507.01810 (2015)

[6] I. Utke, *et. al.*, J. of Vac. Sci. Tech. B, 26, 1197-1276 (2008)

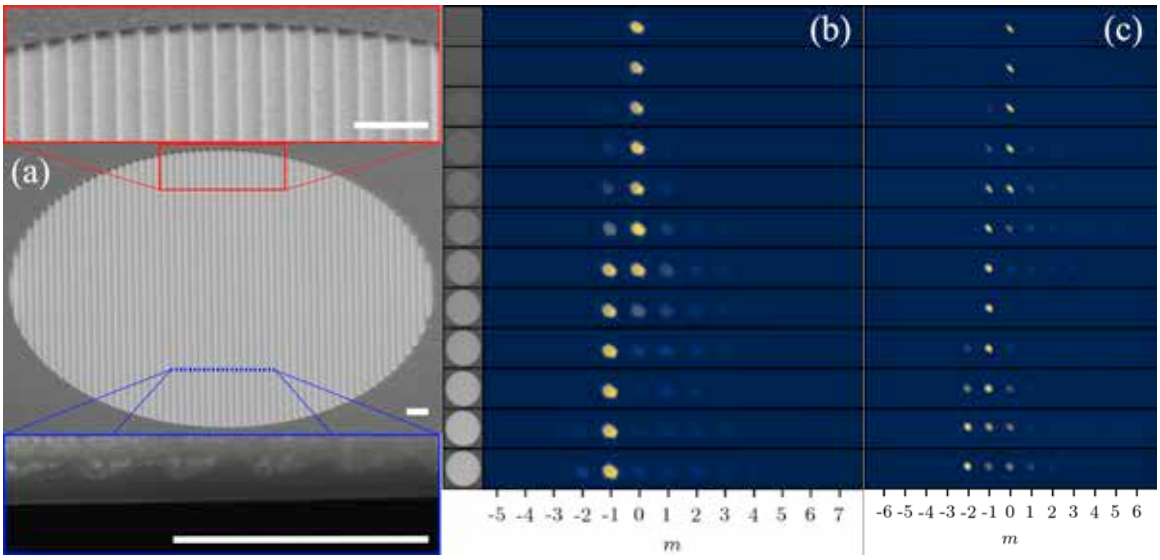

Figure 1: (a) SEM micrograph of blazed grating view, all scale bars are 600 nm. (Red inset) Zoomed in portion of (a). (Blue inset) Example cross section with Pt cap on top of perpindicular FIB milled cut with vacuum under grating. (b) Normalized far-field diffraction patterns of 12 blazed gratings with increasing mill depth from 4-64 nm at 300 keV in a TEM. (c) Same as (b), but taken at 80 keV.

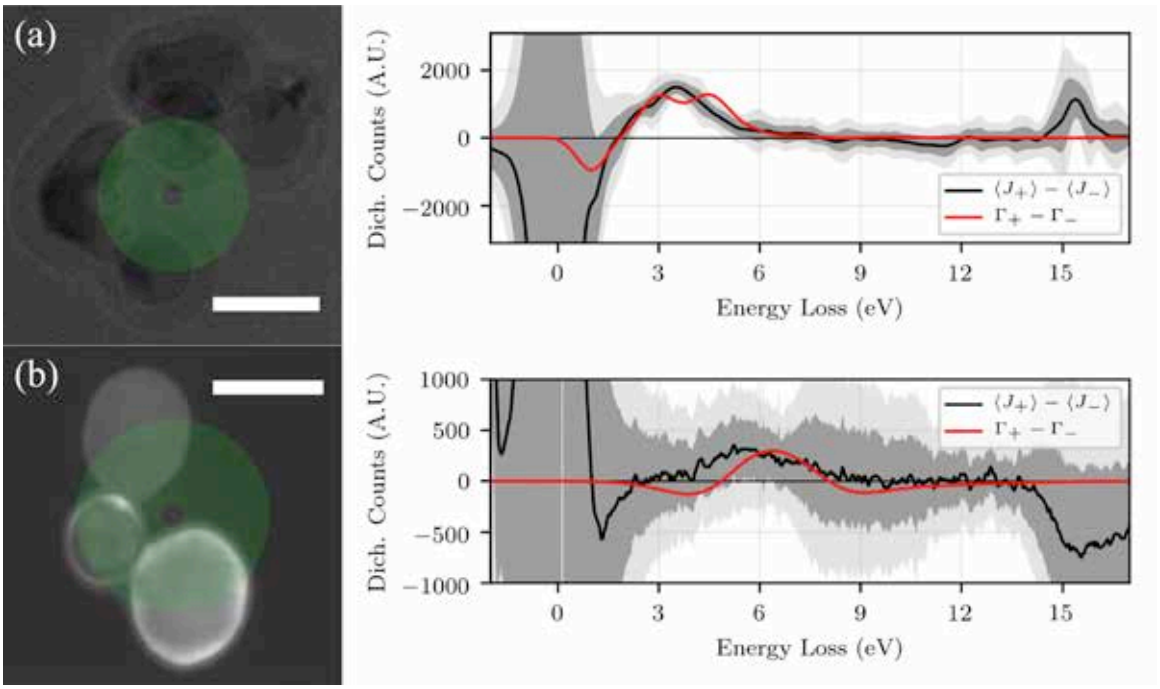

Figure 2: (a) TEM micrograph of Al nanoparticle cluster, scale bar is 100 nm. Green annulus is position of EVB in experiment. (Right) Experimental dichroic EELS spectrum with the difference between measured counts $\langle J_\pm(E) \rangle$ for $\langle L_z \rangle = \pm\hbar$ EVBs, dark gray region is within one standard deviation, light gray is within two. Red curve is the predicted dichroic spectrum from the difference between energy dependent transition probabilities $\Gamma_\pm(E)$. (b) Different experimental cluster of alumninum nanoparticles exhibiting extinsic dichroism, scale bar is 50 nm.

Spontaneous radiation from a wide quantum electron beam

Aviv Karnieli,[1,*,†] Roei Remez,[1,†] Sivan Trajtenberg-Mills,[1] Niv Shapira,[1] Ido Kaminer,[2] Yossi Lereah,[1] and Ady Arie[1]

[1]School of Electrical Engineering, Fleischman Faculty of Engineering, Tel Aviv University, Tel Aviv, Israel

[2]Department of Electrical Engineering, Technion–Israel Institute of Technology, Haifa 32000, Israel

† These authors contributed equally

[*]Corresponding author: avivkar1@gmail.com

Introduction

Spontaneous radiation from free electrons has been thoroughly investigated over the years, with implications on both fundamental science and technology. Although it can be almost fully explained by a classical theory of radiation excited by the motion of point charges, the wave nature of the particles is manifested only in the quantum theory. Smith-Purcell radiation (SPR), in which a swift electron emits light when passing next to a grating, has been the subject of intense research since its discovery in 1953 [1], permitting light sources in deep-UV and X-ray. Many classical theories were developed to explain this phenomenon [2], where the electron is described as a point charge. Quantum theories mainly focused on the dispersion relation, or the point-particle limit of electrons having some small-ranging transverse wavefunction [3] or for a longitudinal wavefunction [4]. The Maxwell-Schrodinger approach, which couples the Schrodinger wave function for the electron and Maxwell's equations for the radiation by identifying the *probability current* with a classical current density, has also been employed for quantum SPR from one-dimensional wavepackets [5].

Recent works [6-9] that also approached the problem of spontaneous emission from *wide* electrons assumed a two-dimensional current *sheet* or a wide line charge. These methods, together with the Maxwell-Schrodinger analysis, interpret the electron wavefunction ψ as a smeared current density proportional to $|\psi|^2$, and underlyingly assume the spatial coherence of this single electron "current". According to this approach, when the transverse width of the current considerably exceeds the wavelength of the emitted radiation, the resulting far-field radiation must be collimated, as opposed to the point-electron case, where it is always diverging (see Fig 1a-1b).

A fundamentally different approach, also employed in the analysis of electron-light interactions [10-12] interprets the square modulus of the transverse wavefunction of a free electron $|\psi|^2$ as a probability density for finding a point electron, instead of a coherent current density. The radiation can be calculated as being emitted from a "classical" point electron, whereas the exact location of that electron should be averaged according to $|\psi|^2$. In this approach, the radiation is *always* diverging (see Fig. 1c).

Methods

To resolve this semiclassical discrepancy, we approach the problem within the quantum-electrodynamics (QED) formalism. The electron can have an arbitrarily wide transverse wavefunction (of width Δx), where we assume for simplicity that the wavefunction is paraxial with carrier momentum $\mathbf{k}_i$. The photons are quantized in the periodic Bloch modes due to the periodic grating boundary condition. Only the evanescent near-field part of each

mode carries enough momentum such that energy and momentum are conserved simultaneously, and therefore contributes to the matrix element of emission into that mode. The electron, therefore, interacts with this near-field, and subsequently emits a photon that can be detected in the far-field, having momentum $\mathbf{q}$. The setup is illustrated in Fig. 2. When the spectral radiant power $\frac{d^2P}{d\Omega d\omega}$ is calculated via the Fermi golden rule and for the wide electron case, we obtain the following general relation:

$$\frac{d^2P}{d\Omega d\omega} = \int d^2\mathbf{r}_T |\psi_T(\mathbf{r}_T)|^2 \frac{d^2P^{\text{class}}}{d\Omega d\omega}(\mathbf{r}_T)$$

where $d^2P^{\text{class}}/d\Omega d\omega$ is the emission pattern from a *point*-like electron (which is always azimuthally divergent) at the transverse position $\mathbf{r}_T$, and $\psi_T(\mathbf{r}_T)$ is the transverse part of the wavefunction. Remarkably, this relation allows us to interpret $|\psi_T(\mathbf{r}_T)|^2$ as the probability density for finding a point electron at position $\mathbf{r}_T$. The emission from different transverse positions is always summed incoherently, and therefore the emission pattern is always expected to diverge.

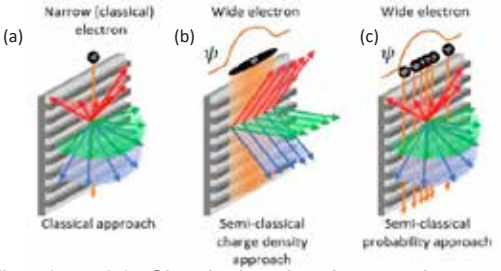

Fig. 1 – (a) Classical point-charge electron produces highly diverged radiation. (b) The current-density approach predicts collimated radiation. (c) The probability semi-classical approach predicts high divergence.

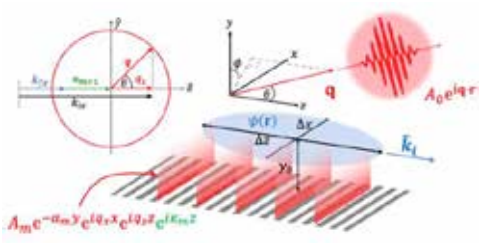

Fig. 2 –Spontaneous Smith-Purcell emission from a wide electron. Left – momentum space description for $\phi = 0$. Right – real space. The blue cloud above the grating represents the electron wave function that interacts with the periodic evanescent electromagnetic field (red), thanks to the additional momentum provided by the grating (green).

Results

To experimentally confirm our findings, we measured the azimuthal divergence of SPR in the single electron regime, using a 200 keV ($\beta = \frac{v}{c} = 0.7$) FEI Tecnai transmission electron microscope (TEM). A metallic grating of period 416 nm was placed in the viewing chamber, whereas the lenses were used to control the beam transverse dimension Δx. The narrow beam size (at the focal plane) was 300 μm. The beam size was then increased to 2000 μm by introducing astigmatism. We measured the radiation intensity using a CCD camera for different azimuthal angles (i.e., the rotation angle about the electron's velocity direction), as illustrated in Fig. 3. The results of these measurements are presented in Fig. 4. To estimate the transverse coherence length (TCL) of the electron beam at the specific working point, we measured the extent of Fresnel fringes [13,14] at the limiting aperture of the system (100 μm in diameter), to be 2.5 μm, and the used the conservation of the TCL/beam size ratio [15-17], to find that the TCL of the narrow beam was 5 μm and that of the wide beam is at least 33 μm.

Were the coherent current-density interpretation correct, then from the wide beam a very narrow azimuthal divergence $\Delta\phi = \lambda/\Delta x$ of 15 mrad (0.87 degrees) would have been observed, 30 times smaller than the measured divergence. Furthermore, a significant change in the divergence would have been obtained between the wide and narrow beams. However, the results clearly show that the divergence is broad, and that the two emission patterns of

wide and narrow beams cannot be told apart. These results clearly support the probabilistic interpretation of the electron wavefunction, which was also derived from the QED theory.

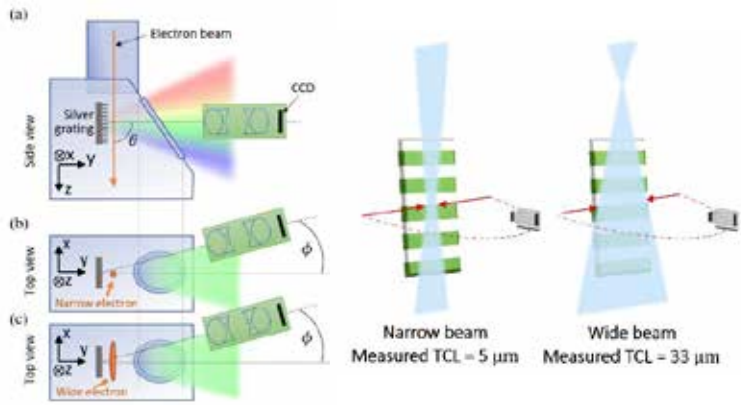

Fig. 3 – Experimental setup. (a) Side view of the viewing chamber of Transmission Electron Microscope. (b) and (c) – top view of the setup for the case of narrow (b) and wide (c) electron beam. The radiated power was measured in both cases for different values of ϕ. (d) Illustration of the narrow and wide electron beams passing parallel to the grating.

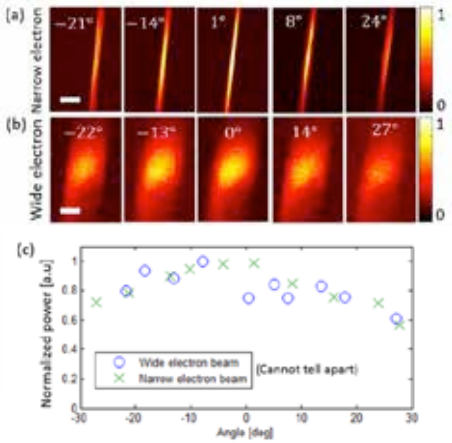

Fig. 4 – Experimental results. (a) and (b) – images of the grating plane as observed for the case of narrow and wide electron beams, respectively, for different values of the azimuthal angle ϕ. (c) – Normalized power of SPR as a function of the azimuthal angle ϕ for narrow and wide electron beams, showing no significant difference between the two.

Discussion

In conclusion, our findings suggest that the spontaneous emission from wide free electrons should be interpreted in a probabilistic, local manner – in contrast to a common approach where the wavefunction is assumed to generate a coherent current density. This conclusion can be readily generalized to processes other than SPR, and may shed light on the possible mechanisms that take part in such interactions, for example wavefunction collapse.

References

[1] S. J. Smith and E. M. Purcell, Phys. Rev. **92**, 1069–1069 (1953).
[2] J. Brownell, J. Walsh, and G. Doucas, Phys. Rev. E **57**, 1075–1080 (1998).
[3] A. Friedman, A. Gover, G. Kurizki, S. Ruschin, and A. Yariv, Rev. Mod. Phys. **60**, 471–535 (1988).
[4] N. Talebi, New J. Phys. **18**, 123006 (2016).
[5] A. Gover and Y. Pan, Phys. Lett. A **382**, 1550–1555 (2018).
[6] Z. Wang, K. Yao, M. Chen, H. Chen, and Y. Liu, Phys. Rev. Lett. **117**, 157401 (2016).
[7] L. Liang, W. Liu, Y. Liu, Q. Jia, L. Wang, and Y. Lu, Appl. Phys. Lett. **113**, 13501 (2018).
[8] C. Luo, M. Ibanescu, S. G. Johnson, and J. D. Joannopoulos, Science **299**, 368 (2003).
[9] S. Liu, M. Hu, Y. Zhang, Y. Li, and R. Zhong, Phys. Rev. E **80**, 1–10 (2009).
[10] R. H. Ritchie and A. Howie, Phil. Mag. A **58**, 753–767 (1988).
[11] B. Barwick, D. J. Flannigan, and A. H. Zewail, Nature **462**, 902–906 (2009).
[12] S. T. Park, M. Lin, and A. H. Zewail, New J. Phys. **12**, 123028 (2010).
[13] J. C. H. Spence, W. Qian, and M. P. Silverman, J. Vac. Sci. Technol. A Vacuum, Surfaces, Film. **12**, 542–547 (1994).
[14] L. Reimer and H. (Helmut) Kohl, (Springer, 2008).
[15] G. Pozzi, Optik (Stuttg). **7**, 69–73 (1987).
[16] T. Latychevskaia, Ultramicroscopy **175**, 121–129 (2017).
[17] B. Cho, T. Ichimura, R. Shimizu, and C. Oshima, Phys. Rev. Lett. **92**, 246103 (2004).

A programmable phase patterning device for electron beams

S. A. Koppell, A. J. Bowman,Y. Israel,M. A. Kasevich

Department of Applied Physics, Stanford University, Stanford, California

e-mail: skoppell@stanford.edu

In contrast to the fantastic diversity and modularity of the tools of light optics, electron optical elements are significantly constrained. A programmable phase patterning device could simulate light optics which are difficult to implement for electrons and could open up exciting possibilities like inexpensive, high order geometric aberration correction, efficient phase imaging, adaptive and compressive imaging, exotic beam shaping (e.g. bessel and vortex beams), and beam splitters for quantum electron microscopy [1].

As a step towards this goal, a 2x2 array of 1 micron Einzel lenses was recently demonstrated by Verbeeck et al [2]. As noted in their work, it will be difficult to scale this design beyond a few tens of pixels while maintaining the ability to address each pixel independently and while keeping charging and decoherence effects small.

We have designed an electron phase modulating device consisting of several thin films deposited on a silicon nitride membrane. The total thickness of the device is less than 50nm, making it nearly transparent to high energy electrons. It can also be used as a reflective element to control wavefronts produced by an electron mirror. Each micron-sized pixel on the device can be addressed in parallel to rapidly program a phase shift between 0 and 2π. Our proof of concept device has hundreds of programmable pixels, and can straightforwardly be scaled to hundreds of thousands of pixels. This talk will describe the physical mechanism and progress in characterizing the device. We will also present simulations of the device performance for applications like aberration correction and phase imaging.

References

[1] P Kruit et al, Ultramicroscopy, 164, 31-45, 2016

[2] Verbeeck et al, Ultramicroscopy, 190, 58-65, 2018

Wavefront modulation by inverted Gabor holography

T. Latychevskaia

[1]*Physics Department, University of Zurich, Winterthurerstrasse 190, 8057 Zurich*
[2]*Current address: Paul Scherrer Institute, Forschungsstrasse 111, 5232 Villigen, Switzerland*
E-mail:tatiana@physik.uzh.ch

Introduction

It is well known that by modifying the wavefront in a certain manner, the light intensity can be turned into a certain shape. Examples are optical lenses or Fresnel Zone Plates for focusing an incident wave to a point at the focal plane. Another example are Airy beams [1] created by modifying the phase distribution of the wavefront into an Airy function resulting in a bending of the light intensity while propagating. A further example is holography, where the phase of the wavefront passing through a hologram is changed to mimic the object wavefront, thus providing the illusion that the original object is present in space [2]. However, all these known techniques allow for limited light modifications: focusing within a limited region in space [2], shaping into a certain class of parametric curves [3-8] along the optical axis or bending described by a quadratic-dependent deflection as in the case of Airy beams [1]. A detailed overview of the existing light modulation methods and their limits is provided by Piestun and Shamir [9].

In the presented here work, a general case of wavefront shaping that allows for intensity and phase redistribution into an arbitrary 3D shape including pre-determined switching-off of the intensity will be presented, which is based on the co-called inverted Gabor holography [10].

Methods

In the inverted Gabor holography, to create an arbitrary 3D path of intensity, the 3D path is presented as a sequence of closely packed individual point-like absorbers and the in-line hologram of the warfront propagated through the 3D path of absorbers is simulated. When such a hologram is contrast inverted, a so-called "diffractor" is obtained. Under illumination of the diffractor, the pre-determined three-dimensional path is reconstructed behind the diffractor as a bright path of intensity. The crucial parameter for a smooth optical path is the sampling of the predetermined 3D curve, which is given by the lateral and axial resolution of the optical system.

Results

To demonstrated the 3D wavefront modulation using the principle of the inverted Gabor holography, we performed light optical experiments. The results are shown in Fig. 1. The light intensity was modulated into a form of a straight beam splitting into two parallel beams. The simulated diffractor is shown in Fig. 1(a) and the pre-defined path is shown in Fig. 1(b). In the simulations presented here, the 3D path was sampled at planes *z* = 100 – 900 mm using steps of 4 mm. When numerically reconstructed, the intensity distribution is matching the distribution of the initial path. The experimentally measured light distribution reproduces the predefined split shape, see Fig. 1(b). The (x,z)-plane distributions shown in Fig. 1(c) also show good agreement between the numerically reconstructed and experimentally observed intensity distributions. The (x,y)-plane distributions at three different distances are shown in Fig. 1(d).

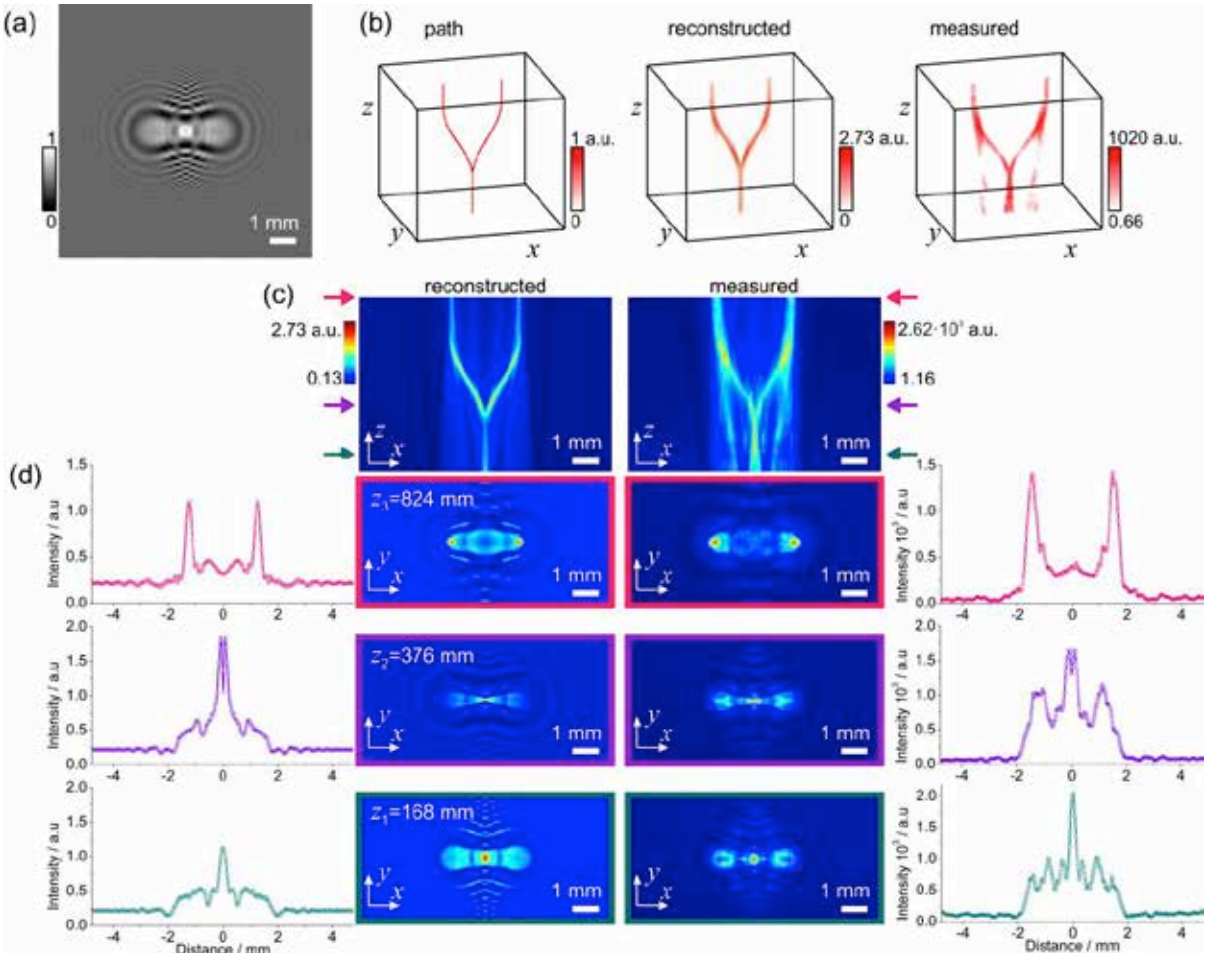

Figure 1. Shaping a split light beam. (a) Central part of 300 × 300 pixels corresponding to 9.6 mm × 9.6 mm of the simulated diffractor. (b) Three-dimensional representation of the light intensity: the desired intensity path used for simulating the diffractor (left), the numerically reconstructed intensity distribution by field propagation behind the diffractor (center), and the experimentally measured intensity distribution behind the diffractor (right). (c)

Two-dimensional intensity distributions $I(x, y=0, z)$ numerically reconstructed behind the diffractor (left) and the experimentally measured intensity (right). (d) Intensity distributions at three different *z*-positions: z_1 = 168 nm, z_2 = 376 nm and z_3 = 824 nm indicated with colored arrows in (c). Two-dimensional $I(x, y, z_i)$ at fixed z_i -positions intensity distributions obtained by numerical reconstruction (second column) and measured experimentally (third column) behind the diffractor. The related one-dimensional intensity distributions $I(x, y=0, z_i)$ at the corresponding z_i -positions are shown in the first and in the fourth column.

Discussion

This technique of 3D wavefront modulation can be applied to any waves, for example, electron, X-ray waves or terahertz waves provided the diffractor could be scaled down to the nanometer size. We will discuss the resolution limits of the method and possible applications.

References

[1] M. V. Berry, and N. L. Balazs, "Nonspreading wave packets," Am. J. Phys. **47**, 264–267 (1979).
[2] D. Gabor, "A new microscopic principle," Nature **161**, 777–778 (1948).
[3] C. A. Alonzo, P. J. Rodrigo, and J. Gluckstad, "Helico-conical optical beams: a product of helical and conical phase fronts," Opt. Express **13**, 1749–1760 (2005).
[4] V. Jarutis *et al.*, "Spiraling zero-order Bessel beam," Opt. Lett. **34**, 2129–2131 (2009).
[5] J. E. Morris *et al.*, "Realization of curved Bessel beams: propagation around obstructions," J. Opt. **12**, 124002 (2010).
[6] I. D. Chremmos *et al.*, "Bessel-like optical beams with arbitrary trajectories," Opt. Lett. **37**, 5003-5005 (2012).
[7] J. Y. Zhao *et al.*, "Observation of self-accelerating Bessel-like optical beams along arbitrary trajectories," Opt. Lett. **38**, 498–500 (2013).
[8] J. A. Rodrigo *et al.*, "Shaping of light beams along curves in three dimensions," Opt. Express **21**, 20544–20555 (2013).
[9] R. Piestun, and J. Shamir, "Synthesis of three-dimensional light fields and applications," Proc. IEEE **90**, 222–244 (2002).
[10] T. Latychevskaia, and H.-W. Fink, "Inverted Gabor holography principle for tailoring arbitrary shaped three-dimensional beams " Sci. Rep. **6**, 26312 (2016).

Design and implementation of a tunable phase plate for electron microscopy based on Ampere's law

P.-H. Lu[1], M. Beleggia[2], A. Roncaglia[3], R. Speen[1], U. Poppe[1], M. Kruth[1], H. Soltner[1], A. H. Tavabi[1], G. Pozzi[1,4] and R. E. Dunin-Borkowski[1]

[1]Forschungszentrum Jülich, Jülich, Germany
[2]Technical University of Denmark, Lyngby, Denmark
[3]National Research Council of Italy, Modena, Italy
[4]University of Bologna, Bologna, Italy
E-mail: p.lu@fz-juelich.de

Approximately 70 years ago, Boersch proposed several devices that could produce a desired phase shift between a direct beam and scattered electrons to enhance phase contrast [1]. One of these devices, which later became known as a Zernike phase plate (PP), makes use of a thin film to introduce a phase shift to scattered electrons, while the direct beam passes through a central hole without undergoing a phase change. As they are charged particles, electrons can also be manipulated using external electromagnetic fields. This is the principle of other arrangements that Boersch proposed [1] and has led to a number of conceptually new PP designs [2]. However, most of these designs suffer from unwanted electrostatic charging, even when self-charging is used to produce the phase shift, e.g., in a Volta PP [3]. The imparted phase shift may then deviate from the optimal value and the lifetime of the device is usually limited. In order to address most of these issues, we introduce a tunable PP design based on Ampere's law and thus refer to the device as "tunable Ampere phase plate" (TAPP) [4]. The magnetic field circulating around a vertical segment of current-carrying wire could impart a position-dependent and rapidly decreasing phase shift to the incident electrons, which shifts the phase of the unscattered electrons in the vicinity of the vertical current, while the scattered electrons are barely influenced. The design, implementation and experimental tests of this device will be presented [5].

References

[1] H. Boersch, Zeitschrift fur Naturforschung - Section A Journal of Physical Sciences **2**, 615 (1947).
[2] R. M. Glaeser, Review of Scientific Instruments **84**, 111101 (2013).
[3] R. Danev, B. Buijsse, M. Khoshouei et al. PNAS **111**, 15635 (2014).
[4] A. H. Tavabi, M. Beleggia, V. Migunov et al. Scientific Reports **8**, 5592 (2018).
[5] The authors acknowledge a Deutsch-Israelische Projektkooperation grant from the Deutsche Forschungsgemeinschaft and funding from the European Research Council under grant agreement No. 766970.

Quantum correlations in electron microscopy

C. Mechel[1], Y. Kurman[1], A. Karnieli[2], N. Rivera[3], A. Arie[2] and I. Kaminer[1]

[1]Technion – Israel Institute of Technology, Haifa, Israel

[2]Tel Aviv University, Tel Aviv, Israel

[3]Massachussetts Institute of Technology, Cambridge, MA, USA

E-mail: cmechel@campus.technion.ac.il

Introduction

Electron microscopes provide a powerful platform to study quantum phenomena with the precision of a free electron probe [1]. Techniques such as electron energy loss spectroscopy (EELS) reveal materials' optical excitations, such as surface and bulk plasmons. These excitations can be stimulated by laser pulses in photon-induced near-field electron microscopy, achieving femtosecond temporal and nanometer spatial resolution [2]. Such novel techniques give further motivation to study basic questions about quantum correlations between the electron and the optical excitations. Can we use the tools of quantum information to shed new light on the quantum correlations and utilize their underlying physics to develop new spectroscopic functionalities?

Here, we study the interaction of free electrons with general optical excitations in matter, with focus on the quantum correlations created during the interaction. We connect the electron spatial coherence and the electron-polariton entanglement created during the interaction to the electromagnetic Green's function of the medium, and propose applications for measuring the dispersion and lifetime of surface plasmon polaritons (SPPs). Our findings could enrich the analytical capabilities of electron microscopes, and lay the groundwork for using electron microscopes to explore the underlying quantum information aspects intrinsic to electron-excitation interaction.

Methods

Consider an electron passing through a sample that supports localized optical excitaitons, such as dipolar resonances in nanoparticles, or extended excitations, such as surface plasmons on metalic surfaces. The electron excites a quantized polaritonic excitation and its resulting energy loss is probed by EELS. The electron and the excitations can be described by the joint wavefunction: $\sum_\sigma c_\sigma \, |\psi_\sigma\rangle_{\mathrm{electron}} |1_\sigma\rangle_{polariton}$, which displays entanglement between the electron and the polariton modes. Using EELS, we post-select the electrons that lost energy in creating an excitation of a specific energy, thus allowing us to indirectly resolve the excitation. These serve as knobs for controlling the entanglement in the interaction.

Our formalism describes the interaction of a free electron with excitations in a general optical environment, including losses, for which we use the framework of macroscopic QED [4]. We solve for the joint final state of the electron and the excitations and then trace-out the excitations to obtain the reduced density matrix of the electron, which is the only party being measured in the experiment. Due to the entanglement between the electron and the excitations, the measured electron is generally mixed and consequently its spatial coherence is impaired. Using our

formalism, we quantitatively address the intriguing relation between the post-interaction electron spatial coherence and the entanglement created in the interaction.

Results

We find the connection between the electron reduced density matrix with the dyadic electromagnetic Green's function of the optical environment:

$$\rho_{\mathrm{e}}(\boldsymbol{r}_\perp,\boldsymbol{r}'_\perp;\Delta E)=\frac{\alpha}{\pi^2}\frac{1}{\hbar cA}\int dz\,dz'\,e^{i\frac{\Delta E}{\hbar v_0}(z-z')}\mathrm{Im}\mathbf{G}_{zz}\left(\mathbf{r}_\perp,z;\,\mathbf{r}'_\perp,z';\,\frac{\Delta E}{\hbar}\right), \tag{1}$$

where α is the fine-structure constant, v_0 is the initial electron velocity, c is the speed of light, A is a sample area, $\hbar$ is the reduced Planck's constant, and $\mathrm{Im}G_{zz}\,(\boldsymbol{r}_\perp,z;\,\boldsymbol{r}'_\perp,z';\frac{\Delta E}{\hbar})$ is the imaginary part of the zz-component of the dyadic Green's function with frequency $\frac{\Delta E}{\hbar}$. The diagonal part of Eq. (1) corresponds to the classical observables in EELS [1], the energy-filtered transmission electron image. The off-diagonal elements are related to the electron spatial coherence [3]. Therefore, Eq. (1) relates the excitation's electromagnetic classical correlations to the electron's quantum correlations. To quantify the electron-polariton entanglement, we calculate the electron purity [3], which is 1 for no entanglement (the electron is pure) and 0 for maximal entanglement (the electron is completely mixed).

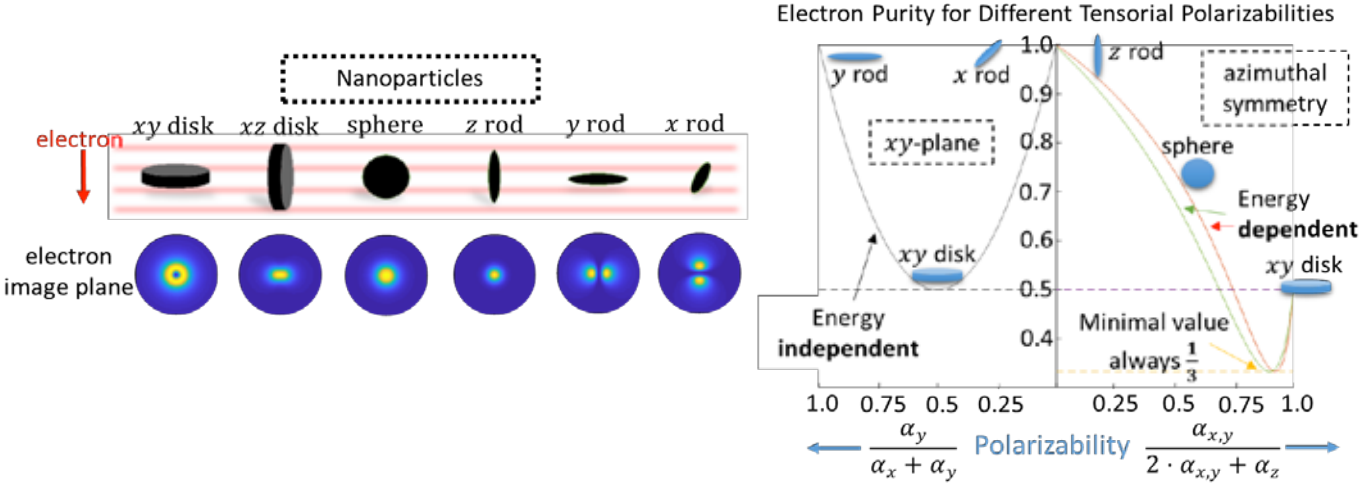

Figure 1: **Quantum correlations between a free electron and a nanoparticle. (a)** Energy-filtered electron image $\langle \boldsymbol{r}_\perp|\rho|\boldsymbol{r}_\perp\rangle$ after interacting with different nanoparticle shapes. Different dipole orientations induce different electron images, allowing us to measure the polarizability $\bar{\bar{\boldsymbol{\alpha}}}(\omega)$, from which we can calculate the electron coherence. **(b)** The electron purity for different nanoparticle geometries, demonstrating our "discrete" control over the entanglement in the interaction, by shaping the nanoparticle geometry. The minimal value of the purity is always $\frac{1}{3}$, inverse the number of non-zero eigenvalues of ρ. The electron is more coherent (larger purity) when interacting with lower-dimensional shapes, such as disks or rods.

To demonstrate our formalism, we consider the electron interaction with various nanoparticles (Fig. 1(a)). We treat the nanoparticle as a point dipole with tensorial polarizability $\bar{\bar{\boldsymbol{\alpha}}}$ (3-by-3 matrix), implying that at most 3 dipole modes can be excited per energy (corresponding to x-,y-,z- dipoles, up to rotations). Because of the quantum correlations with the nanoparticle, the electron state is comprised of at most 3 contributions, each summed-up incoherently, which reduces the electron spatial coherence. From this analysis, we deduce the connection between

the geometry of the nanoparticle to the electron decoherence, as depicted in Fig. 1(b), which shows that decreasing the number of excitation modes improves electron coherence.

In addition to our analysis of nanoparticles that deals with a finite number of modes, the electron can become entangled to a continuum of modes in any optical environments, as we exemplify with the case SPPs. In this case, the post-interaction electron spatial coherence is greatly affected by the plasmonic losses, as was measured and analysed before by several groups (e.g., see papers by Lichte, van Dyck, Verbeeck, and others [5]). Our quantum-informational analysis further predicts that unlike the electron spatial coherence that depends on the plasmonic decay, the electron-plasmon entanglement (quantified as before with the electron purity) does not depend on the decay. Thus, the electron experiences a similar degree of decoherence, regardless of the plasmonic losses. We use macroscopic QED [4] to quantitatively infer the decoherence in the interaction, and propose its applicability for measuring SPPs dispersion and lifetime for each frequency, using electron energy-filtered diffraction (see Fig. 2).

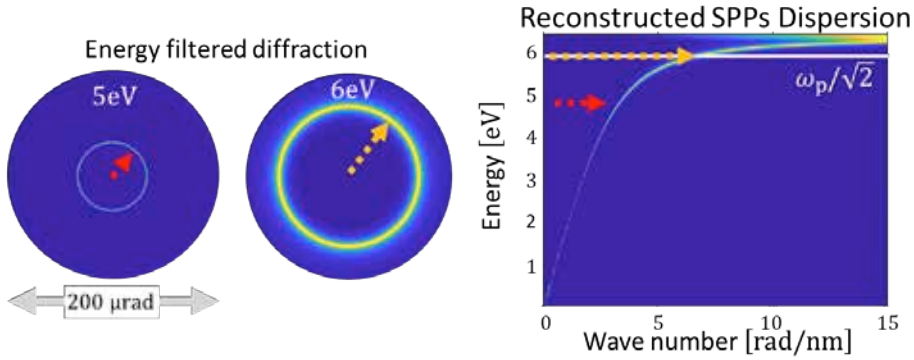

Figure 2: **Finding the disperion and lifetime of SPPs from their entanglement to free electron probes. (a)** Energy-filtered electron diffraction images. The ring radius of each image is determined by the momentum of the plasmon with the matching energy, and the ring width yields the plasmon propagation distance. **(b)** Reconstructed plasmonic dispersion using simulated diffraction images, showing a good match with theory.

To conclude, we study the interaction of free electrons with general optical excitations, exemplified with nanoparticles and with SPPs. We find a connection between the electron density matrix and its entanglement to the excitations using the macroscopic QED tools. We quantify the electron spatial coherence and the entanglement induced in the interaction, and utilize this connection to show how to measure the dispersion and lifetime of SPPs at each frequency by a corresponding energy-filtered electron diffraction image.

References

[1] J. Abajo, Reviews of modern physics **82**, 209 (2010)

[2] A. Zewail, Science **328**, 187 (2010); A. Feist *et al.*, Nature **521**, 200 (2015); G. Vanacore *et al.*, accepted to Nat. Matetrials, arXiv 1806.00366

[3] M. Nielsen and I. Chuang, Cambridge University press, New York, NY, USA (2011)

[4] S. Scheel *et al.*, Acta Physica Slovaca **58**, 675 (2008)

[5] J. Verbeeck, *et al.*, Ultramicroscopy **102**, 229 (2005); **111**, 887 (2011); P. Potapov *et al.*, Ultramicroscopy **106**, 1012 (2006); **107**, 559 (2007)

Towards direct imaging of GHz magnetic dynamics with sub-100-nm resolution in a transmission electron microscope

Y. Murooka[1], T. Weßels[1], R. Speen[2], V. Migunov[2, 3], U. Poppe[4], H. Soltner[5], B. Breitkreutz[6], A. Kovács[2] and R. E. Dunin-Borkowski[1, 2]

[1] Forschungszentrum Jülich, Peter Grünberg Institute, Jülich, Germany
[2] Forschungszentrum Jülich, Ernst Ruska-Centre for Microscopy and Spectroscopy with Electrons, Jülich, Germany
[3] RWTH Aachen University, Central Facility for Electron Microscopy (GFE), Aachen, Germany
[4] CEOS GmbH, Heidelberg, Germany
[5] Forschungszentrum Jülich, Central Institute of Engineering, Electronics and Analytics, Jülich, Germany
[6] Forschungszentrum Jülich, Nuclear Physics Institute (IKP-4), Jülich, Germany
E-mail: y.murooka@fz-juelich.de

Modern spin-based technology has been rapidly advanced by making use of microscopic magnetic processes, such as the generation of spin waves in nanoscale geometries. Subtle differences in nanostructure can result in significant changes in magnetic properties due to the competing energies. Conventionally, direct magnetic imaging is achieved in real space by using quantitative transmission electron microscopy (TEM) methods such as off-axis electron holography and Lorentz microscopy. However, the dynamics of spin waves that are far from equilibrium are often of interest, with excitation frequencies taking values that can exceed 10 GHz. At present, there is no standard technique that can be used to investigate such a time domain with nm spatial resolution. Here, we report a GHz TEM technique that allows the application of in-plane radio frequency (RF) magnetic fields to a sample between the MHz range and 15 GHz, in order to excite spin waves such as magnons. The RF signal is guided to the specimen by a coplanar waveguide, which is patterned on an exchangeable Si chip. The geometry of the guide is optimised using magnetic field simulation. Results obtained from magnetic specimens that are patterned into nanodisks, nanoparticles and nanowires will be presented.

The Classical-to-Quantum Transition of Measurements from Linear Particle Accelerators to Photon-induced Near-field Electron Microscopy

Yiming Pan[1†], Eliahu Cohen[2†], Ebrahim Karimi[3], Avraham Gover[4], Ido Kaminer[5] and Yakir Aharonov[6,7]

[1]Department of Physics of Complex Systems, Weizmann Institute of Science, Rehovot 7610001, Israel
[2]Faculty of Engineering and the Institute of Nanotechnology and Advanced Materials, Bar Ilan University, Ramat Gan 5290002, Israel
[3]Department of Physics, University of Ottawa, Ottawa, Ontario, K1N 6N5, Canada
[4]Department of Electrical Engineering Physical Electronics, Tel Aviv University, Ramat Aviv 6997801, ISRAEL
[5]Department of Electrical Engineering, Technion: Israel Institute of Technology, Haifa 3200003, Israel
[6]School of Physics and Astronomy, Tel Aviv University, Ramat Aviv 6997801, Israel
[7]Institute for Quantum Studies, Chapman University, Orange, CA 92866, USA
Correspondence to Y.P. (yiming.pan@weizmann.ac.il).

Introduction

Measurement lies at the heart of quantum mechanics. It allows us to probe the system of interest through a measuring pointer coupled to its observables. The quantum interaction between the measured system and measurement (classical) apparatus is later amplified for the outcome to be seen macroscopically. There is, however, a continuous transition between classical and quantum interactions, which we would like to analyze when examining several limiting cases of the measurement process in the context of light-matter interactions.

What is the role of wave-particle duality in quantum interactions between light and matter? Here we explore the classical-to-quantum transition associated with measurements in light-matter interactions, as shown in Fig.1. Four couplings in the inverse Smith-Purcell setup on a grating were considered, loosely corresponding to 'classical electron' and 'classical photon', 'classical electron' and 'quantum photon', 'quantum electron' and 'classical photon', and 'quantum electron' and 'quantum photon'. Based on the wavepacket representation of free electrons, we find a universal factor $\exp\left(-\Gamma^2/2\right)$ in the physics of wavepacket acceleration, characterizing the transition of measurements from classical to quantum, in which $\Gamma = 2\pi\Delta_z/\beta\lambda$ is the ratio between the electron wavepacket size Δ_z and the optical wavelength λ with β being the electron's velocity divided by the speed of light in vacuum.

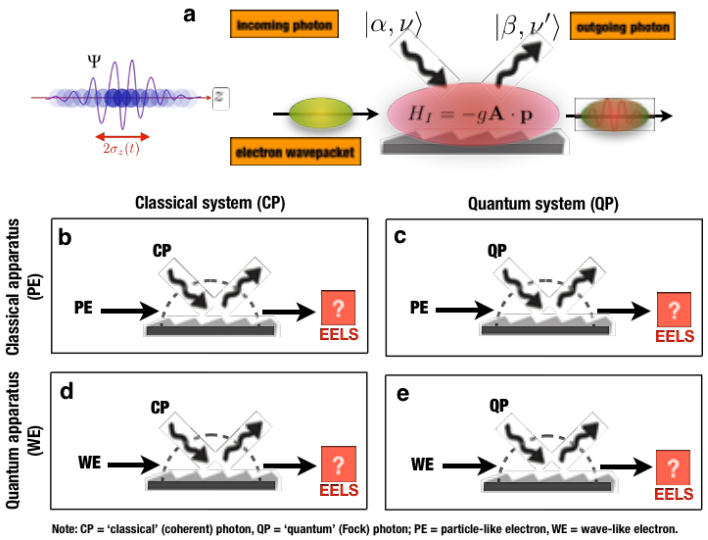

Fig. 1 The classical-to-quantum measurement schemes of the electron-photon interaction. Four combinations of electron and photon interactions in the classical-to-quantum measurement transition. The readout is the electron energy loss spectrum (EELS).

In the point-particle limit ($\Gamma \to 0$), the appearance of classical linear particle accelerator is shown to be a result of the weak measurement scheme; meanwhile, the Photon-Induced Near-field Electron Microscopy (PINEM) naturally corresponds to von Neumann's measurement scheme in the plane-wave limit ($\Gamma \to \infty$). Our classical-to-quantum measurement theory may more generally delineate the border between the realms of classical and quantum electrodynamics, employing the very essence of wave-particle duality in the quantum measurement process.

Methods

With the short duration approximation $\dot{z} \simeq v_0$, $z(t) = v_0 t$, the classical momentum transfer can be thus reduced to

$$\Delta p_{point} \simeq -eE_c \int_0^{L/v_0} \cos\left(\omega t - q_z(v_0 t) + \phi_0\right) dt = -\left(\frac{eE_c L}{v_0}\right) \mathrm{sinc}\left(\frac{\bar{\theta}}{2}\right) \cos\left(\frac{\bar{\theta}}{2} + \phi_0\right), \qquad (1)$$

where the synchronization condition is $\bar{\theta} = \left(\omega / v_0 - q_z\right) L$, where L is the interaction length and v_0 is the initial velocity of the electron. This is the well-known linear acceleration formula in classical accelerator physics, as well as in Free Electron Lasers (FEL) and the inverse Smith-Purcell effect, which in principle leads us to laser-induced particle accelerator on a chirp. In our QED treatment of the initial electron-photon state as given by $c_{p,\nu}^{(0)} = c_p^{(0)} c_\nu^{(0)}$, we consider the initial electron wavepacket of the chirped Gaussian distribution combined with a coherent photon state ($\left|\sqrt{\nu_0}\right\rangle$). From the treatment of quantum electrodynamics, one can obtain the explicit energy transfer of electron pointer with two parts:

$$\begin{aligned} \Delta E^{(1)} &= -\left(eE_c L\right) e^{-\Gamma^2/2} \mathrm{sinc}\left(\frac{\bar{\theta}}{2}\right) \cos\left(\frac{\bar{\theta}}{2} + \phi_0\right) \\ \Delta E^{(2)} &= -\tilde{\Upsilon}^2 \hbar\omega \, \mathrm{sinc}^2\left(\frac{\bar{\theta}}{2}\right), \end{aligned} \qquad (2)$$

where the normalized photon exchange coefficient is defined as $\tilde{\Upsilon} = e\tilde{E}_q L / 4\hbar\omega$. A surprising extinction parameter in the phase dependent energy transfer (6), is given by $\Gamma = \left(\frac{\omega}{v_0}\right) \Delta_z\left(t_D\right) = \left(\frac{\hbar\omega}{v_0}\right) \frac{\sqrt{1+\xi^2 t_D^2}}{2\Delta_{p_0}} = \Gamma_0 \sqrt{1+\xi^2 t_D^2}$, with $\Gamma_0 = \frac{2\pi}{\beta}\left(\frac{\Delta_{z_0}}{\lambda}\right)$. The decay factor ($e^{-\Gamma^2/2}$) demonstrates that the prior history and the wavepacket size and form of a free electron have physical effects in its interaction with coherent light.

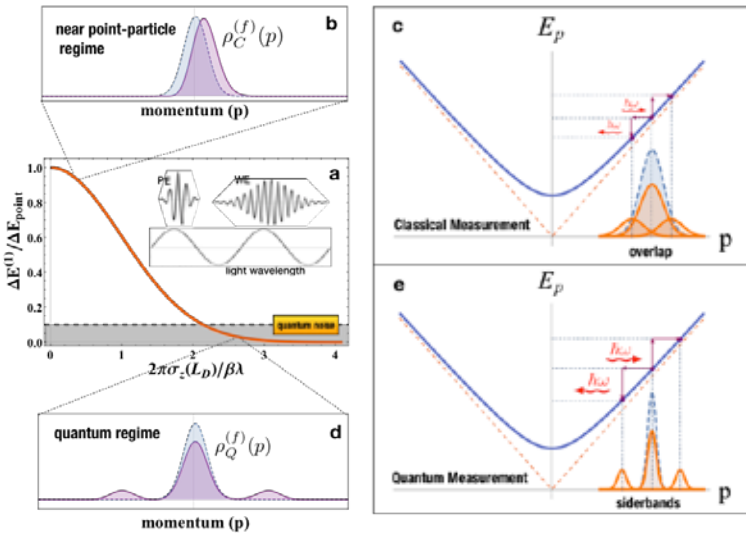

Fig. 2 The classical-to-quantum measurement transition between the classical point-particle picture (b, c) and quantum plane-wave picture (d, e) of electron wavepacket pointer when coupled to a photon coherent state.

Results and Discussion

The particle-to-wave transition of the electron-photon interaction in measuring electron energy loss spectroscopy (EELS) is shown in Fig. 2. The decay parameter (Γ) implies the measurability of the electron wavepacket size near the classical particle-like regimes. On the other hand, the plane-wave limit can be directly defined in the case $\Delta E^{(1)} \to 0$ and only has the contribution of phase-independent terms. Additionally, the phase-independent term ($\Delta \mathrm{E}^{(2)}$) relates to the vacuum expectation value, which acts as quantum noise of spontaneous fluctuation in our electron-photon coupling measurements.

<u>Is the point-particle acceleration possibly a weak-value of vector potential</u>? – As demonstrated in Fig. 2b&d, we find that the strong measurement [5] corresponds to the electron spectrum with discrete photon-sidebands, and the weak measurement [8] to the accelerated spectrum with central momentum shift. Note that our classical-to-quantum measurement theory is completely different from the environment-induced decoherence program. After applying decoherence theory whose 'classicality' emerges from the natural loss of quantum interference by 'leakage' into the environment, in fact, we would expect the final electron state without contributions of quantum interference to yield neither wavepacket-dependent acceleration nor periodic density bunching in the attosecond scale, which indicates that the environment-induced decoherence cannot produce the classical linear particle accelerator.

References

[1]. Gover, A. and Pan, Y. Phys. Lett. A 382, 1550-1555 (2018).

[2]. Barwick, B., Flannigan, D. J., & Zewail, A. H. Nature 462, 902-906 (2009).

[3]. Feist, A., Echternkamp, K. E., Schauss, J., Yalunin, S. V., Schfer, S. & Ropers, C. Nature 521, 200-203(2015).

[4]. Peralta, E. A., Soong, K., England, R. J., Colby, E. R., Wu, Z., Montazeri, B., & Sozer, E. B. Nature 503, 91-94 (2013).

[5]. Von Neumann, J. Mathematical foundations of quantum mechanics: New edition. Princeton university press (2018).

[6]. Aharonov, Y., Albert, D. Z., & Vaidman, L. Phys. Rev. Lett. 60, 1351 (1988).

[7]. Aharonov Y, Cohen E, Carmi A, Elitzur A. C. Proc. R. Soc. A 474, 20180030 (2018).

[8]. Schlosshauer, M. arXiv preprint arXiv:1404.2635 (2014).

The role of spatial coherence for the creation of and imaging with atom size electron vortex beams

Darius Pohl[1,2], Stefan Löffler[4], Sebastian Schneider[2,3], Peter Tiemeijer[5], Sorin Lazar[5], Kornelius Nielsch[2], and Bernd Rellinghaus[1,2]

[1]Dresden Center for Nanoanalysis, TU Dresden, D-01062 Dresden, Germany.
[2]IFW Dresden, P.O. Box 270116, D-01171 Dresden, Germany.
[3]Institute for Solid State Physics, TU Dresden, D-01062 Dresden, Germany.
[4]University Service Centre for Transmission Electron Microscopy, TU Wien, 1040 Wien, Austria.
[5]Thermo Fisher Scientific, PO Box 8066, 5600 KA Eindhoven, The Netherlands.
E-mail: darius.pohl@tu-dresden.de

Introduction

Recently discovered electron vortex beams, which carry quantized orbital angular momenta (OAM) L, promise to reveal magnetic signals [1]. Since electron beams can be easily focused down to sub-nanometer diameters, this novel technique promises the possibility to quantitatively determine local magnetic properties with unrivalled lateral resolution. To generate the spiralling wave front of an electron vortex beam with an azimuthally growing phase shift of up to 2π and a phase singularity in its axial centre, specially designed apertures are needed [2].

Methods

In order to produce single electron vortex beams, we recently developed a method which allows to generate user-defined OAM beams [3]. We implemented two types of apertures, a 50 µm fork-type aperture and a 100 nm small blocking aperture into the condenser lens system of a FEI Titan3 80-300 transmission electron microscope (TEM) equipped with a probe spherical aberration corrector and a Wien-type monochromator. The selected focused probe is used for the acquisition of HRSTEM images and local EELS maps. Although today, atom size electron vortex beams can be readily generated and atomically resolved HRSTEM and EELS data can be acquired with OAM-selected EVBs, the application as a probe for local measurements of the electron energy loss magnetic chiral dichroism (EMCD) suffers from a poor S/N ratio and is thus still under development. One reason may be the incoherence of the vortex beam itself, which results in a strong reduction of the dichroic signal. Measurements on ferrimagnetic samples reveal magnetic signals, which are by far smaller than expected from simulations.

Results

Both electron guns show an improvement of the spatial coherence with increasing gun lens excitation, measured by the central intensity dip in the |L| = 1 ħ vortex beam. For the XFEG operated at 200kV, a central intensity dip of LDip/Imax = 0.3 can be reached. HR-STEM imaging of the Barium hexaferrite $BaFe_{11}TiO_{19}$ is shown in Fig.2 using the L=+1 vortex beam (200kV, XFEG). The improved coherence is found to result in an enhanced visibility of the donut-like intensity distribution in the intensity of the atomic columns. Adding additional phase shifts to the electron probe, e.g. by 2-fold astigmatism results in a splitting of the ring intensity into two side-lobes, which is directly visible in the HR-STEM image (see fig. 2).

Discussion

EVBs generated from fully coherent primary beams may be the missing piece to the puzzle of substantially improving quantitative magnetic signals as obtained from individual atomic columns. Additionally, using aberrations to modify the electron vortex beam might be useful for advanced orbital or plasmon mapping.

References

[1] J. Verbeeck et al., Nature **467** (2010), p. 301-304.
[2] J. Verbeeck et al., Ultramicroscopy **113** (2012), p. 83-87.
[3] D. Pohl et al., Sci. Rep. **7** (2017) 934.
[4] P. Schattschneider et al., Ultramicroscopy **111** (2011), p. 1461-1468.
[5] P. Schattschneider et al., Ultramicroscopy **115** (2012), p. 21-25.

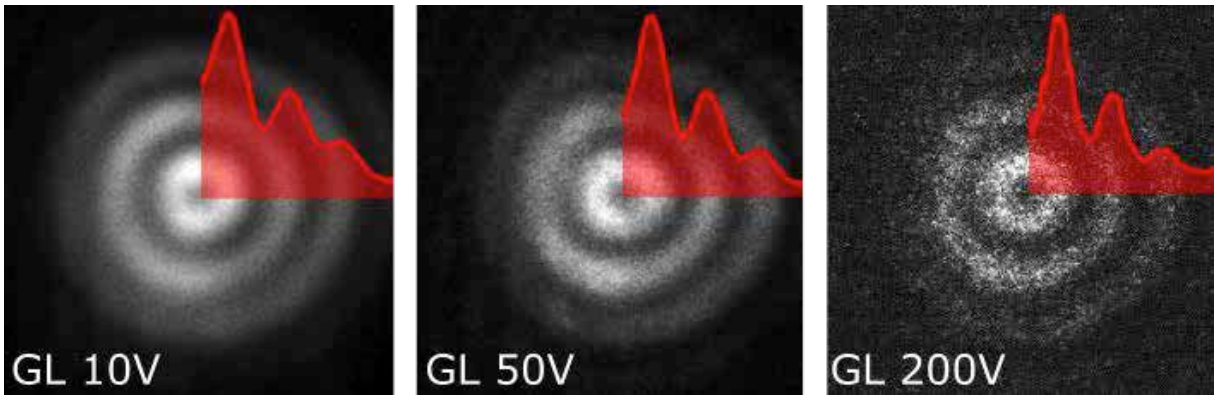

Figure 1: Images of the electron vortex beam for different gun lens excitations using a XFEG @ 200kV. An exposure time of 0.5 s was used for all images. Insets show normalized and rotationally averaged intensity profiles.

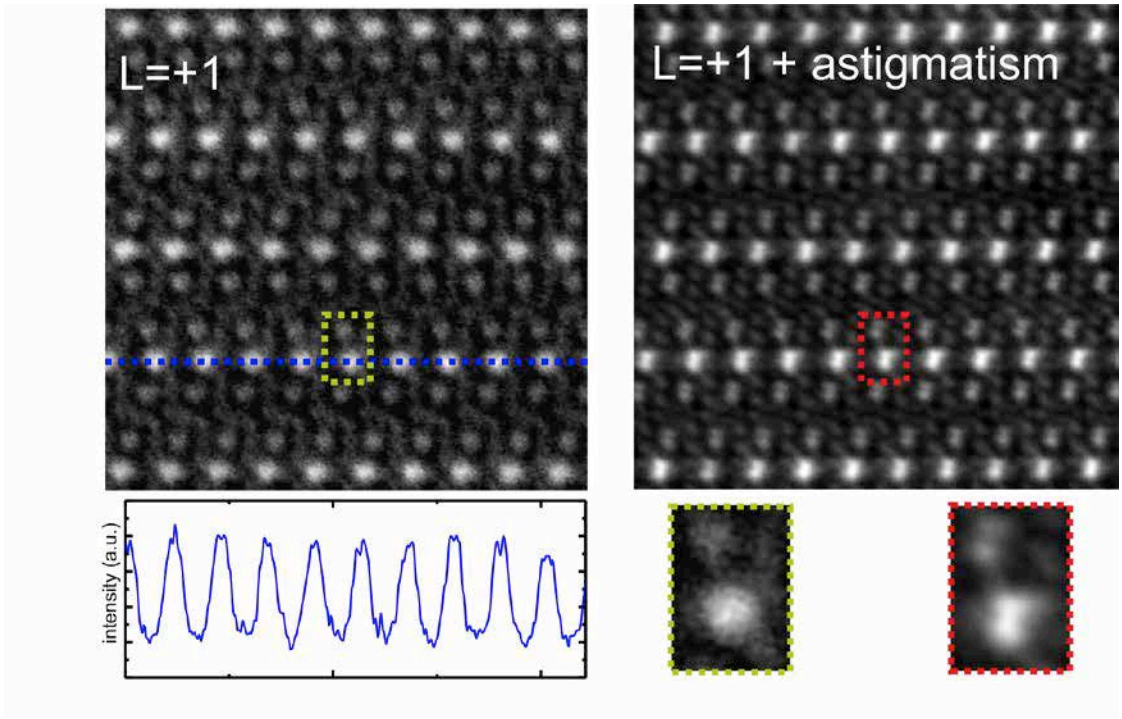

Figure 2. HR-STEM image of BaFe11TiO19 acquired in a [100] zone axis orientation using electron vortex beams with L=+1 with and without 2-fold astigmatism. The donut-like intensity distribution in the images of individual atomic columns can be seen from dips in the intensity profile across a single row of Ba atoms (see blue line across the top left HR-STEM image and bottom left profile). The effect becomes even more evident from the occurrence of a splitting of the otherwise centro-symmetric intensity distributions of all columns into two separate arcs upon introducing some two-fold astigmatism to the beam. All pairs of arcs oppose one another exactly along the two-fold axis of astigmatism (see top right HR-STEM image and magnified sections of the stigmatic and astigmatic images, respectively (bottom right).

Time-, and phase-resolved cathodoluminescence spectroscopy

Magda Sola Garcia,[1] Nick Schilder,[1] Sophie Meuret,[1,*] Toon Coenen,[1,2] and Albert Polman[1]

[1]Center for Nanophotonics, AMOLF, Amsterdam, the Netherlands
[2]Delmic, Kanaalweg 4, Delft, the Netherlands
polman@amolf.nl

Abstract
We present time-resolved pump-probe and phase-resolved cathodoluminescence spectroscopy using two new SEM-CL microscopes that we have recently constructed.[1]

Pump-probe CL spectroscopy
We present ultrafast pump-probe cathodoluminescence spectroscopy to investigate the dynamics of electron-induced $NV^0 \leftrightarrow NV^-$ state transfer of diamond NV centers. We use 1-ps 5-keV electron pulses created by photoemission using 250-fs λ=258 nm laser pulses for excitation, and use λ=517 nm laser pulses to read out the NV states. The electron-induced carriers induces the conversion from NV^- to NV^0 and the data is explained with a 3D carrier diffusion and excitation model considering carrier recombination (0.8 ns), NV^0 spontaneous emission (20 ns) and $NV^0 \rightarrow NV^-$ back transfer (500 ms). The results provide new insights into the $NV^- \leftrightarrow NV^0$ conversion dynamics, and into the use of picosecond pump-probe cathodoluminescence as a nanoscale characterization tool of optical excitation processes.

Phase-resolved CL microscopy
While CL signals can now be resolved in the spatial, spectral, angle, polarisation and time domain,[2,3,4] measurements of the CL emission wave fronts, which are relevant in coherent CL excitation spectroscopy, have been elusive so far. We present the 30 keV angle-resolved CL emission patterns from a single Ag plasmonic nanoscatterer that is excited through surface plasmon polaritons on Ag, that we interfere in the far field with a CL transition radiation reference signal. We observe pronounced angle- and wavelength-resolved interference fringes from which we derive the CL nanoscatterer's wave front over a broad angular range. The data also provide a direct map of the dispersion relation of surface plasmon polaritons on Ag.

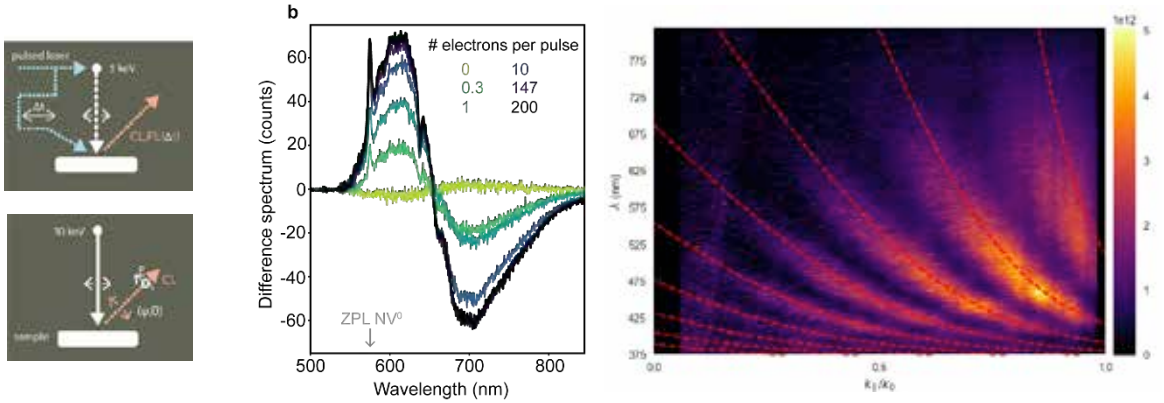

Figure 1 (left) Schematics of pump-probe CL (top) and angle and polarization-resolved CL (bottom). (center) Difference spectra of combined CL+PL excitation and separate CL and PL excitation, showing increased NV^0 and decreased NV^- contributions upon increased number of electrons per pulse. (right) CL intensity due to single-particle plasmon and transition radiation interference, as a function of in-plane wave vector. Dashed lines correspond to calculations taking into account the SPP dispersion relation.

References

[1] S. Meuret, M. Solà Garcia, T. Coenen, E. Kieft, H. Zeijlemaker, M. Lätzel, S. Christiansen, S.Y. Woo, Y.H. Ra, Z. Mi, and A. Polman, Ultramicroscopy **197**, 28 (2019)
[2] S. Peng, N. Schilder, X. Ni, J. van de Groep, A. Alú, A. Khanikaev, H.A. Atwater, and A. Polman, Phys. Rev. Let. **122**, 117401 (2019)
[3] J. Schefold, S. Meuret, N. Schilder, H. Agrawal, E. Garnett, and A. Polman, ACS Photon. **6**, 1067 (2019)
[4] T. Coenen and A. Polman, ACS Photon. **6**, 573 (2019)

* present address: CNRS, Center d'Élaboration de Matériaux et d'Etudes Structurale (CEMES), Toulouse, France

Realization of a holographic Fan Out e-beam OAM sorter

Paolo Rosi [1], Federico Venturi [1], Giacomo Medici [1], Claudia Menozzi[1], Gian Carlo Gazzadi[2],Enzo Rotunno[2], Stefano Frabboni [1,2], Robert Nijland[4], Peter Tiemeijer[4] ,Amir Hossein Tavabi[3], Rafal Dunin-Borkowski[3] and Vincenzo Grillo [2]

[1]Università di Modena e Reggio Emilia, Dipartimento FIM, Modena, Italy
[2] CNR Ististuto Nanoscienze S3 , Modena, Italy
[3] Ernst-Ruska Center, Forschungszentrum Julich, Julich, Germany
[4]Thermo Fisher Scientific, Eindhoven, Netherland
E-mail: paolo.rosi@unimore.it

Introduction

The discovery of the possibility to shape electron beam in a similar fashion as photon beams led to the generation of electron vortex beams carrying discrete quanta of Orbital Angular Momentum (OAM). This fact allowed vertical magnetic measurements [1] and opened the road to improvements in the EMCD field, plasmonic and protein dichroism analysis.
The afore mentioned improvements, however, are not possible if the OAM is not efficiently analyzed. In recent years, research groups around the world have started to investigate the most efficient methods of OAM decomposition, namely the OAM sorter based on the conformal mapping of the wavefunction. [1][2][3]
By taking inspiration from optics, the first examples of electron OAM sorters have been realized using holographic phase plates, which demonstrated the feasibility of the experiment, however a major improvement will be obtained when electrostatic phase elements will be utilized [4].
In the last years, our research group focused its efforts in producing increasingly difficult holograms by Focused Ion Beam (FIB) nanofabrication, achieving satisfying results [5]. In the case of holographic production of an electron beam with very high OAM (*l=1000*), when the FIB reached its resolution limit, we used electron beam lithography (EBL) to achieve better resolution. [6]
Here we present a system of two phase holograms to sort the OAM fabricated using Ga-FIB milling. The holograms are both designed using a Fan-Out geometry [7][8]. The name Fan-Out originates from the fact that the beam copies are tiled (Fig.1), and this geometry has proven to be able to reach an experimental separation efficiency >92% in the measurement of the OAM of light [8].
The first hologram (Fig 1) has a blazed profile on one direction and sinusoidal on the other, while the second hologram has a sinusoidal profile. The type of profiles is chosen to increase the signal of the OAM-governed diffraction and produce the so called “multiplexing” of the transmitted beam.

.

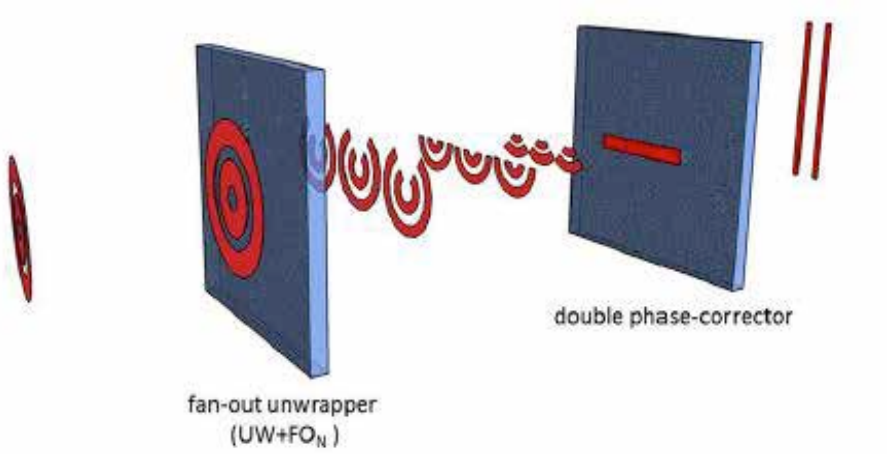

Figure 1: Schematic of a Fan-Out OAM sorter, adapted from [7].

Methods

We started by designing the holograms using STEM_CELL [9]. For the Sorter1 pattern generation a blazed non Fan-Out OAM sorter is multiplied by a sinusoidal grating to obtain the Fan-Out geometry (Fig.2).

After the design is completed, the hologram is reproduced using FIB-Milling. The first phase relies in testing the patterning parameters to obtain the desired groove profile and depth. This process involves finding the right dwell-time, the ideal ion beam current and pixel-size. Final

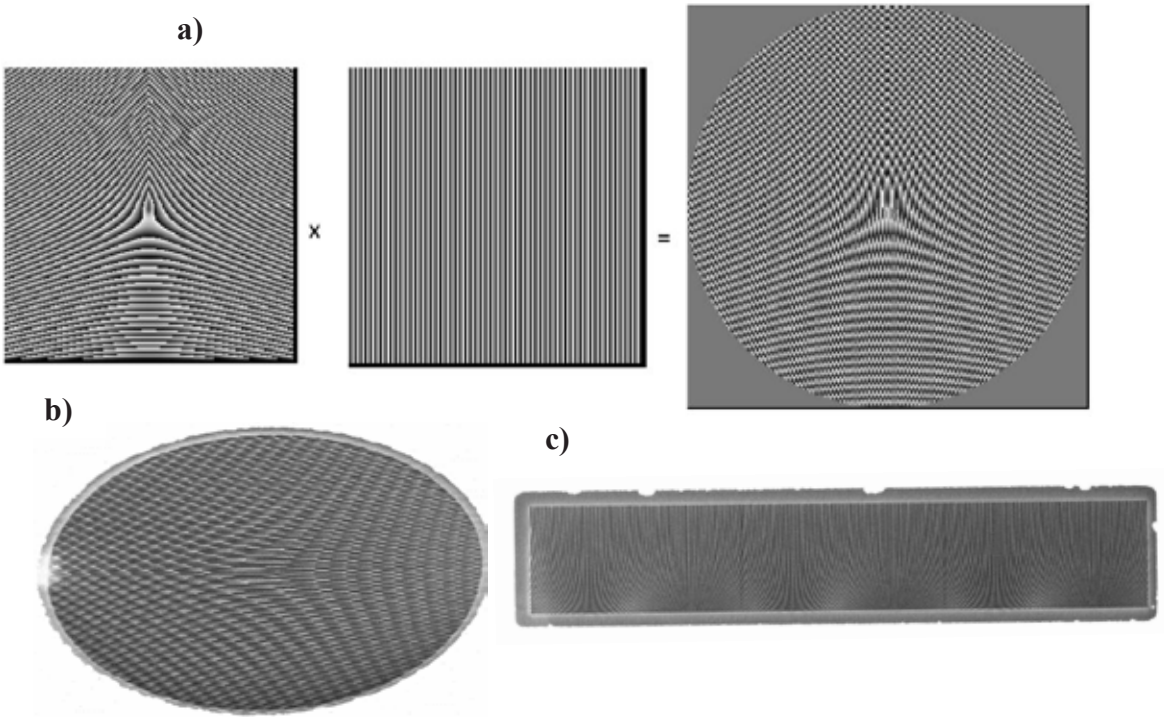

Figure 2: a) the computer design of a Sorter 1 hologram, the Phase-unwrapper hologram b) an HR SEM image of a patterned Sorter1 and c) a HR SEM image of a patterned Sorter2, the phase corrector

testing was performed by analysing the electron diffraction pattern at a Transmission Electron Microscope (TEM).

Results

The resulting diffraction pattern from the TEM analysis of the Fan-Out Sorter1 hologram (Fig.3a), shows two key features: the sinusoidal modulation unwraps the beam in 3 different copies, while the almost blazed profile redirects most of the intensity on one of the first diffraction orders. The effect of the second hologram is evident in Fig.3c.

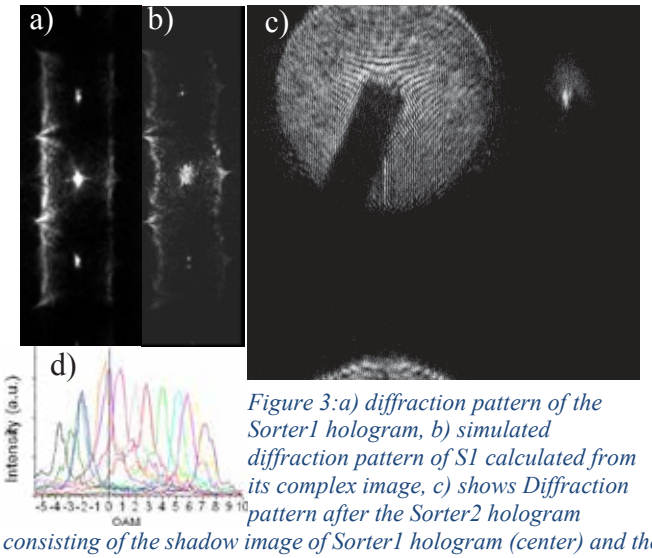

Figure 3:a) diffraction pattern of the Sorter1 hologram, b) simulated diffraction pattern of S1 calculated from its complex image, c) shows Diffraction pattern after the Sorter2 hologram consisting of the shadow image of Sorter1 hologram (center) and the OAM spectrum (right).d) Shows the OAM Spectrum produced by an Electron Vortex-beam Generator resolved by the Fan-Out Sorters.

Moreover, once the two-hologram are mounted in the Objective focal plane and in the Selected Area aperture plane respectively, in order to analyze the OAM of an Electron Vortex Beam (EVB), the resulting spectrum shows a multitude of peaks corresponding to the OAM of the incoming beam and integer multiples of the OAM (Fig.3d). Each peak features significant tails and these can be ascribed to mismatch alignment between the two holograms, aberrations probably induced by charging effects and fabrications imperfection. It is evident that some cross talk in the signal is still present, but the performance is still improved with respect to previous results[1].

Discussion

Holographic phase plates have some known issues like charging under the e-beam and aging, which affect the longevity and performance. Due to recent developments in phase plates, holographic elements will most probably be completely substituted by electrostatic phase plates in a couple of years. However, at the moment, the holographic Fan-Out sorting system is the one which theoretically and experimentally gives the best results from the point of view of OAM sorting resolution, making worth our efforts in developing such system.

References

[1] V. Grillo et al. Nature Communications **8**. 689 (2017)

[2] G.C.G Berkhout, et al. Phys.Rev.Lett.**105**,153601 (2010)

[3] V.Grillo et al. Nature Communications **8**. 15536 (2017)

[4] B.J.McMorran et al. New J.Phys. **19**, 023053 (2017)

[5] H. Larocque et al. Contemporary Physics, doi: 10.1080/00107514.2017.1418046,1-19 (2018)

[6] E. Mafakher et al. Appl. Phys. Lett. **110**, 093113 (2017)

[7] G.Ruffato et al Sci.Rep, **8**, 10248 (2018)

[8] R.W.Boyd et al. Nat.Comm **4**, 2781(2013)

[9] V.Grillo, E.Rotunno, Ultramicroscopy, **125**, (2012)

Electron Magnetic Chiral Dichroism using the Orbital Angular Momentum sorter

E. Rotunno[1], M. Zanfrognini[1], R E. Dunin Borkowski[2], S. Frabboni[1,3], J. Rusz[4], V. Grillo[1]

[1] CNR-NANO, via G Campi 213/a,I-41125 Modena, Italy

[2] Ernst Ruska-Centre for Microscopy and Spectroscopy with Electrons, Forschungszentrum Jülich, 52425, Germany

[3] Università di Modena e Reggio Emilia, via G Campi 213/a,I-41125 Modena, Italy

[4] Uppsala University, P.O. Box 516, 75120, Uppsala Sweden

E-mail: enzo.rotunno@nano.cnr.it

Introduction

Electron magnetic chiral dichroism (EMCD) has attracted a lot of interest due to its promising applications in the study of the magnetic properties of materials, possibly with atomic resolution [1],[2]. Currently two main measurement schemes have been proposed to perform EMCD experiment in a Transmission Electron Microscope (TEM), but both suffer from serious drawbacks.

The first proposition [3] requires working in a two beams condition and collecting the inelastically scattered electrons at two specific positions in the diffraction plane resulting in a very limited spatial resolution, a poor signal to noise ratio, and a strong dependence from the sample thickness. The second, instead, requires two measurements performed using electron vortex beams [4][5] with opposite topological charge. However, two measurements using different probes cannot be precisely performed in the same point, strongly affecting the reliability of the differential measurement implied in EMCD; moreover vortices feature zero intensity in their centre where the atomic column under analysis should be located, therefore the EMCD signal intensity is small.

We propose here an innovative EMCD experiment based on a double dispersion in terms of both energy and Orbital Angular Momentum (OAM) of the inelastically scattered electrons. The theory necessary to describe EMCD experiments will be covered, as well as the influence of finite resolution of the experimental apparatus over the OAM resolved energy loss spectra.

Experimental setup

A magnetic sample, oriented along a high symmetry zone axis, is imaged using a conventional STEM probe defined by a hard circular aperture. The two phase elements composing the OAM sorter [6] should be introduced in the microscope column at the objective and select area diffraction planes to spatially separate the OAM components of the electron beam. An appropriate orientation of these elements with respect to the energy spectrometer is required in order to obtain the double dispersion in energy and OAM in orthogonal directions. This setup offers several advantages over previous propositions of EMCD experiment: the two spectra needed for the EMCD measurements are obtained simultaneously, moreover, being the sample oriented along a high symmetry direction, in combination with the STEM probe, it should allow for in-plane atomic resolution.

Methods

We consider here the simple case of bcc iron oriented along the 001 direction. The STEM probe is characterized by a semi-convergence angle of 7.3 mrad. Dynamical effects related to the propagation of the electrons inside the crystal have been evaluated through a modified version of the software MATSv2 [7]. The inelastic scattering cross section was evaluated by first principles calculations using the WIEN2k package [8] in the generalized gradient approximation of exchange-correlation functional [9], including spin-orbital coupling effects.

Results

In figure 1a we report the simulated spectra obtained for different value of the OAM in the range [-2;2] using a 7mrad collection angle. The dichroism evaluated between the $\ell = 1$ and $\ell = -1$ components is reported along side.

It is worth noticing that the proposed setup allows for a dichroic signal that reaches values of about 15% (or more) at both the L2 and the L3 iron edges, a quantity much larger than the relative dichroic signal normally observed with conventional approaches to EMCD.

Finally, in figure 1b) we present the in plane spatial mapping of the dichroic signal obtained by scanning the STEM probe over the sample, demonstrating atomic resolution.

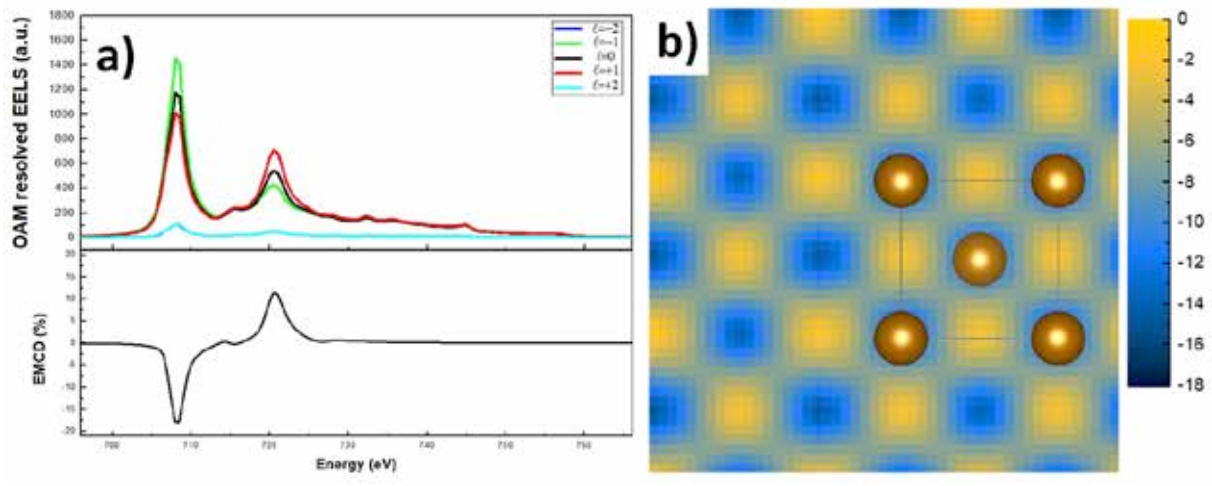

Figure 1: a) OAM resolved EEL spectra computed for l in the range [–2;+2], assuming a collection angle of 7 mrad. **b)** Spatial mapping of the dichorism function computed for the iron L2 edge.

The strength of the relative dichroism is maximum when the electron beam is centered on an atomic column, while it decreases and reaches its minimum if the probe is moved between two columns.

To conclude, our results point out that the proposed technique provides very strong dichroic signals with lateral atomic resolution, even with a limited resolution in OAM, enabling magnetic measurements at the single atomic columns level, with the current technology.

References

[1] P.Schattschneider, S.Rubino, C. Hebert, J.Rusz, J. Junes, P. Kovak, E.Carlino, M.Fabrizioli, G.Panaccione and G.Rossi, Nature 441, 486 (2006).
[2] D. Song, Z. Wang and J. Zhu Ultramicroscopy, 201, 1-17, (2019)
[3] J.Rusz, S.Rubino, P.Schattschneider, Phys. Rev.B, 75, 214425 (2007).
[4] D. Pohl, S.Schneider, P.Zeiger, J.Rusz, P.Tiemeijer, S.Lazar, K.Nielsch and B. RellinghausScientific Reports 7, 934 (2017).
[5] A. Béché, R. Juchtmans, J. Verbeeck, Ultramicroscopy 178, 12-19, (2017)
[6] V. Grillo, A.H.Tavabi, F.Venturi, H. Larocque, R. Balboni, G.C. Gazzadi, S. Frabboni, P.H. Lu, E. Mafakheri, F.Bouchard, R.E. Dunin-Borkowski, R.W. Boyd, M.P.J. Lavery, M.J.Padgett and E. Karimi Nat. Commun. 8, 15536(2017).
[7] Rusz Ultramicroscopy 177, 20-25 (2017).
[8] P. Blaha, K. Schwarz, G. K. H. Madsen, D. Kvasnicka, J. Luitz, R. Laskowski, F. Tran and L. D. Marks, WIEN2k, An Augmented Plane Wave + Local Orbitals Program for Calculating Crystal Properties (Karlheinz Schwarz, Techn. Universität Wien, Austria), 2018. ISBN 3-9501031-1-2
[9] J. P. Perdew, K. Burke and M. Ernzerhof . Phys. Rev. Lett., 77, 3865 (1996)

Vortex filter EMCD: Experimental evidence for sub-nanometre resolution

T. Schachinger[1], S. Löffler[1,2], A. Steiger-Thirsfeld[1], M. Stöger-Pollach[1,2], A. H. Tavabi[3], F. Venturi[4], V. Grillo[5], M. Horák[6], C. Eisenmenger-Sittner[2], R. E. Dunin-Borkowski[3], P. Schattschneider[2]

[1] USTEM, TU Wien, Vienna, Austria
[2] Institute of Solid State Physics, TU Wien, Vienna, Austria
[3] Ernst Ruska-Centre (ER-C), Jülich, Germany
[4] Faculty of Engineering, University of Nottingham, Nottingham, Great Brittan
[5] CNR-Nano, Modena, Italy
[6] CEITEC, Brno University of Technology, Brno, Czech Republic

E-mail: thomas.schachinger@tuwien.ac.at

Introduction

It has long been thought that spin-polarized electron beams are needed to convert the X-ray magnetic circular dichroism technique to the electron microscope. A clever interferometric electron energy-loss (EELS) setup proved this assumption to be wrong [1]. Soon after this seminal work, an intimate connection between electron energy-loss magnetic chiral dichroism (EMCD) and the orbital angular momentum (OAM) of the probing electron has been put forward [2]. In the inelastic scattering process, a chiral electronic transition is induced that obeys the dipole selection rule for the magnetic quantum number $\Delta\mu = \pm 1$ or $\Delta L_z = \pm\hbar$, such that the scattered probe carries OAM (m) in units of $\hbar$, and so-called electron vortex beams (EVBs) of atomic size are produced [3].

In this work, new evidence is given that holographic devices, known as holographic vortex masks (HVMs), typically used to alter the electrons' wave-front in a way that OAM is imparted to the traversing electrons, can be employed to filter the outgoing inelastically scattered electrons for their OAM content, i.e. to yield an EMCD signal. As this approach does not rely on the standard EMCD geometry and the specimen's role as a beam splitter, it does not require a tedious alignment of the crystal, nor a crystal at all. In principle the experiments are done in an imaging STEM [4] like geometry, enabling high lateral resolution EMCD measurements, see Figure 1(a). The difficulties and limitations of this approach have already been pointed out in [5]. Here, a simplified setup and the improvement of the SNR will be addressed.

Methods

The setup shown in Figure 1 (a) was implemented on the Titan Holo at the ERC in Jülich working at 300 kV, equipped with an X-FEG, a GIF Tridiem and a wide gap polepiece, where custom-made objective apertures can be inserted. As a filtering element, a 40 µm high diffraction efficiency sinusoidal phase HVMs with a periodicity of 160 nm has been used. Additional experiments where the vorticity filter is placed in the selected area diffraction (SAD)

aperture holder (see [5]) were performed on a TECNAI F20 working at 200 kV, also equipped with an X-FEG, a GIF Tridiem and using a binary absorption HVM as a filter element. Samples were magnetron sputtered 30 nm Fe on 5 nm SiN_x-membranes and cross-sections of an epitaxially grown 30 nm thick FeRh layer. The in-house inelastic multi-slice simulation (IMS) code (IXCHEL) was used to estimate the effects of defocus, sample thickness and incoherent source size broadening (ISSB) on the EMCD signal.

Results

Figure1 (b) shows rotationally averaged radial profiles of the energy-filtered EVBs after passing 30 nm Fe and careful astigmatism and defocus control. The difference signal, $I_{Diff} = (I_+(r) - I_-(r))/(I_+(r) + I_-(r))$, where $I_\pm(r)$ are the respective EVBs' radial profiles for $m = \pm 1$, can be reproduced using IMS, showing a sub-nanometre spot size.

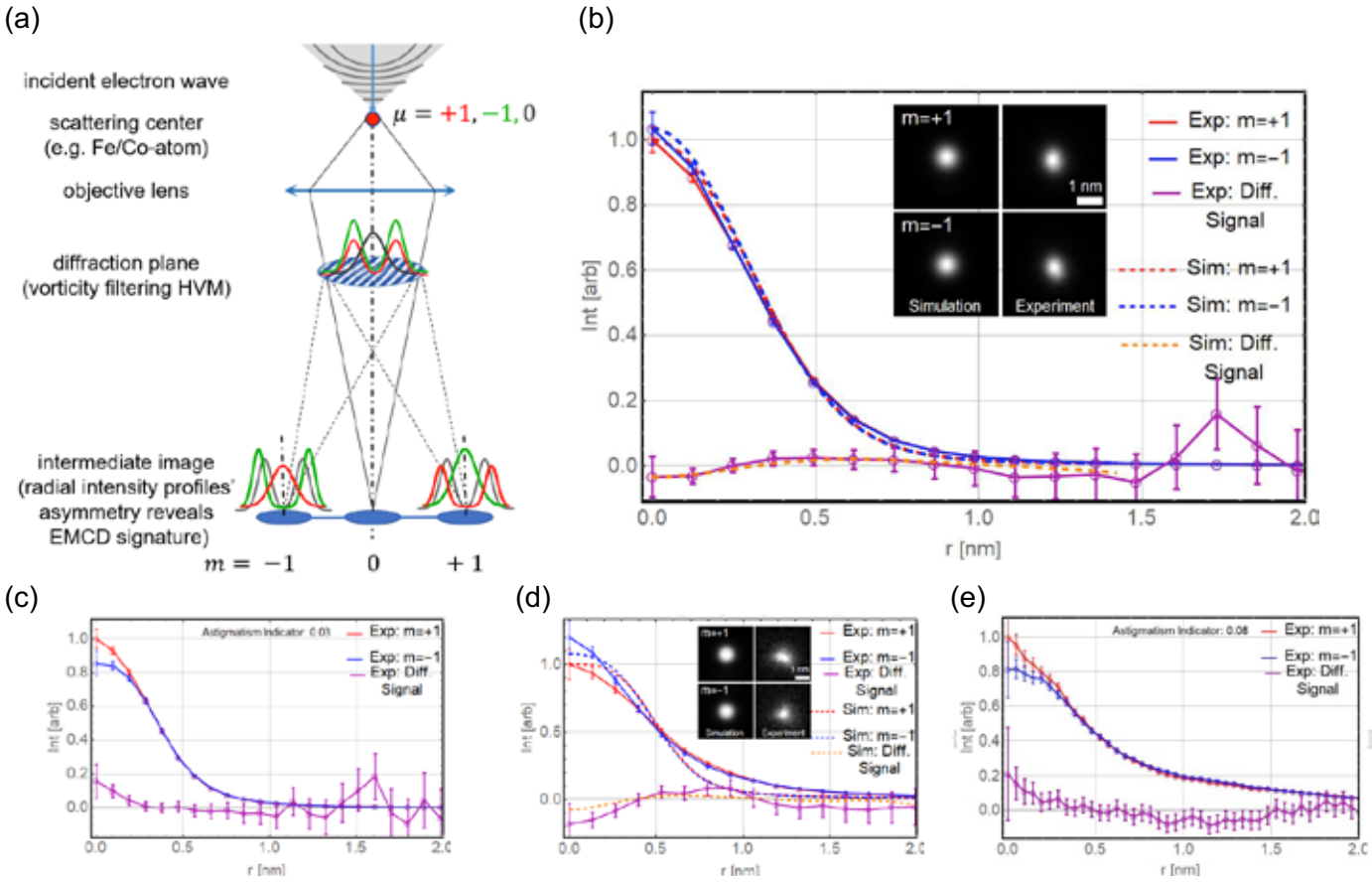

Figure 1: a) Experimental setup of vortex filter EMCD. (b) Rotational average of *m* = ±1 EVBs at 710 eV energy-loss and a 10 eV slit, measured at the Titan Holo at 300 kV on 30 nm Fe and *df* ~ 0 nm, with I_{Diff} curves and the IMS simulation for an ISSB of 0.4 nm. (c), the same as (b) but for the L_2-edge. (d), the same as (b) but for 50 nm FeRh at parallel and (e) anti-parallel lens field, taken at the Tecnai F20.

The radial profiles are normalized to the total intensity in the respective vortex order to account for intensity asymmetries induced by HVM imperfections [5]. Also, a difference signal reversal can be observed for the L_2-edge measurement of the same sample area, see Figure 1 (c).

Figure 1 (d) and (e) were taken on a FeRh alloy, a material with an AFM to FM phase transition at ~400 K, at 450 K. Upon magnetization reversal, the difference signal changes its sign accordingly.

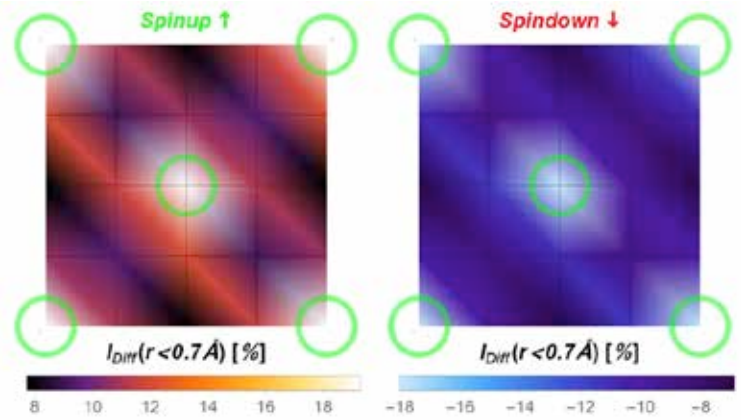

Figure 2: Vortex filter EMCD IMS maps of I_{Diff} over a bcc-Fe unit cell including ISSB, computed for *t* = 30 nm and *α* = 7 mrad, *ß* = 5 mrad, *Cs* = 2.7 mm, *U* = 300 kV, *df* = 73 nm and *ISSB* = 0.1 nm. Green circles represent the Fe-atoms.

Atomic scale IMS mappings including ISSB show a significant variation of I_{Diff} over the unit cell, see Figure 2.

Discussion

Experiments on different machines and samples show difference signals that fit well to IMS simulation accounting for ISSB. Using larger HVMs with higher collection angles improved the SNR but there is still room for improvement of the diffraction efficiency and signal counts. Signal reversals between L_3- and L_2-edges, as well as for parallel and antiparallel magnetisation have been observed, confirming the presence of a faint EMCD signal. Artefact sources like astigmatism and defocus must be carefully controlled. Sub-nanometre resolution could be achieved but IMS mappings suggest that even atomic resolution should be feasible using Cc corrected machines and improved HVMs.

References

[1] P. Schattschneider, Nat. 441, 486-488 (2006)

[2] P. Schattschneider, UM 106, 91-95 (2008)

[3] J. Verbeeck et al., Nat. 467, 301-304 (2010)

[4] A. Rosenauer et al., PRL 113, 096101 (2014)

[5] T. Schachinger et al., UM 179, 15-23 (2017)

[6] Financial support by the ÖAW, HJST (H-294689), FWF (P29687-N36), Horizon 2020 program (Q-SORT, Grant: 766970) and the sample preparation of Arthur Weber is acknowledged.

A simple procedure for the optimization of classical electron magnetic circular dichroism measurements

Sebastian Schneider[1,2], Devendra Negi[3], Matthew J Stolt[4], Song Jin[4], Jakob Spiegelberg[3], Darius Pohl[5,1], Bernd Rellinghaus[5,1], Sebastian TB Goennenwein[2,6], Kornelius Nielsch[1,7], Ján Rusz[3,1]

[1]Institute for Metallic Materials, IFW Dresden, Dresden, Germany
[2]Institut für Festkörper- und Materialphysik, TU Dresden, Dresden, Germany
[3]Department of Physics and Astronomy, Uppsala University, Uppsala, Sweden
[4]Department of Chemistry, University of Wisconsin-Madison, Madison, USA
[5]Dresden Center for Nanoanalysis, TU Dresden, Dresden, Germany
[6]Center for Transport and Devices of Emergent Materials, TU Dresden, Dresden, Germany
[7]TU Dresden, Institute of Materials Science, Dresden, Germany
E-mail: sebastian.schneider@ifw-dresden.de

Introduction

Electron magnetic circular dichroism (EMCD) [1], the electron wave analogue of X-ray magnetic circular dichroism (XMCD), allows for the element specific measurement of the spin and orbital magnetic moments with up to nanometer resolution. Despite being in development for more than a decade, the method has not yet reached widespread employment. The most likely reason for that are dynamical diffraction effects, which severely complicate the EMCD detection and often reduce the signal strength.

Objectives

Therefore, it is necessary to optimize the experimental settings by performing inelastic-scattering calculations in various experimental geometries. To circumvent this step we propose a simple procedure that should help and provide to the experimentalist a set of rules as how to determine the optimal experimental geometry for classical EMCD experiments [2].

Materials & methods

In order to test the proposed optimization procedure these rules are applied to measure a dichroic signal in the field-polarized phase of the helimagnet FeGe. To stabilize this phase the classically prepared sample is cooled to 90 K using a liquid nitrogen TEM holder, and the sample is then exposed to the field of the fully excited objective lens (B = 2.2 T), resulting in a ferromagnet like parallel alignment of all magnetic moments of the material with respect to the external magnetic field (cf. Fig. 1 (a)).

Results

By explicitly reviewing the theory of EMCD in two- and three-beam orientations we can identify a pre-factor that is so far not considered in theory and that scales with the dichroic signal strength. This expression, which is very similar to a structure factor, although the summation is limited to the magnetic atoms of the unit cell only, is introduced as *partial structure factor*. When applied to FeGe the highest *partial structure factor* is found for a two-beam orientation with **G** = {400}. In contrast the partial structure factor for a three-beam case with **G** = {200} is significantly reduced. By explicitly calculating the EMCD signal in the diffraction plane it can be confirmed, that the dichroic signal strength is much more pronounced for the two-beam case (cf. Fig. 1 (b) and (c)). In subsequent experiments a clear EMCD signal can be measured for the two-beam orientation, whereas the dichroic signal is not detectable in the three-beam case (cf. Fig. 2).

Conclusion

By providing the crystal structure and assuming the magnetic structure it is possible to calculate the partial structure factor of an arbitrary material, which enables the possibility to choose the optimal experimental orientation for an EMCD experiment. Likewise calculations, simulations and experiments on the field-polarized phase of FeGe confirm the applicability of this easy procedure. Future works on FeGe aim to measure a spatially resolved EMCD signal of the Skyrmion phase to gain further inside into three dimensional spin texture of these magnetic quasiparticles complementary to holographic measurements [3].

References

[1] Schattschneider et al., Nature **441** (2006), p. 486.
[2] Schneider et al., Physical Review Materials **2** (2018), p. 113801.
[3] Schneider et al., Physical Review Letters **120** (2018), p. 217201.

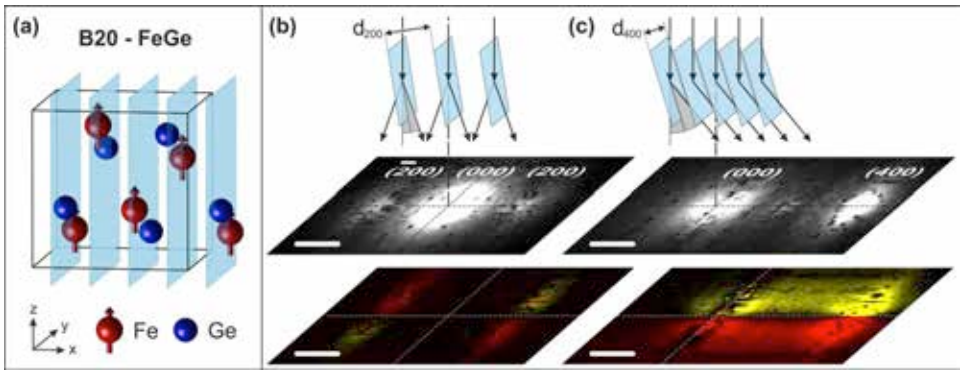

Fig. 1.: (a) Crystallographic unit cell of stoichiometric FeGe in the B20 structure. The blue sheets indicate the {200} and {400} lattice planes. Schematic illustration of the Bragg scattering of 300 keV electrons, which impinge on a B20 FeGe crystal under (b) (−200)(000)(200) three-beam orientation and (c) (000)(400) two-beam condition. Both the calculated diffraction patterns (upper grey scale maps) and EMCD maps (lower, colored maps) are shown for each of these cases (scale bars = 5 mrad).

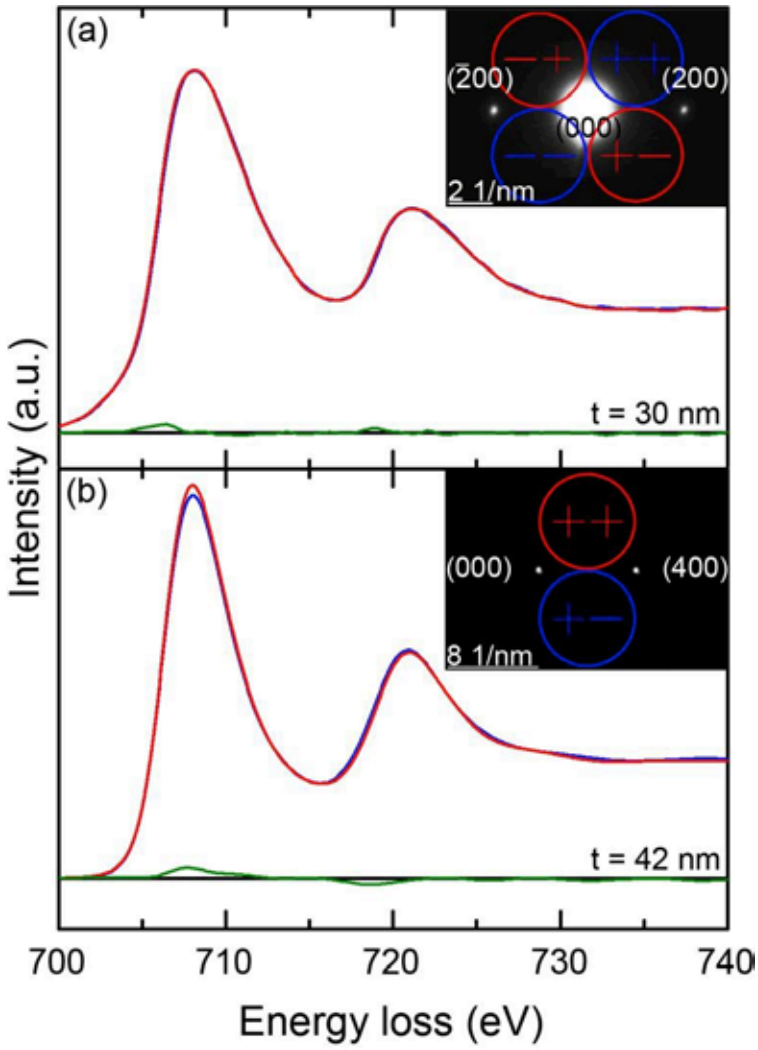

Fig. 2.: EEL spectra measured in two- and three-beam conditions with their respective EMCD signal (difference) in green. The aperture positions corresponding to the spectra are displayed as inset.

Control of free electrons in the vicinity of dielectric nanostructures

N. Schönenberger[1], A. Mittelbach[1], J. Illmer[1], P. Yousefi[1], U. Niedermayer[2], R. Shiloh[1], P. Hommelhoff[1]

[1]Lehrstuhl für Laserphysik, Friedrich-Alexander-Universität Erlangen-Nürnberg, Germany
[2] TU Darmstadt, Germany
E-mail: norbert.schoenenberger@fau.de

Introduction

Making use of the ever growing field of dielectric laser accelerators (DLAs), where free electrons can be controlled by the interaction with near field modes, either synchronous or asynchronous, of laser illuminated dielectric structures, known as the inverse Smith-Purcell effect and the development of more advanced structures we show control of the phase space in the sub cycle regime of the driving laser.

We show latest results, obtained in our ultrafast scanning electron microscope [1], of controlling longitudinal and transversal [2] phase spaces of bunch trains.

References

[1] Ultrafast scanning electron microscope applied for studying the interaction between free electrons and optical near-fields of periodic nanostructures, M. Kozak, J. McNeur, N. Schönenberger, J. Illmer, A. Li, A. Tafel, P. Yousefi, T. Eckstein, P.Hommelhoff, Journal of Applied Physics **124** (2018)

[2] Alternating-Phase Focusing for Dielectric-Laser Acceleration, Uwe Niedermayer, Thilo Egenolf, Oliver Boine-Frankenheim, and Peter Hommelhoff, Phys. Rev. Lett. **121**, 214801 (2018)

Attosecond electron bunch creation in optical traveling waves via ponderomotive scattering

N. Schönenberger[1], M. Kozák[2], P. Hommelhoff[1]

[1]Lehrstuhl für Laserphysik, Friedrich-Alexander-Universität Erlangen-Nürnberg, Germany
[2] now with Charles University Prague, Prague, Czech Republic, EU
E-mail: norbert.schoenenberger@fau.de

Introduction

Many atomic, molecular and other condensed matter structures have not been fully studied yet at ultrafast timescales because adequate probing methods, like XUV, ultrafast electron diffraction and microscopy, are only now becoming available. Here, we report on the ponderomotive interaction of electrons with optical traveling waves and the ultrashort electron bunch trains generated after this interaction [1]. Such bunch trains could be the basis of such a probing method. In the interaction, the travelling waves are created by the superposition of two laser pulses at different frequencies intersecting at specific angles to ensure phase matching with the electrons. This technique allows for a strong energy modulation of the free electrons of 2.2 GeV/m. Even higher gradients could be achievable, as the ponderomotive force is only limited by the available laser power. Subsequent dispersive propagation of the electrons in free space causes ballistic microbunching on the sub cycle timescale. This bunching is detected via a second ponderomotive interaction at the temporal focus. Spectrograms recorded in this setup in conjunction with numerical simulations are used to determine that pulse trains of 300 as pulses are formed.

References

[1] Inelastic ponderomotive scattering of electrons at a high-intensity optical travelling wave in vacuum, M. Kozak, T. Eckstein, N. Schönenberger, P.Hommelhoff, Nature Physics 14 (2018), S. 121–125

[2] Ponderomotive Generation and Detection of Attosecond Free-Electron Pulse Trains, M. Kozak, N. Schönenberger, P. Hommelhoff, Physical Review Letters 120 (2018), Art.Nr.: 103203

Sub-relativistic electrons in dielectric acceleration and ultrafast interactions

Roy Shiloh, Peyman Yousefi, Norbert Schönenberger, Johannes Illmer, Ang Li, Alex Tafel, Anna Mittelbach, and Peter Hommelhoff

Department of Physics, Friedrich-Alexander-Universität Erlangen-Nürnberg (FAU), Staudtstrasse 1, 91058 Erlangen, Germany
E-mail: roy.shiloh@fau.de

Free electron sources, driven by femtosecond UV lasers, can provide electron pulses with high temporal and spatial coherence. These electrons can then be arranged to interact in space and time with another laser pulse, such that further manipulation of the electrons can be made in an extremely fast and precise setting. The interaction can be mediated, for example, in free space using a ponderomotive scheme, or by employing nano-structures and using the generated, engineered near-fields.

A prominent example of such an experiment is routinely done in our group in the framework of dielectric laser acceleration [1,2]: toward the aim of accelerating sub-relativistic electrons to high energies with practical survivability rates, we must first prepare the electron beam to match the requirements of the accelerating structures in space and time [3]. This can be done, for example, using ponderomotive schemes [4]. We then must continuously manipulate the beam by confining, steering, bunching, and focusing throughout the acceleration section. Strict tolerances in the spatial and temporal domains have to be met in this scheme, due to the tiny dimensions of the devices. In this talk I will present some of the challenges and solutions we're working on.

References

[1] J. McNeur, M. Kozák, N. Schönenberger, K. J. Leedle, H. Deng, A. Ceballos, H. Hoogland, A. Ruehl, I. Hartl, R. Holzwarth, O. Solgaard, J. S. Harris, R. L. Byer, and P. Hommelhoff, Optica **5**, 687 (2018).

[2] M. Kozák, J. McNeur, N. Schönenberger, J. Illmer, A. Li, A. Tafel, P. Yousefi, T. Eckstein, and P. Hommelhoff, J. Appl. Phys. **124**, 023104 (2018).

[3] U. Niedermayer, T. Egenolf, O. Boine-Frankenheim, and P. Hommelhoff, Phys. Rev. Lett. **121**, 214801 (2018).

[4] M. Kozák, N. Schönenberger, and P. Hommelhoff, Phys. Rev. Lett. **120**, 103203 (2018).

Optimal electrode design for Programmable Phase Plates for use in electron microscopes

H. Soltner[1], V. Grillo[2], P. Lu[3], R.E. Dunin-Borkowski[3]

[1]Central Institute of Engineering, Electronics and Analytics (ZEA-1), Forschungszentrum Jülich GmbH, 52425 Jülich, Germany
[2]CNR-Istituto Nanoscienze, Centro S3, Via G Campi213/a, I-41125 Modena, Italy
[3]Ernst-Ruska Centre for Microscopy and Spectroscopy with Electrons and Peter Grünberg Institute, Forschungszentrum Jülich GmbH, 52425 Jülich, Germany
E-mail: h.soltner@fz-juelich.de

Introduction

The phase manipulation of an electron beam can be achieved by the application of electrostatic or magnetostatic fields along the electron beam. Due to space restrictions in electron microscopes, thin devices supporting such fields are advantageous. Nowadays dedicated 2-dimensional chips can be manufactured by nanofabrication, paving the way for many types of devices. The phase of the electron wave, however, depends on the integrated potential in both cases, a quantity, which is not directly accessible experimentally, but which has to be calculated beforehand. Specifically, in order to optimize a particular device the corresponding inverse problem, i.e., the design of an electric or magnetic structure from knowledge of the specified field integrals has to be carried out analytically or numerically. This contribution highlights such approaches for programmable phase plates (PPP) in electron microscopes.

Atomic-plane-resolved electron magnetic chiral dichroism using a defocused electron beam

D. Song and R. E. Dunin-Borkowski

[1]Ernst Ruska-Centre for Microscopy and Spectroscopy with Electrons and Peter Grünberg Institute, Forschungszentrum Jülich, 52425 Jülich, Germany

E-mail: d.song@fz-juelich.de and r.dunin-borkowski@fz-juelich.de

Introduction

High spatial resolution electron magnetic chiral dichroism (EMCD) in the transmission electron microscope (TEM) has been developed using several approaches: (1) Parallel and serial scanning TEM (STEM) EMCD[1], whose spatial resolution of 1 nm[2] can be extended towards the atomic scale by using patterned apertures[3]; (2) Beam-shift EMCD with atomic plane resolution in a probe-corrected STEM[4]; (3) Chromatic-aberration-corrected TEM of atomic-plane-resolved EMCD signals[5]; (4) Vortex EMCD, which has been proposed theoretically for atomic column-by-column EMCD[6]; (5) Phase-shaped electron probes for atomic column-by-column EMCD, in particular using four-fold astigmatism[7,8]. However, none of these methods are yet widespread because of their limitations and challenges. Here, we concentrate on beam-shift EMCD, which can be implemented in a modern probe-corrected STEM that is equipped with electron energy-loss spectroscopy (EELS). We show that a defocused beam can be used to enhance EMCD signals from single atomic planes.

Methods

The beam-shift EMCD technique using an atomic-sized electron beam is typically implemented in a probe-corrected STEM[4]. A large semi-convergence angle is used to achieve atomic-resolution STEM imaging, as well as coherent overlap of diffracted discs and direct beams. A phase shift is introduced by using a controlled beam displacement during scanning of the electron beam across atomic planes in a three-beam orientation, as shown in Fig. 1(a). The simulations shown in Fig. 1(b) illustrate the distribution of the EMCD signal for a beam positioned at different distances from an atomic plane. A key advantage of using beam-shift EMCD is the use of a single aperture to acquire EELS signals from the area marked by a red rectangle in Fig. 1(b). One expects to detect positive and negative EMCD signals at distances of d/4 and 3d/4 from an atomic plane (where d is the atomic plane spacing) during STEM line scanning. By subtracting the EELS signals recorded at these two positions, a beam-shift EMCD signal for this atomic plane is obtained.

We performed simulations using MATS v2 software, which was provided by Jan Rusz[9] and can include vortex and aberrated beams. We studied *bcc* Fe (a = 0.286 nm) at an accelerating voltage (V) of 300 kV. A supercell was constructed along the [016] direction to simulate a (200) three-beam orientation. The simulations were performed over ±40 mrad in the diffraction plane, where $G_{(100)}$ = 6.89 mrad at 300 kV. The beam position, convergence semi-angle (CA), specimen thickness (t) and defocus are summarised in Fig. 1(a).

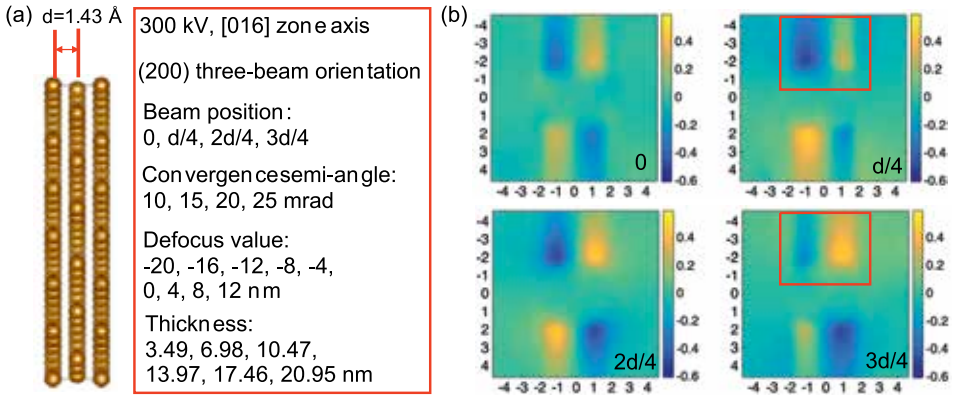

Fig. 1. Simulation setup for *bcc* Fe. (a) Atomic model of Fe in a (200) three-beam orientation and calculation parameters. (b) Reciprocal space maps of beam-shift EMCD signals for different beam positions. The red rectangles show the position of the aperture used for signal acquisition. The calculation parameters are: V = 300 kV, t = 10.47 nm, CA = 15 mrad; zero defocus.

Results

Beam-shift EMCD signals were calculated as a function of beam position, convergence semi-angle, specimen thickness and defocus. Figure 2 shows reciprocal space maps of beam-shift EMCD signals for different defocus values for t = 10.47 nm and CA = 15 mrad. The signals are strongly enhanced close to a defocus of -8 nm. For such an underfocused electron beam, the maximum beam-shift EMCD signal occurs at a defocus that approaches the thickness of the specimen. The EMCD signals are modulated by double channelling, while the defocused beam also affects the outgoing conditions. In contrast to the use of plane wave illumination, by focusing the beam at a certain depth in the specimen a balance can be achieved between incoming and outgoing conditions to provide the strongest EMCD signals. Conversely, the signals are decreased when using overfocused conditions, because the probe is largely spread before entering the crystal and the increased delocalization of the signals leads to decreased intensity.

Optimized defocus values were determined as a function of convergence semi-angle and specimen thickness. When using a smaller convergence semi-angle, the beam-shift EMCD signals vary slightly with defocus, as shown in Fig. 3. The use of a large convergence semi-angle results in a small depth of focus ($1.77\lambda/\alpha^2$), with the EMCD signals becoming more sensitive to defocus within a narrow range. The optimized defocus is almost unchanged with convergence angle and is modulated by the specimen thickness (see Fig. 4). The optimized underdefocus value can be estimated to be slightly smaller than the specimen thickness, providing an experimental guideline to achieve enhanced beam-shift EMCD signals.

Discussion

The simulations show that a defocused beam can be used to enhance beam-shift EMCD signals for atomic-plane-resolved magnetic measurements.

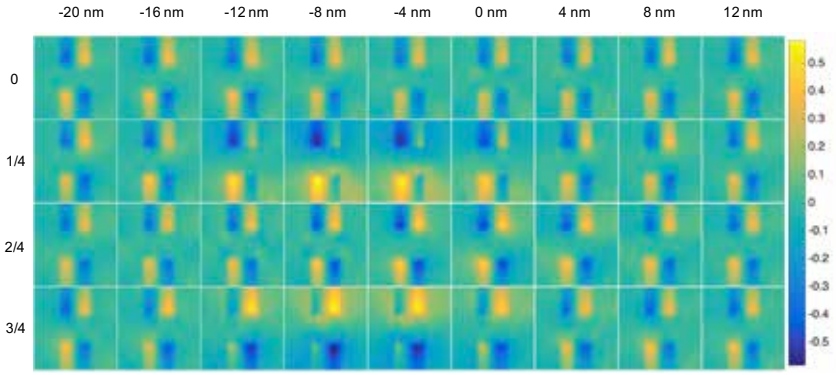

Fig. 2 Reciprocal space maps of beam-shift EMCD signals for different beam positions and defocus values. V = 300 kV, t = 10.47 nm, CA = 15 mrad.

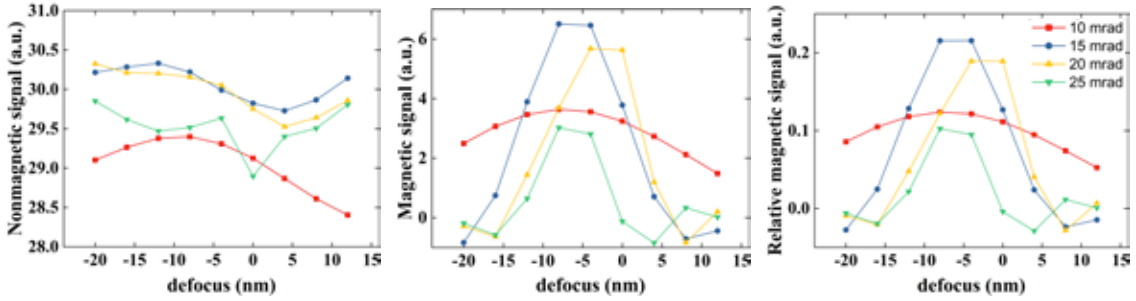

Fig. 3. Non-magnetic (left), magnetic (middle) and relative (right) magnetic beam-shift EMCD signals plotted as a function of defocus for different convergence semi-angles. V = 300 kV, t = 10.47 nm. The signals are integrated over the aperture area marked in Fig. 1(b).

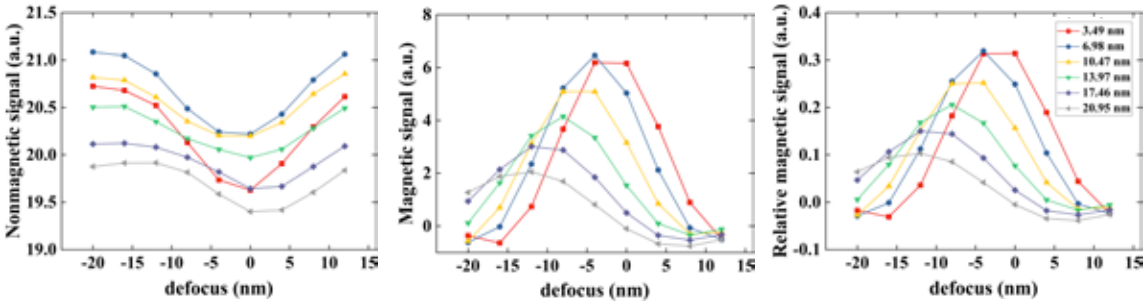

Fig. 4. As for Fig. 3 but for different specimen thicknesses. V = 300 kV, CA = 15 mrad.

References

1. Schattschneider, P. Linear and Chiral Dichroism in the Electron Microscope. *CRC Press* (2012)
2. Thersleff, T., Rusz, J., Hjörvarsson, B. & Leifer, K.. *Physical Review B* **94**, (2016).
3. Negi, D. *et al. Physical Review Letters* **122**, 037201 (2019).
4. Rusz, J. *et al. Nature Communications* **7**, 12672 (2016).
5. Wang, Z. *et al. Nature Materials* **17**, 221–225 (2018).
6. Rusz, J. & Bhowmick, S. *Physical Review Letters* **111**, 105504 (2013).
7. Rusz, J., Idrobo, J.-C. & Bhowmick, S. *Physical Review Letters.* **113**, 145501 (2014).
8. Idrobo, J. C. *et al. Adv. Struct. Chem. Imag.* **2**, 5 (2016).
9. Rusz, J. *Ultramicroscopy* **177**, 20–25 (2017).

High spectral resolution EELS and CL to probe optical properties at the nanometer scale

Luiz H. G. Tizei[1], Noémie Bonnet[1], Hugo Lourenço-Martins[1], Marcel Tencé[1], Jean-Denis Blazit[1], Xiaoyan Li[1], Alberto Zobelli[1], Alexandre Gloter[1], Odile Stéphan[1] and Mathieu Kociak[1]

[1]Laboratoire de Physique des Solides, Université Paris-Sud, CNRS-UMR 8502, Orsay 91405, France
E-mail: luiz.galvao-tizei@u-psud.fr

The remarkable energy resolution and control achievable in all-optical experiments makes it a hard contender against new designs and developments in other spectroscopies, at least in the optical range. However, this high precision means that even nanometer scale changes to the object under study have a detectable spectral effect . For example, a 10 nm length change on a micrometer-long metallic rod leads to an energy shift of the order of 1 meV, roughly. Hence, the necessity of coupling high spatial resolution to high spectral resolution. Up until recently, this bridge was crossed by performing complementary electron microscopy measurements at high spatial resolution in addition to optical measurements either ex or in situ.

Yet, the use of electron energy loss spectroscopy (EELS) and cathodoluminescence (CL) in different configurations and with increased spatial and spectral resolutions has shown there are many benefits in using electron beams for spectroscopy, at least where nanometer scale features are relevant. More importantly, the remarkable spectral resolution in experiments with focused electron beams [1-4] achieved in the previous few years makes EELS a powerful companion to all-optical spectroscopies. In this contribution, we will describe some of these capabilities using two experiments as examples.

In the first one, we will show that CL and photoluminescence (PL) of nitrogen-vacancy (NV) centers in diamond can be obtained from the same object using a light injection/collection system installed in an electron microscope. This system allows us to collect light emitted from the NV centers under laser, electron or both excitations. We observed that, as reported previously [5], that only the uncharged state of the NV center (NV^0) is observed in under electron excitation, while both the NV^0 and the NV^- are seen in PL (as recently reported by S. Meuret *et al* [6]), for the same object. Understanding the differences between the excitation mechanisms might give us hints on how to control the charge state of this defect under electron irradiation.

In the second experiment, concerning high spectral resolution (< 10 meV) at high spatial resolution (< 10 nm) EELS, we will discuss the mapping of surface phonon modes on h-BN flakes of varying thickness (Figure 2). As it has been discussed in the literature, EELS

measures the Fuchs-Kliewer (FK) modes [7,8]. The physics of these excitations is very similar to that of surface plasmon modes in metal nanoparticles [6]. As expected we observe two FK modes at 173 meV and 195 meV. The intensity of these modes changes as a function of the thickness of the h-BN flake. Initially with the electron beam in aloof geometry only the lower energy mode is observed. The intensity of the second mode increases as a function of the thickness of the flake. This is expected because of the symmetry of the eigencharge of this mode, which is symmetric between the two surfaces (similarly to what is observed in a thin metal film).

Finally, the experiments presented above were performed on the ChromaTEM microscope, a modified Nion Hermes 200 with a cold sample stage. We will present some more recent results on nanoscale plasmon physics obtained with this machine.

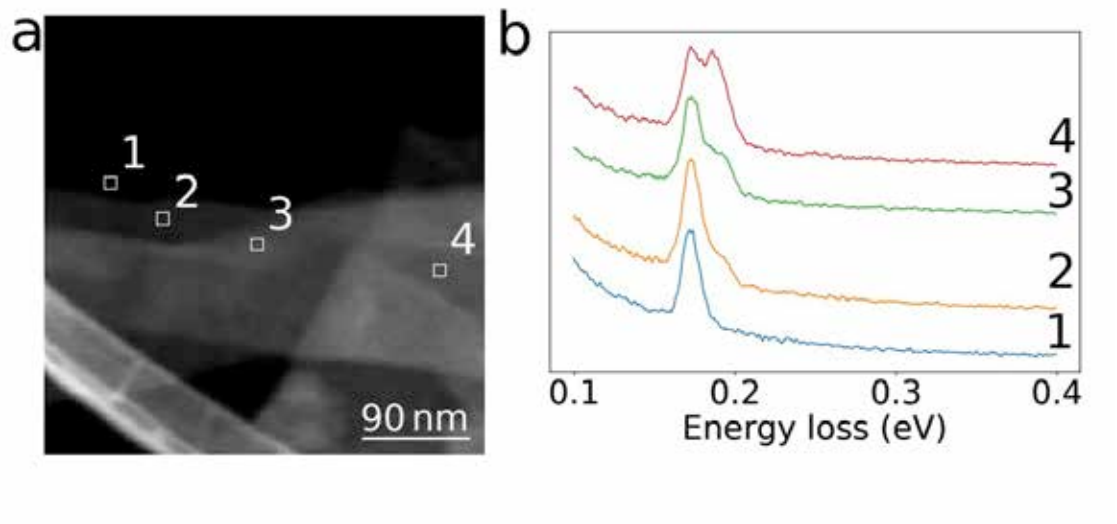

Fig. 1 a) High angle annular dark field image of an h-BN flake. b) Four spectra averaged from an hyperspectral image in the regions marked 1-4. Initially, with the beam in vacuum, only a single peak is observed at 173 meV. As the beam is positioned towards thicker parts of the flake, a peak at 195 meV appears, with increasing intensity.

Methods

Two electron microscopes have been used in the experiments described above. For the higher spatial resolution CL and PL experiments a VG HB501 microscope operated at 60 keV was used. This microscope is equipped with a light collection/injection system based on a parabolic mirror. The sample was kept at 150 K.
A Nion 200 Hermes equipped with an electron monochromator and cold field emission gun (operated at 60 keV) was use for the high resolution EELS experiments. The maximum energy resolution of this setup is 6 meV.

References

[1] O. Krivanek et al, Nature **514**, 209 (2014)
[2] L. H. G. Tizei et al, Phys. Rev. Lett. **114**, 107601 (2015)
[3] M. J. Lagos et al, Nature **543**, 529 (2017)
[4] F. S. Hage et al, Sci. Adv. **4**, eaar7495 2018)
[5] L. H. G. Tizei and M. Kociak, Nanotechnology **23**, 175702 (2012)
[6] S. Meuret, private communications (2018)
[7] R. Fuchs and K. L. Kliewer, Phys. Rev. **140**, A2076 (1965)
[8] H. Lourenço-Martins, Phys. Rev. X **7**, 041059 (2017)
[9] S. Author, Journal **100**, 101101 (2009)

Dihedral plasmonics: from optical skyrmions to novel spin-orbit interaction of light

Shai Tsesses[1], Evgeny Ostrovsky[1], Kobi Cohen[1], Bergin Gjonaj[1,2], Netanel H. Lindner[1] and Guy Bartal[1]

[1] Technion – Israel Institute of Technology, Haifa, Israel
[2]Albanian University, Tirana, Albania
E-mail: tsesses@campus.technion.ac.il

Skyrmions are topologically stable field formations [1], which exist in a limited range of physical systems. Most famously, they appear in chiral magnets [2], and are currently considered a promising route towards high-density magnetic information storage and transfer, as well as a possible tool in the field of spintronics. However, skyrmions are scarcely used outside the field of magnetism and have never been demonstrated before in the field of optics. In my talk, I will present the generation of a skyrmion lattice in the electric field of surface plasmon polaritons (SPPs), imaged by phase-resolved near-field optical microscopy [3]. I will show how the optical skyrmion lattice exhibits robustness to imperfections while the topological domain walls in the lattice can be continuously tuned, changing the spatial texture of the skyrmions from bubble-type [4] to Néel-type [5].

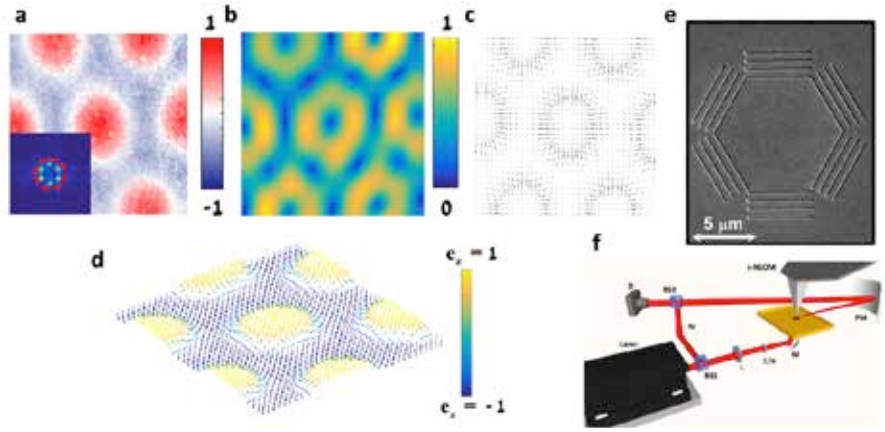

Fig. 1. Measurement of an optical skyrmion lattice created by surface plasmon polaritons. Measured out-of-plane electric field (a), from which the amplitude of the in-plane electric field (b), its vector representation (c) and the local unit vector of the electric field (d) are extracted, exhibiting a bubble-type skyrmion lattice. Inset (a) is the Fourier decomposition of the out-of-plane field, with the red circle representing a low-pass filter used to derive the in-plane field. e) SEM image of the sample - six gratings on a 200 nm Au layer. The grating periodicity corresponds to the plasmonic wavelength (636 nm) and a single grating is displaced from a perfect hexagon by half the plasmonic wavelength. The optical skyrmion lattice is created at the center of the excitation slit, according to the boundary conditions enforced on the SPPs. f) Illustration of the experimental setup. BS1,BS2 – beam splitter; L – weakly focusing lens; $\lambda/4$ - quarter-wavelength plate; M – mirror; PM – parabolic mirror; D – detector.

This discovery is enabled by the unique interaction of circularly polarized light with polygon plasmonic excitation slits [6] which is a special form of the spin-based plasmonic effect [7], stemming from the spin-orbit interaction (SOI) of light [8]. The interaction with hexagonal slits

results in four topologically different plasmonic lattices, controlled by engineered boundary conditions, and reveal a cyclic nature of the spin-based plasmonic effect which does not exist for circular symmetry. Finally, through the calculation of optical forces and PINEM effect generated by the plasmonic lattices, I will show how these unique field configurations can exert forces on nanoparticles and imprint topological charges on electron beams.

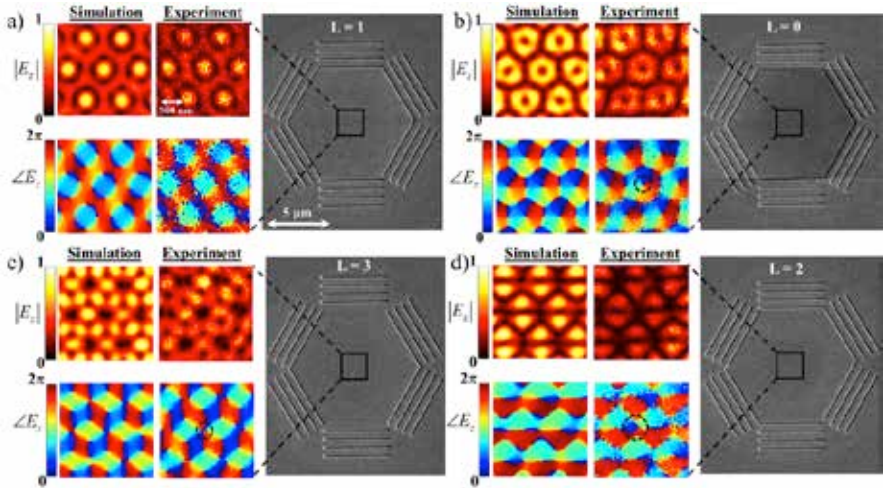

Fig. 2. Measurements of the spin-orbit interaction of light in plasmonic lattices. (a)-(d) simulated and measured amplitude (top) and phase (bottom) of plasmonic lattices created by the spin-based plasmonic effect in hexagonal symmetry. The topological charge at every lattice site is either (a) 0, (b) 1, (c) 2 or (d) 3. In (a) and (c), the impinging light handedness was left-circular, whereas in (b) and (d) – the handedness was right-circular. Each figure also contains an SEM image of the corresponding excitation slit used to generate the plasmonic lattice. Vortex points are encircled for convenience, scale bars are given in (a) and the presented area of the lattices is marked on each slit image (square).

References

[1] T. H. R. Skyrme, "A unified field theory of mesons and baryons," Nucl. Phys. **31**, 556–569 (1962).

[2] P. B. S. Mühlbauer *et al.*, "Skyrmion Lattice in a Chiral Magnet," Science **323**, 915–920 (2009).

[3] S. Tsesses, E. Ostrovsky, K. Cohen, B. Gjonaj, N. H. Lindner, G. Bartal, "Optical skyrmion lattice in evanescent electromagnetic fields," Science **361**, 993-996 (2018).

[4] J. P. Liu, Z. Zhang and G. Zhao, *Skyrmions: Topological Structures, Properties, and Applications* (CRC Press, 2016), Chap. 1.

[5] I. Kezsmarki *et al.*, "Neel-type skyrmion lattice with confined orientation in the polar magnetic semiconductor GaV4S8," *Nat. Mater.* **14**, 1116–1122 (2015).

[6] S. Tsesses, K. Cohen, E. Ostrovsky, B. Gjonaj, G. Bartal, "Spin-orbit interaction of light in plasmonic lattices," Under Review (2019).

[7] Y. Gorodetski, A. Niv, V. Kleiner, E. Hasman, "Observation of the Spin-Based Plasmonic Effect in Nanoscale Structures," *Phys. Rev. Lett.* **101**, 043903 (2008).

[8] K. Y. Bliokh, F. J. Rodríguez-Fortuño, F. Nori, A. V. Zayats, "Spin-Orbit Interactions of Light," *Nat. Photonics* **9**, 796–808 (2015).

Structured detection and structured illumination in constant-dose particle counting experiments

W. Van den Broek,[1] B.W. Reed,[2] A. Béché,[3] J. Verbeeck,[3] C.T. Koch.[1]

[1] *Institut für Physik & IRIS Adlershof, Humboldt-Universität zu Berlin, 12489 Berlin, Germany*

[2] *Integrated Dynamic Electron Solutions, Inc., Pleasanton CA 94588, US*

[3] *EMAT, Antwerp University, 2020 Antwerp, Belgium*

e-mail: vandenbroek@physik.hu-berlin.de

Introduction

The utility of structured detection (SD) and structured illumination (SI) lies in their suitability for compressed sensing (CS) [1], thus enabling the retrieval of a signal from a surprisingly small number of measurements. In this work the different behavior of SD and SI in terms of collected flux and the ensuing implications of the associated Poisson noise on the quality of the retrieved signal are investigated. This leads to a comprehensive figure of merit, the detective quantum efficiency (DQE), that can readily be used to predict optimal experimental settings for a constant dose on the object.

SD in particle counting experiments is achieved by overlaying the flux of particles emanating from the object with a pseudo-random pattern followed by an integration to yield the recordings. A well-known example is the single-pixel camera [1] in Figure 1. In the case of SI the flux of particles impinging on the object is given a pseudo-random pattern and integrating the emanating flux yields the recordings. In this work SI is represented by the annular dark field scanning transmission electron microscopy (ADF-STEM) depicted in Figure 1.

Both the SD and SI signal formation process is linear, $\mathrm{E}(y) = IAx$, with E the expectation value, y the $M \times 1$ recorded signal, x the two-dimensional object in long-vector format ($N \times 1$), A the

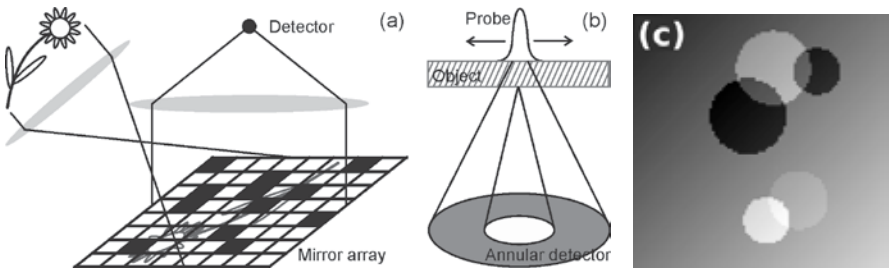

Figure 1: (*a*): For the single-pixel camera the flux emanating from the scene is projected onto an array of switchable mirrors forming a pseudo-random pattern, and the reflected light is focused into a detector located in the conjugate plane. (*b*) In ADF-STEM an electron probe visits a number of pseudo-randomly chosen locations on the object, the electrons scattered to higher angles are integrated in an annular detector in the far-field. (*c*): The Ramp-Discs phantom.

so-called sensing matrix overlaying the respective patterns, and $I\mu$ the average number of particles reflecting off each of the object's pixels, with μ the average of x.

The parameter of interest in this work is p – the fraction of mirrors switched on in SD, or locations visited in SI – and its optimal value p_{opt} is sought for. While in SD the number of particles in the recorded signal scales directly with p, this number can be kept constant in SI because of direct control in terms of scan speed and beam intensity. This is reflected in a different expression for the elements of the respective sensing matrices A: elements corresponding to on-mirrors in SD are set to $1/M$ and the others to 0, for SI these values are $1/(pN)$ and 0, respectively.

Methods

The DQE is defined as

$$\text{DQE} = \frac{M}{N}\frac{\text{SNR}_y^2}{\text{SNR}_{\text{ref}}^2}, \tag{1}$$

with SNR_y the signal-to-noise ratio of the recorded signal y and SNR_{ref} that of an hypothetical ideal reference image where an ideal (and thus merely Poisson-limited) detector is assumed in lieu of each mirror in SD or on each location for SI. The factor M/N accounts for the different number of measurements in both cases. Following [2], explicit expressions are obtained for SD and SI respectively:

$$\text{DQE}_{\text{SD}} = \frac{p(1-p)}{pN + Mc/(I\mu)} \quad \text{and} \quad \text{DQE}_{\text{SI}} = \frac{1-p}{pN}\frac{1}{1+c/(I\mu)}. \tag{2}$$

Where c is the variance of the zero-mean Gaussian read-out noise in the detectors.

The validity of this approach is tested by comparing DQE^{-1} to the mean squared error (MSE) of reconstructions obtained from the expected likelihood method described in [2]. For SD, simulations from the Ramp-Discs phantom in Figure 1 were used with $\mu = 0.53$, $N = 1\text{e}4$, $M = 2\text{e}3$, $I = 7.5\text{e}5$, and $\sqrt{c} = 1.6\text{e}2$. SI is tested with experimental ADF-STEM recordings of a Au-nanorod; see Figure 2. An image serving as ground truth was scanned with $I = 3.9\text{e}3$ and a second image with $I = 1.1\text{e}2$, with $N = 66\text{e}3$ and $\sqrt{c} \simeq 0$. From the latter image SI recordings were extracted with $p = 1/N$ and M ranging from $0.1N$ to $1.0N$ in ten steps. The settings are detailed further in [2].

Results

From the results for SD in Figure 2.a it is clear that $\text{DQE}_{\text{SD}}^{-1}$ matches MSE well and that both show the same optimum at $p = 0.1$. Figure 2.b shows two reconstructions for SI and in Figure 2.c the excellent agreement between $\text{DQE}_{\text{SI}}^{-1} \propto N/M$ and MSE is displayed.

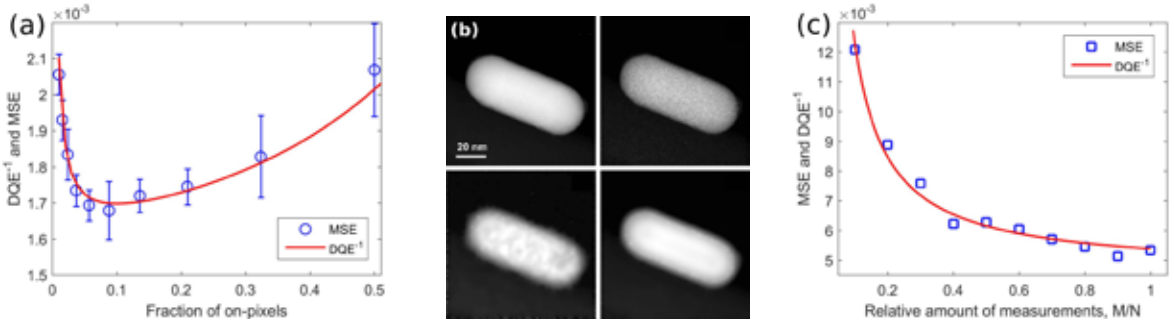

Figure 2: (*a*): SD result. $\mathrm{DQE}_{\mathrm{SD}}^{-1}$ and MSE vs. fraction p of on mirrors. p is spaced logarithmically to sample the region around the optimum better. (*b*): SI results. Experimental ADF-STEM data with the ground thruth image (upper left), the image at lower intensity (upper right), a reconstruction for $M = 0.1N$ (lower left), and a reconstruction for $M = N$ (lower right). (*c*): SI result. $\mathrm{DQE}_{\mathrm{SI}}^{-1}$ and MSE vs. number of measurements M.

The optimal values for p can be derived analytically from (2), yielding

$$p_{\mathrm{opt,SD}} = \frac{Mc}{NI\mu}\left(\sqrt{1+\frac{NI\mu}{Mc}}-1\right) \quad \text{and} \quad p_{\mathrm{opt,SI}} = \frac{1}{N}. \tag{3}$$

Discussion

The close correspondence of DQE^{-1} and MSE justifies the use of the analytically tractable DQE in establishing optimal experimental settings. Furthermore, in [2] close correspondence with the Fisher information in the recordings is shown. For SD $p_{\mathrm{opt,SD}}$ is heavily dependent on the read-out noise c, and, remarkably, in the absence of read-out noise $p_{\mathrm{opt,SD}} = 1/N$ despite the massive loss in recorded intensity. For SI $p_{\mathrm{opt,SI}}$ is always equal to $1/N$, independent of read-out noise.

Acknowledgments

WVDB: funding from the DFG project BR 5095/2-1. The Qu-Ant-EM microscope used for the experimental data was partly funded by the Hercules fund from the Flemish Government. AB and JV: funding from FWO project G093417N. CTK: funding from the DFG (CRC 951). We thank Prof. Luis Liz-Marzan for the Au nanoparticle sample.

References

[1] R. G. Baraniuk, IEEE Signal Processing Magazine, 24, 118–121 (2007)

[2] W. Van den Broek et al., IEEE Transactions on Computational Imaging, 1–1 (2019)

Ultrafast coherent manipulation of a free-electron wave function by electron-light quantum interaction

G. M. Vanacore

Institute of Physics, Laboratory for Ultrafast Microscopy and Electron Scattering,
Ecole Polytechnique Federal de Lausanne, Station 6,
CH-1015 Lausanne, Switzerland

E-mail: giovanni.vanacore@epfl.ch

Introduction

The interaction between light and electrons can be exploited for generating radiation, such as in synchrotrons and free electron lasers, or for controlling electron beams for the dynamical investigation of materials and molecules. Using electromagnetic fields the coherent control of an electron wave function can be pushed to unexplored timescales, enabling new applications in light-assisted quantum devices and diagnostics at extremely small timescales, such as those governing intramolecular electronic motions and nuclear processes.

In this contribution, I will describe a novel method for the coherent longitudinal and transverse phase manipulation of a free-electron wave function. Using appropriately synthesized optical light fields I will demonstrate how to modulate the energy, linear momentum and orbital angular momentum (vorticity) of the electron wave function with attosecond sensitivity.

Methods

A relativistic pulsed electron beam was made to interact with an appropriately synthesized electromagnetic field. The field was generated either by a sequence of two fs laser pulses reflected at the surface of a mirror (semi-infinite field), or by the coherent superposition of the surface plasmon polaritons (SPPs) optically-generated from nanofabricated structures (near field). The energy-momentum exchange resulting from the electron-field interaction was directly mapped via momentum-resolved ultrafast electron energy-loss spectroscopy in an ultrafast transmission electron microscope (UEM).

Results and discussion

First, we have demonstrated that it is possible to coherently manipulate the longitudinal phase of a free-electron wave function using a semi-infinite light field configuration composed of a sequence of two mutually phase-locked light pulses impinging on a mirror and delayed in time by fractions of the optical cycle [1]. The profile of the field resulting from such a temporal combination of pulses changes the energy and momentum of an electron as it traverses the interaction volume and provides direct access to the quantum nature of the electron–light coupling at optical frequencies.

In a more recent work [2], we have shown that, besides the longitudinal phase modulation, also the transverse electron's phase profile can be efficiently manipulated when using localized electromagnetic fields mediated by light-induced collective electronic modes (surface plasmon polaritons, SPPs). To demonstrate this effect, we have generated an ultrafast vortex electron beam by means of a spatially-confined optical field carrying Orbital Angular Momentum (OAM) as generated by the excitation of chiral SPPs. The formation of chiral plasmons relies on the spin-to-OAM conversion from circularly-polarized light in non-paraxial scattering from a nanoscale cavity and is a clear manifestation of the strong spin-orbit coupling of light when confined to subwavelength scales. The quantized inelastic coupling between a free-electron and such field configuration is thus responsible for an efficient transfer of a nonzero topological charge and helical phase distribution from the chiral SPP to the transverse profile of the electron wave function. For the first time, we were able to demonstrate the ultrafast generation of an electron vortex beam and the dynamic control of its vortex structure on the attosecond timescale using ultrafast chiral plasmonic near fields (see for instance Fig. 1 for an artist's impression of the process).

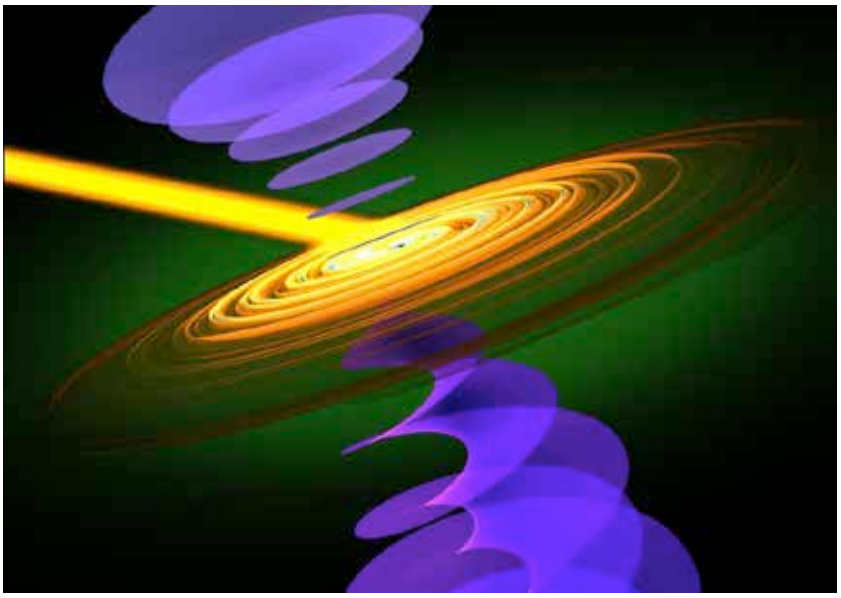

Fig. 1. Artist's impression of the ultrafast generation of an electron vortex beam and the dynamic control of its vortex structure using ultrafast chiral plasmonic near fields (credit: Ella Marushchenko - Ella Maru Studio).

The ability to access the phase profile of low-energy quantized plasmonic excitations directly resulted from the development of a new ultrafast time-domain holographic imaging technique, as described in detail in a very recent work [3]. With this method we were able to capture attosecond/nanometer-resolved phase-sensitive movies of rapidly evolving localized electromagnetic fields in plasmonic structures. Unlike conventional holography, where the signal and the reference are spatially separated and then recombined to interfere, in our method we use electromagnetic fields to split an electron wave function in a quantum coherent superposition of different energy states by means of spatially separated reference

and signal electromagnetic fields (Ramsey-type interference). In the image plane, spatial modulation of the electron-energy distribution reflects the phase relation between reference and signal fields. Beyond the obvious implications in the investigation of ultrafast coherent processes at the nanometer length scale, this approach allows implementing optically-controlled and spatially-resolved quantum measurements in parallel, providing an efficient and versatile tool for the exploration of electron quantum optics by accessing the quantum coherence of generic electronic states in a parallel fashion.

Conclusions

The potential of our approach for longitudinal and transverse phase modulation at the ultrashort timescale and below should pave the way to achieve unprecedented insights into non-equilibrium phenomena in advanced quantum materials, and should play a decisive role in the rational design and engineering of future photonics and electronics applications.

References

[1] Vanacore*, Madan*, Berruto, et al., Nature Communication **9**, 2694 (2018)

[2] Vanacore*, Berruto*, Madan, et al., Nature Materials https://doi.org/10.1038/s41563-019-0336-1

[3] Madan*, Vanacore*, Pomarico, Berruto, et al., Science Advances **5**, eaav8358 (2019)

Quantized Interaction of Free Electrons with Cavity Photons Stimulated by pJ Laser Pulses

Kangpeng Wang[1] Rafael Dahan[1], Michael Shentcis[1], Yaron Kauffmann[2] and Ido Kaminer[1*]

1. *Solid State Institute and Faculty of Electrical Engineering, Technion-Israel Institute of Technology, Haifa 32000, Israel*
2. *Department of Materials Science & Engineering, Technion-Israel Institute of Technology, Haifa 32000, Israel*

E-mail: kaminer@technion.ac.il

Abstract

We measure the quantized interaction of free electrons with cavity photons trapped in a thin photonic crystal slab, stimulated by laser pulses with energy as low as <0.1 nJ. The enhanced interaction enables the direct imaging of photonic crystal Bloch modes with deep subwavelength resolution, simultaneous with measuring the modes' lifetime and the entire photonic bandstructure.

Introduction

Ultrafast interactions of free electrons and laser pulses have enabled powerful imaging techniques to investigate ultrafast dynamics in transmission electron microscopy [1]. By using femtosecond (fs) laser pulses as pump and electrons as probe, one can image the electric field of light through photon-induced near-field electron microscopy (PINEM) [2-7]. The pump light creates an evanescent field around the sample and then the probe electrons interact with this field by absorbing/emitting multiple quanta of photons. Employing these energy-shifted electrons for imaging, the light-field around the nanostructure can be detected with fs temporal and subwavelength spatial resolution. Specifically, by also tuning the laser frequency, one can achieve laser-stimulated electron energy spectroscopy [6]. So far, the existing literature on PINEM focuses on the interaction with metallic or lossy structures (e.g., plasmonics), whose photonic excitations have short lifetimes, limiting their energy exchange with probing electrons.

Here, we propose and demonstrate for the first time the quantized interaction of free electrons with resonant cavities, utilizing the strong enhancement of the resonance modes for advance microscopy capabilities. We use such PINEM interaction to perform transmission nearfield optical microscopy (TNOM) of the resonance modes in a photonic crystal (PhC), with subwavelength resolution, simultaneously detecting their lifetime, and mapping their entire angular-spectral response (*i.e.*, the photonic bandstructure).

Results and Discussion

We stimulate the photonic resonance modes with fs laser pulses and use the free electrons to image the modes' spatial profile with subwavelength resolution. **Figure 1** presents the direct observation of the PhC Bloch modes with wavelength-, angle-, and polarization-selective excitation, imaged through the transmitted electron with subwavelength resolution. Our approach complements a different usage of free electrons for nearfield imaging by angle-

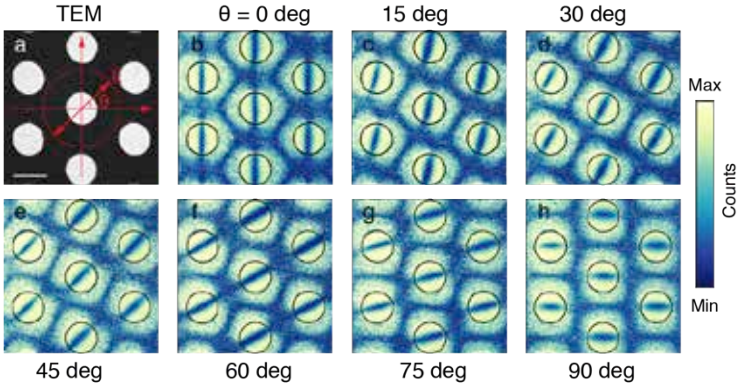

Fig. 1 Subwavelength imaging of optical Bloch modes in photonic crystals (PhC). (a) Transmission electron microscope image of the PhC triangular unit cell from top-view. The PhC is a 200 nm thick Si3N4 slab with 300 nm holes and 600 nm periodicity. The length of white scale bar is 300 nm. (b-h) Examples of laser-stimulated TNOM images showing the resonant (Bloch) modes in the PhC across the entire unit cell for a varying polarization. The optical pump laser is at 730 nm and normally incident onto the PhC slab (Γ-point). The angle of polarization, θ, is defined by the red arrows in (a).

resolved cathodoluminescence [8, 9], which can also infer the Bloch modes [8] and bandstructure [9] by measuring the local density of states (LDOS) at every point. Related structures have been studied in photonic waveguide geometries, and with subwavelength resolution by scanning nearfield optical microscopes (SNOM) [10,11,12].

Through the comparison with other nearfield optical techniques, let us emphasize several pros and cons of TNOM: On the one side, we can vary the polarization and angle of the excitation to select a *single* resonant mode (e.g., Bloch mode), image it also in vacuum (e.g., holes in the structure in **Fig.1b-h**), and detect fields buried deep inside the structure (as shown in [5-7]). Comparing with SNOM, TNOM can image without perturbing the nearfield of the nanophotonic system under investigation with the probing tips. On the other side, samples in transmission electron microscopes need to be thin for the electrons to penetrate them, which does not limit nearfield imaging with cathodoluminescence and SNOM.

Our experiments are performed on a dielectric PhC membrane (**Fig. 1a**) in an ultrafast transmission electron microscope. By tuning the wavelength and incident angle of fs laser pulses, we couple them into resonance bands of the PhC, thus achieving stronger electron-photon interactions. **Fig. 2a-i** show examples of Bloch modes we obtain with 200 keV electrons, whose higher energy enables penetration through PhC slab and integration over the hard-to-reach fields of the modes. We also observe how different Bloch modes at the Γ point can be excited by rotating the pump polarization, enabling us to observe the transformation from a pure TM mode to a pure TE mode (**Fig. 1b** vs **2h**).

The resonant cavity nature of the PhC modes allows us to use a much lower laser intensity than in previous reports [3-7] to create the quantized electron-photon interactions (<0.1 nJ pulse energy with ~100 μm spot diameter and ~200 fs pulse duration); corresponding to <0.1 mW pump power with 1 MHz repetition rate. Our method is especially important for power-sensitive nanostructures, which can be damaged by the heat of the pump laser during investigation. The resonant nature also means that the lifetimes of the photonic modes reach ps time scale (quality factor Q of thousands). Through our pump-probe we demonstrate the first direct detection of the lifetime of optical modes by the time-resolved scan. Furthermore,

we demonstrated the possibility to construct the entire PhC bandstructure for both TM and TE polarizations in **Fig. 2**. The mapping is done by scanning over the wavelengths and incident angles of the pump laser pulse (using ~4 mW) and analyzing the resulting electron energy-loss spectrum (EELS). The measured bandstructure corresponds well with our simulations.

To conclude, we demonstrate efficient quantized electron-photon interactions in resonant photonic cavities, with prospects for low power laser-stimulated electron energy spectroscopy and imaging.

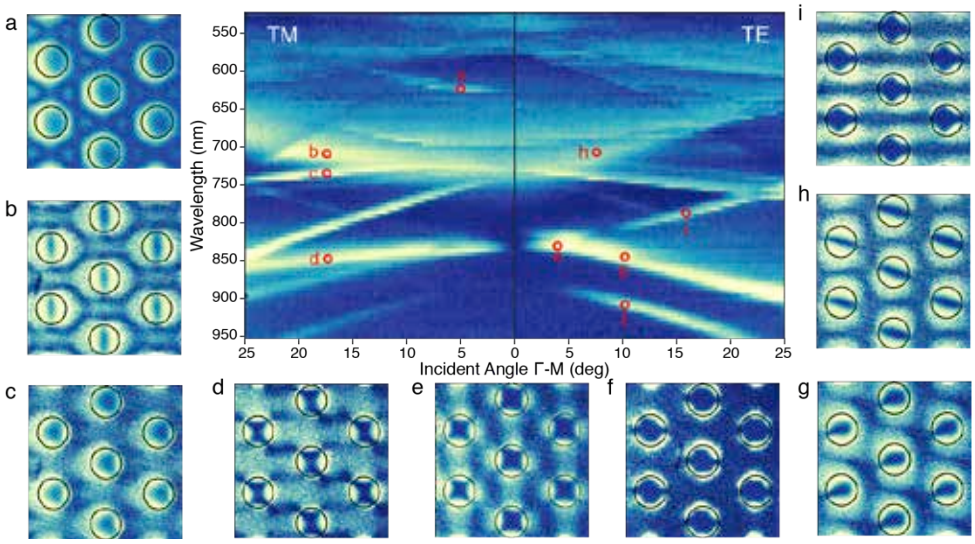

Fig. 2 Point-by-point mapping of the PhC bandstructure in ultrafast electron microscopy, scanning over laser incident angles and wavelengths. Each pixel is a separate PINEM measurement of the probe electron's energy-gain when it overlaps with the pump laser temporally and spatially. The color represents energy gain; brighter areas indicate coupling to higher Q PhC Bloch modes (limited by the laser's bandwidth, which is ~5-10 nm). (a-i) Nearfield images show the light-field distribution of TM (a-d) and TE (e-i) Bloch modes of the PhC triangular unit cell from top-view, marked by red circles on the bandstructure map.

References

[1] A. Zewail, "Four-Dimensional Electron Microscopy", Science **328**, 187-193. (2010)

[2] B. Barwick, et al., "Photon-induced near-field electron microscopy". Nature **462**, 902-906. (2009)

[3] A. Feist, et al., "Quantum coherent optical phase modulation in an ultrafast transmission electron microscope." Nature **521**, 200-203. (2015)

[4] Y. Morimoto and P. Baum, "Diffraction and microscopy with attosecond electron pulse trains." Nature Physics **14**, 252–256 (2018).

[5] L. Piazza, et al., "Simultaneous observation of the quantization and the interference pattern of a plasmonic near-field." Nat. Commun. **6**, 6407. (2015)

[6] E. Pomarico, et al., "meV resolution in laser-assisted energy-filtered transmission electron microscopy." ACS Photonics **5**, 759-764, (2017).

[7] G. M. Vanacore, et al., "Ultrafast Generation and Control of an Electron Vortex Beam via Chiral Plasmonic Near Fields", Nature Mater., (2019), Accepted.

[8] R. Sapienza, et al. "Deep-subwavelength imaging of the modal dispersion of light." Nature Mater. **11**, 781 (2012).

[9] S. Peng, et al., Probing the Band Structure of Topological Silicon Photonic Lattices in the Visible Spectrum, Phys. Rev. Lett. **122**, 117401 (2019).

[10] J. W. Fleischer, et al., "Observation of two-dimensional discrete solitons in optically induced nonlinear photonic lattices", Nature **422**, 147–150 (2003)

Orbital angular momentum and energy loss characterization of plasmonic excitations in metallic nanostructures in TEM

Matteo Zanfrognini[1,2], Enzo Rotunno[2], Stefano Frabboni[1,2], Alicia Sit[3], Ebrahim Karimi[3], Ulrich Hohenester[4], and Vincenzo Grillo[2]

[1]Dipartimento FIM, Università di Modena e Reggio Emilia, via G.Campi 213/a, I-41125, Modena, Italy

[2]CNR-NANO via G Campi 213/a,I-41125 Modena, Italy

[3]Department of Physics, University of Ottawa, 150 Louis Pasteur, Ottawa, Ontario K1N 6N5, Canada

[4]Institute of Physics, Karl-Franzens-Universitat Graz, Universitatsplatz 5, 8010 Graz, Austria

Email: matteo.zanfrognini@unimore.it

Introduction

Low loss EEL spectroscopy in TEM is one of the main techniques to study localized surface plasmon resonances (LSPs) in metallic nanostructures as it enables the mapping of the electromagnetic fields associated to these excitations with nanometric resolution [1]. In such experiments the measured physical quantity is the loss probability density function, as a function of the probe position on the sample: in this way the absolute value of the projection along the optical axis of the electric field associated to the excited plasmon can be accessed. This approach doesn't lead to a complete understanding of the symmetry properties of the plasmonic resonances, especially in the case of excitations with close energies and similar electric field distributions. This problem can be overcome by shaping the electronic wavefunction to match the symmetry of a given LSP, in order to detect only that peculiar mode while excluding other excitations without the required field distribution [2], but this approach requires a preliminary knowledge of the spatial properties of the modes of interest and it suffers a low signal to noise ratio. In our recent work [3] we study the LSPs symmetries by measuring both the energy and the orbital angular momentum of the electrons which have inelastically interacted with the metallic nanostructure: we have started from the theory exposed in [2] and we have computed OAM resolved loss functions within the non retarded

approximation [1], evaluating the spatial and spectral properties of the plasmonic modes through MNPBEM toolbox [4]. As a first example (Figure 1) we focus on the case of systems with cylindrical symmetry as nanodisks and we point out that a post selection in terms of the OAM immediately enables to classify LSPs according to their multipolar order. The post selection in OAM also permits to obtain more insight in the way in which the plasmon modes are modified, once the cylindrical symmetry is broken: as suggested in [5] the new plasmonic modes can be obtained by mixing LSP of the original cylindrically symmetric system to find new hybridized modes. We demonstrate that such mixing is effectively measurable by probing the OAM of the inelastically scattered electrons and so good control in the change of the plasmonic properties of a given nanostructure under morphing is available. Finally, as already exposed in [6], strong differences in the intensity of the loss functions corresponding to opposite OAM are expected in chiral assemblies of metallic nanostructures. Selecting the inelastically scattered electrons in terms of their OAM provides insights in the properties of chiral plasmonic nanostructures: in particular, a plasmonic nanostructure which should exhibit giant dichroism has been analysed (Figure 2). The work is supported by Q-SORT, a project funded by the European Union's Horizon 2020 Research and Innovation Programme under grant agreement No. 766970.

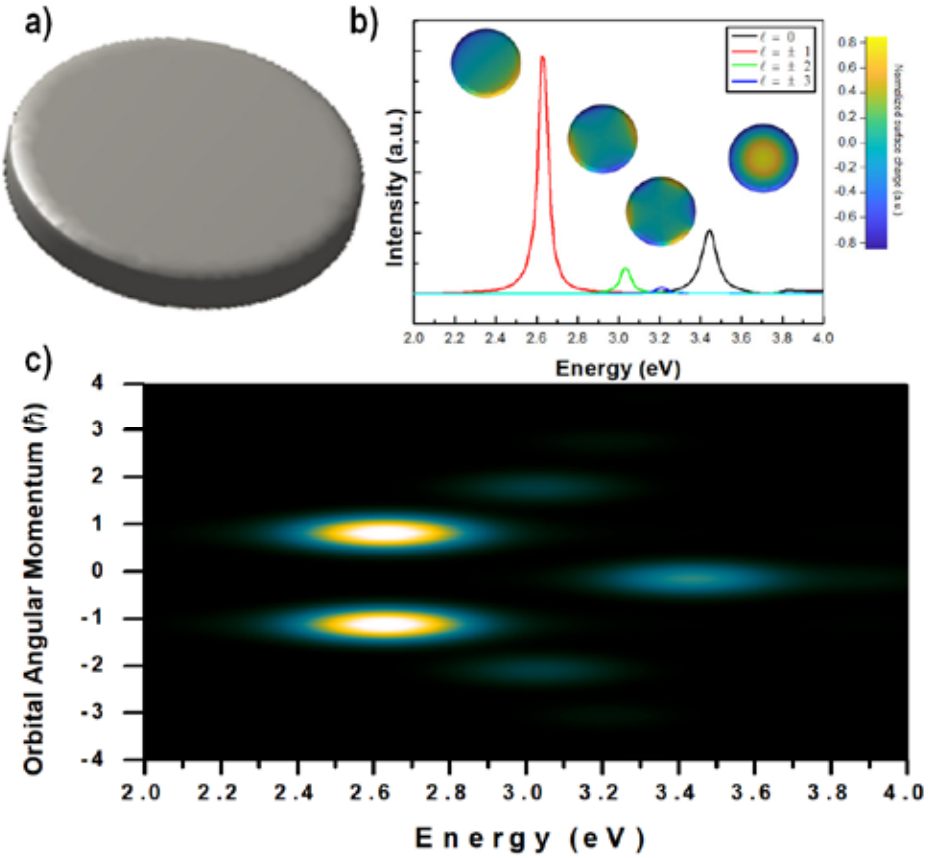

Figure 1. a) Tilted view of the Ag nanodisk. b) Simulated OAM-resolved EEL spectra for different OAM values (see legend). The surface charge distribution of each plasmonic mode is reported as an inset, where positive (negative) charge corresponds to blue (yellow) tone. c) 2D representation of the EEL spectra convoluted with a Gaussian function simulating the limited instrumental resolution ($\Delta E = 0.3eV$ and $\Delta \ell = 0.5\hbar$).

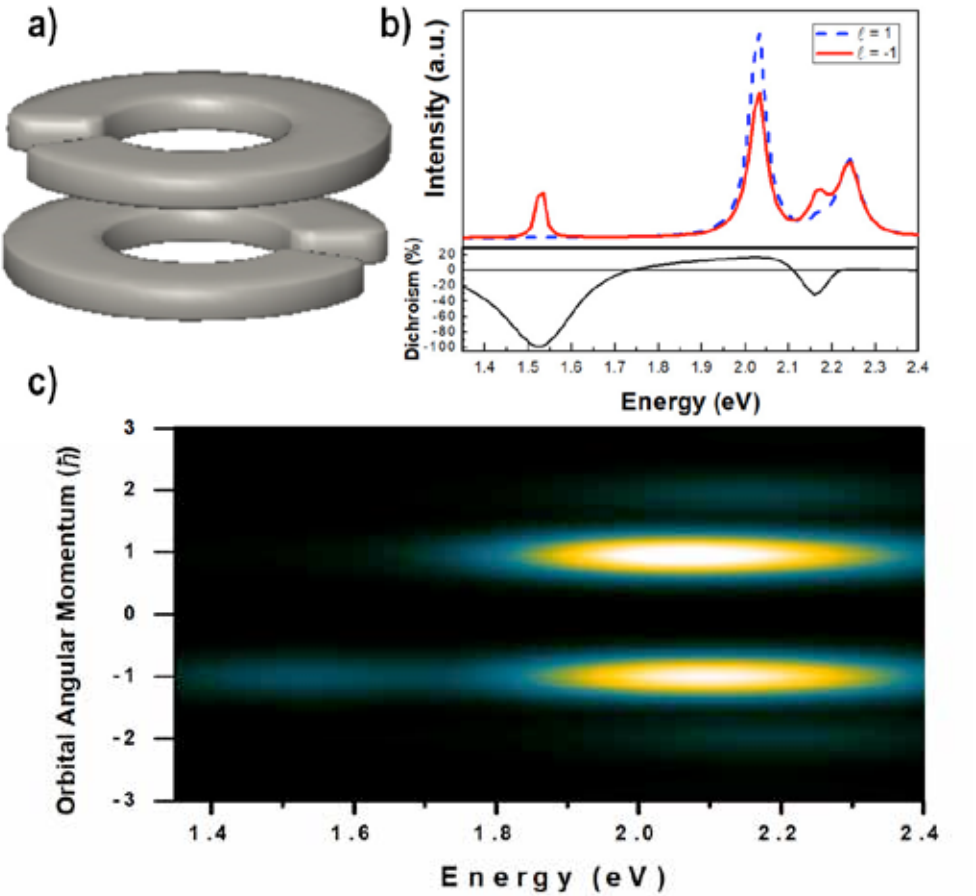

Figure 2. a) Tilted view of the chiral plasmonic structure. b) Simulated OAM-resolved EEL spectra for the $\ell = +1$ (blue dashed line) and $\ell = -1$ (red line) components: notice the presence of a peak only for $\ell = -1$ at 1.53 eV, which is responsible for a giant electron dichroism effect. c) 2D representation of the EEL spectra convoluted with a Gaussian function simulating the limited instrumental resolution ($\Delta E = 0.3eV$ and $\Delta\ell = 0.5\hbar$).It is immediate to observe, despite the experimental broadening, a very pronounced asymmetry between the signals for $\ell = +1$ and $\ell = -1$.

References

[1] F. Garcia de Abajo, *Rev. Mod. Phys.,* 82, 209-275, 2010

[2] G. Guzzinati et al., *Nat. Commun.,* 8, 14999, 2017

[3] M. Zanfrognini et al., *ACS Photonics*, *6* , 620–627, 2019

[4] U. Hohenester et al., *Comput. Phys. Commun.,* 183, 370-381, 2017

[5] F. Schmidt et al., *Nano Lett.,* 14, 4810-4815, 2014

[6] A. Asenjo Garcia et al., *Phys. Rev. Lett.,* 113, 066102, 2014

Spiral Phase Contrast Imaging in Cryo-Electron Microscopy

Yue Zhang[1], Vincenzo Grillo[2], Peter J. Peters[1], Raimond B.G. Ravelli[1]

[1]The Institute of Nanoscopy, Maastricht University, 6211 LK Maastricht, The Netherlands
[2]Institute of Nanoscience, National Research Council (NANO-CNR), Modena, Italy
E-mail: yue.zhang@maastrichtuniveristy.nl

Introduction

Frozen-hydrated biological samples are mainly composed of light elements which result in very low amplitude contrast and weak phase changes of the electron beam in cryogenic electron microscopy (cryo-EM). Traditionally, images are obtained at slight under focus to obtain phase contrast. Analogous to light microscopy, devices commonly referred to as "phase plates" have been developed to provide in-focus phase contrast. Here, we study the influence of the spiral phase plate (SPP) on the image formation model in cryo-EM by adding a phase-change $e^{il\Phi_k}$ which is angularly dependent to the exit wave in the Fourier space. The SPP can produce images with enhanced edge contrast, therefore better contrast at the sample borders. The results are compared with images without SPP under different foci showing that SPP strongly enhance the phase contrast near in-focus condition.

Methods

Image formation of biological samples in cryo-EM can be modelled using the specimen's scattering properties, the influence of optics and the detector response [1]. We calculated the specimen interaction potential using the isolated atom superposition approximation (IASA) which also takes account the solvent, ions and molecular interactions. A multislice algorithm was used to calculate the electron propagation through the specimen with the slice thickness at 1 nm [2]. The difference between the signal and noise transferring was included via the detective quantum efficiency.

The spiral phase plate was incorporated by introducing an angularly dependent phase changes $e^{il\Phi_k}$ to the electron wave in reciprocal space resulting in the wave function $\Psi(r) = \psi(r)e^{il\phi_k}e^{ik_z z}$ [3][4]. Here, l is the topological charge of the electron beam, and Φ_k is the angular coordinate. When $l = 1$, the value we used here, the phase angularly change from -π to π and it produces a spiral shape phase contrast transfer function [5]. By changing the defocus value, we studied the image contrast of the human H chain ferritin, with and without SPP. Simulated images were validated experimentally. The experimental data were acquired on a 200kV Arctica cryo-EM with a purposely built spiral phase plate inserted in the objective holder position. The SPP had been shaped using focus ion beam (FIB) milling of a Si_3N_4 film.

Results

Figure 1 shows simulated cryo-EM images of human apo-ferritin. In the absence of a phase plate, phase contrast is obtained by defocusing (Fig 1b, 1 μm underfocus) which provides

good low-spatial-frequency information compared to close-to-focus condition (Fig. 1a, 100 nm underfocus).

The simulated images with SPP are shown in Figure 1c and 1d. Fig 1c shows an image close to focus, Δf = 100 nm. The contrast in this image is much higher than that of the image without SPP (Fig. 1a). Figure 1d shows a simulated image with SPP at the same defocus as was used for Fig 1b (1 μm underfocus). Comparison of these two images shows the edge-enhancement properties of the SPP.

Figure 2 shows the contrast transfer function for the SPP, both in 2D (Fig. 2a) and in 1D (Fig. 2b) at different azimuthal angles. The three different CTF curves plotted in Figure 2b correspond to the lines shown in Figure 2a. For example, the blue line on the right side of the Thon ring illustrates the high contrast at low frequencies, corresponding to the dark area on the right side of Figure 1d. As a consequence, both low-frequency and high-frequency signals can be obtained in the same image at different azimuthal angles. When the defocus value is 1 um, the phase contrast is azimuthally varying which is indicated by the three different lines in figure 2d.

We also collected some experimental data with a SPP. Figure 3 shows an image collected at a defocus value of 100 nm. The contrast of protein edges is strongly enhanced with SPP, and it also shows an azimuthally-varying phase contrast.

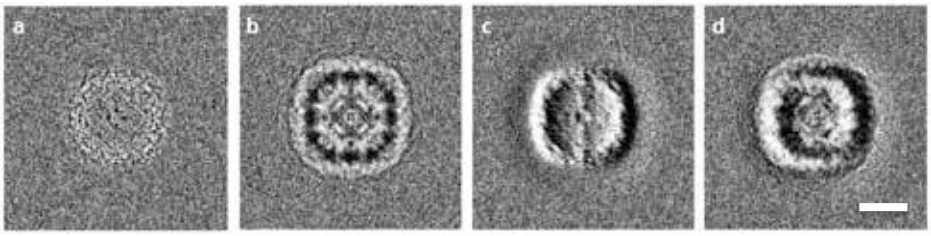

Figure 1. Image of human H-chain ferritin under different defocus values (a) without SPP, ∆f = 100 nm, (b) without SPP, ∆f = 1000 nm, (c) with SPP, ∆f = 100 nm, (d) with SPP, ∆f = 1000 nm. The scale bar corresponds to 5 nm.

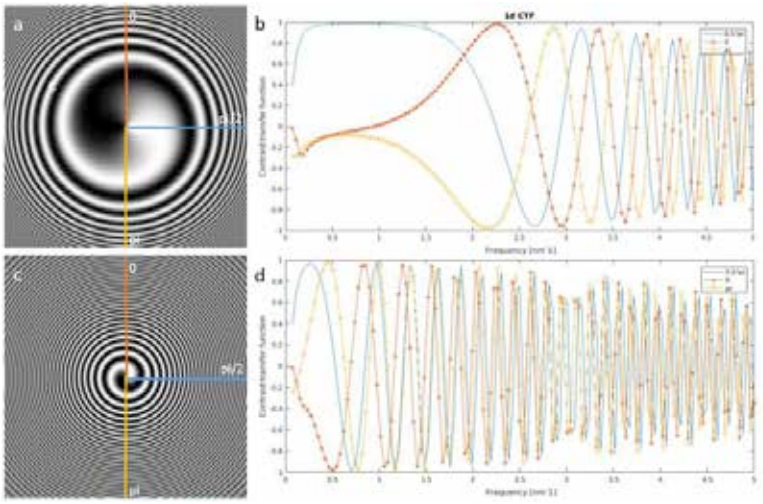

The acceleration voltage is 200 kV, integrated flux 40 e^-/A^2, the detector is Falcon III.

Figure 2. Thon ring and one-dimensional contrast transfer function (CTF) at different azimuthal angles (a)(b) in focus and (c)(d) under 1 um defocus with SPP.

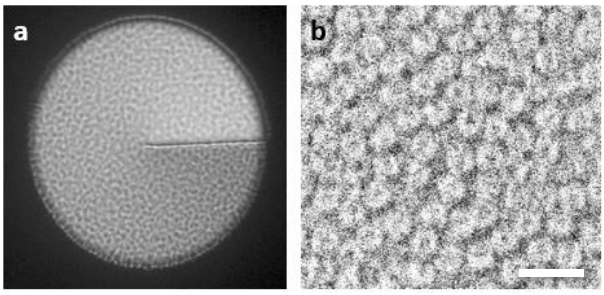

Figure 3. (a) The image of SPP with FIB milling Si_3N_4 film, (b) ferritin with SPP, Δf = 100 nm. The scale bar is 30 nm. The acceleration voltage is 200 kV, integrated flux 40 e^-/A^2 with Falcon III detector used in integration node.

Discussion

We investigate the use of a SPP for cryo-EM imaging of weak-phase frozen-hydrated biological macromolecules. Inserting an $l = 1$ SPP on the back focal plane of the electron microscope helps us to get a good phase contrast especially close to in-focus condition (Figure 1). The SPP adds a $e^{il\Phi_k}$ phase shift to the exit wave, resulting in an angularly dependent contrast transfer function and enhanced edge contrast. The simulation helps to understand the enhancement of the phase contrast by adding an SPP, as well as the optimization of the data acquisition. The experiment is done with Si_3N_4 SPP, illustrating the potential of SPP for edge enhancement. However, due to the scattering caused by the Si_3N_4, such phase plate will also introduce undesired scattering and increase noise. To overcome this, we also plan to do further experiments with magnetic spiral phase plate that will have less scattering effects.

References

[1] M. Vulović *et al.*, "Image formation modeling in cryo-electron microscopy," *J. Struct. Biol.*, vol. 183, no. 1, pp. 19–32, 2013.

[2] E. J. Kirkland, *Advanced computing in electron microscopy: Second edition*. 2010.

[3] L. Allen, M. W. Beijersbergen, R. J. C. Spreeuw, and J. P. Woerdman, "Orbital angular momentum of light and the transformation of Laguerre-Gaussian laser modes,", Optical Express 1992.

[4] R. Juchtmans, L. Clark, A. Lubk, and J. Verbeeck, "Spiral phase plate contrast in optical and electron microscopy," *Phys. Rev. A*, vol. 94, pp. 1–7, 2016.

[5] A. M. Blackburn and J. C. Loudon, "Vortex beam production and contrast enhancement from a magnetic spiral phase plate," *Ultramicroscopy*, vol. 136, pp. 127–143, 2014.

Towards a quantum electron microscope: Microwave based interferometer and resonator for electrons

Robert Zimmermann, Michael Seidling and Peter Hommelhoff

Chair for Laser Physics, Friedrich-Alexander-Universität Erlangen-Nürnberg, Staudtstraße 1, 91058, Erlangen, Germany
E-mail: robert.martin.zimmermann@fau.de

Abstract

We report on the development of a low-energy electron interferometer and resonator based on free electrons manipulated by microwave electric fields applied to micro-structured chips. The working principle is of a Paul trap: A microwave potential applied to electrodes causes an oscillating electric field by which electrons can be guided in a pseudopotential [1]. The transverse confinement provides discretized motional quantum states that govern the motion. Based on initial designs of electron guides [2-3], a more complex electrode structure, a beamsplitter, can be realized by going from quadrupolar to hexapolar fields [4].

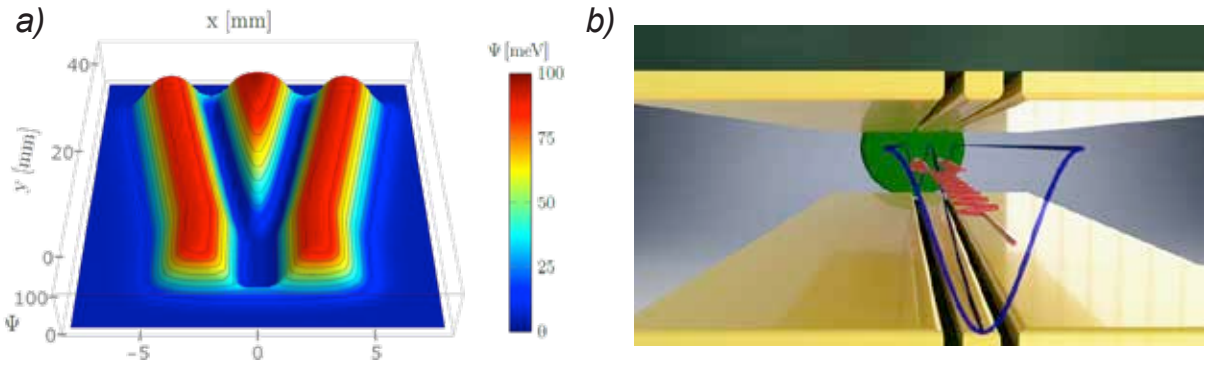

Figure 1: a) Calculation of the pseudopotential formed in the middle of the guide in the xy-plane parallel to the chip surface. The pseudopotential minimum at z=0 splits into two minima along z. b) Illustration of the working principle of the electron beam splitter: The golden surfaces are the planar surface electrodes on which a microwave potential is applied. The electron wave (displayed as the red line) is injected into the pseudopotential minimum (illustrated as the blue line) at the entrance. By following the form of the pseudopotential, the electron wavefunction is split transversely into two parts and detected at the detector after the guide (shown as a green circle).

By decreasing the beamsplitter splitting angle, we have developed an electron beam splitter that is predicted to split the electron wavefunction coherently and adiabatically, i.e., without noticeable excitation to higher-lying transverse quantum states. We will show our ongoing efforts to demonstrate this form of splitting. The electron optics are integrated into our existing setup to overlap both output beams and make interference fringes visible. The phase between laser-triggered electron pulses and the microwave field is controlled in a laser-triggered and

phase-synchronized SEM. Furthermore, simulations and preliminary results are presented for a new design for an electron resonator. It consists of a linear microwave guide, which confines an electron pulse transversely, and electron mirrors at both ends. The goal is to show interaction-free measurements with free electrons, which would pave the way for the development of the quantum electron microscope.

References

[1] W. Paul, Rev. Mod. Phys. **62**, 531 (1990)

[2] J. Hoffrogge, et al.; Phys. Rev. Lett. **106**, 193001 (2011)

[3] J. Hoffrogge and P. Hommelhoff; New J. Phys. **13**, 095012 (2011)

[4] J. Hammer, et al.; Phys. Rev. Lett. **114**, 254801 (2015)

[5] P. Kwiat, et al.; Phys. Rev. Lett. **74,** 4763(1995)

[6] W. P. Putnam and M. F. Yanik; Phys. Rev. A **80**, 040902(R) (2009)

Q-SORT Science Bash: Does God Play Dice?

Outreach event for schools

Thursday 04 July 2019, h. 11:20 — 12:30

Heinrich-Schliemann Gymnasium
Königstraße 105 — 90762 Fürth — Germany

(Outreach event for schools)

- **Miles Padgett**, Glasgow University (United Kingdom)

"Albert Einstein famously stated, in a 1926 letter to Max Born, that God "does not play dice with the universe". It was another way for him to say that he believed that physics should be able to provide a fully deterministic description of the universe, where given precise knowledge of the here and now, the future could be predicted. To use his own words, physics should be able to provide a "complete" description of the universe. This was Einstein's starting point in the criticism that he levelled at the then-recent theory of quantum mechanics, in the famous 1935 article by Einstein, Podolsky, Rosen. The ensuing rich debate lasted decades and indeed, in a sense, might be said to be still ongoing. Out of the debate came some fundamental insights into the still puzzling and paradoxical nature of quantum mechanics.
This talk is devoted to trying to explain the conceptual difficulties that quantum mechanics presents, Einstein's concerns and their experimental test.
I will also explain how some of our own work uses these concepts in the creation of new types of imaging systems, that improve upon classical limits."

Miles Padgett

About the speaker:

Miles Padgett holds the Kelvin Chair of Natural Philosophy in the School of Physics and Astronomy at the University of Glasgow. He heads an Optics Research Group covering a wide spectrum from blue-sky research to applied commercial development, funded by a combination of government charity and industry. He is also Vice-Principal for Research in the University with an office which strives to support both individual researchers in realising their own potential and the University's vision to deliver world-changing research. Miles is a Fellow both of the Royal Society of Edinburgh and the Royal Society, the UK's national academy. In 2008 Miles was awarded the UK Institute of Physics, Optics and Photonics Division Prize. In 2009 Miles was awarded the Institute of Physics, Young Medal "for pioneering work on optical angular momentum". In 2014 he was awarded the Kelvin Medal of the Royal Society of Edinburgh for his contributions to optics and his promotion of a global community of researchers. In 2015 he was awarded the Prize for Research into the Science of Light by the European Physical Society and in 2017 the Max Born Award of the OSA. His research group studies in the field of optics and in particular of optical angular momentum. Their contributions include an optical spanner for spinning micron-sized cells, use of orbital angular momentum to increase the data capacity of communication systems and an angular form of the quantum Einstein-Podolsky-Rosen (EPR) paradox.Miles is the Principal Investigator of QuantIC, the UK's Centre of excellence for research, development and innovation in quantum enhanced imaging, bringing together the six Universities with more than 40 industry partners.

Special Seminar: Making Open Science Work for You

Tuesday 02 July 2019, h. 16:30 — 17:15

Leuchs-Russell Auditorium
Max Planck Institute for the Science of Light
Staudtstraße 2 — 91058 Erlangen — Germany

- **Najla Retteberg**, University of Gottingen (Germany)
- **Tim Smith**, CERN (Switzerland)

This joint presentation will cover the importance of Open Science within research. It will explain how Zenodo works and how CERN is working to support Open Science. The presentation will also cover services for Open Science and the work of OpenAIRE within the context of European Commission Open Science policy.

About the speakers:

Najla Rettberg is the Scientific Manager of the OpenAIRE Advance. She is a librarian with extensive experience in open access, open science, e-infrastructures and digital preservation. An Arabist by training, she has also worked as a consultant for a range of institutions including King's College London, the Digital Preservation Coalition and OCLC.

Tim Smith is Head of Collaboration, Devices and Applications Group at CERN, the European Particle Physics Laboratory. Tim is an Open Science advocate leading initiatives at CERN and in the wider science community. He drove the launch of CERN's Open Data Portal to share Large Hadron Collider big data with the world, as well as the Higgs Boson webcast which shared its discovery live around the globe. He also instigated and nurtures Zenodo within the European Commission's OpenAIRE project as an open data service for world-wide science. Tim came to CERN at the end of the 80s, obtained a PhD in Particle Physics and performed research at the Large Electron-Positron accelerator for 10 years. He then joined the CERN IT Department to lead teams innovating in computing farm management and physics data management.

This is a Q-SORT outreach event
in collaboration with CERN and OpenAIRE

Participants

First Name	Last Name	Email	Company
Navid	Abedzadeh	navid@mit.edu	MIT
Akshay	Agarwal	akshayag@mit.edu	MIT
Harshith	Bachimanchi	ssharshith.bachimanchi@gmail.com	IISER Pune, India
Ulrike	Bauer-Buzzoni	ulrike.bauer-buzzoni@mpl.mpg.de	Max Planck Institute for the Science of Light
Armand	Béché	armand.beche@uantwerpen.be	EMAT - University of Antwerp
Moritz	Carmesin	moritz.carmesin@uni-ulm.de	Uni Ulm
Fu-Rong	Chen	frchen@cityU.edu.hk	City University of Hong Kong
Rafal	Dunin-Borkowski	r.dunin-borkowski@fz-juelich.de	Forschungszentrum Jülich
Dominik	Ehberger	dominik.ehberger@physik.uni-muenchen.de	Ludwig-Maximilians-Universität München
Armin	Feist	armin.feist@uni-goettingen.de	University of Göttingen
Javier	García de Abajo	javier.garciadeabajo@nanophotonics.es	Institut de Ciències Fotòniques (ICFO)
Luca	Giberti	lucagiberti@qedproductions.co.uk	QED
Moumita	Gosh	moumita.ghosh@thermofisher.com	Thermofisher
Avraham	Gover	gover@eng.tau.ac.il	Tel Aviv University
Vincenzo	Grillo	vincenzo.grillo@unimore.it	CNR (ITALY)
Giulio	Guzzinati	giulio.guzzinati@uantwerpen.be	EMAT, University of Antwerp
Tyler	Harvey	tyler.harvey@uni-goettingen.de	University of Göttingen
Peter	Hommelhoff	Peter.Hommelhoff@physik.uni-erlangen.de	University of Erlangen-Nuremberg
Philip	Jacob	philipjaco@gmail.com	Indian Institute of Technology Kharagpur
Cameron	Johnson	cwj@uoregon.edu	Department of Physics, University of Oregon
Ebrahim	Karimi	ekarimi@uottawa.ca	University of Ottawa
Aviv	Karnieli	avivkar1@gmail.com	Tel Aviv University
Felix	Kern	f.l.kern@ifw-dresden.de	IFW Dresden
Stewart	Koppell	skoppell@stanford.edu	Stanford University
Pieter	Kruit	P.Kruit@tudelft.nl	Delft University of Technology
Tatiana	Latychevskaia	tatiana@physik.uzh.ch	Paul Scherrer Institut
Gerd	Leuchs	gerd.leuchs@mpl.mpg.de	Max Planck Institute for the Science of Light
Sergey	Loginov	s.loginov@tudelft.nl	TU Delft
Penghan	Lu	p.lu@fz-juelich.de	Forschungszentrum Juelich
Alessandro	Marchetti	alexmar983@yahoo.it	Wikimedia
Kelly	Mauser	mauser@amolf.nl	AMOLF
Yoshie	Murooka	y.murooka@fz-juelich.de	Forschungszentrum Jülich
Miles	Padgett	Miles.Padgett@glasgow.ac.uk	University of Glasgow
Yiming	Pan	yiming.pan@weizmann.ac.il	Weizmann Institute of Science
Darius	Pohl	darius.pohl@tu-dresden.de	TU Dresden (DCN)
Albert	Polman	Polman@amolf.nl	AMOLF
Giulio	Pozzi	giulio.pozzi@unibo.it	Forschungszentrum Jülich
Raimond	Ravelli	rbg.ravelli@maastrichtuniversity.nl	Maastricht University
Manuel	Reinhard	reinhard@jeol.de	JEOL (Germany) GmbH
Najla	Rettberg	nrettbe@gwdg.de	Göttingen University
Paolo	Rosi	paolo.rosi@unimore.it	UNIMORE
Enzo	Rotunno	enzo.rotunno@nano.cnr.it	CNR-NANO
Raffaella	Santucci	raffaellasantucci@qedproductions.co.uk	QED
Thomas	Schachinger	thomas.schachinger@tuwien.ac.at	TU Wien / USTEM
Sebastian	Schneider	sebastian.schneider@ifw-dresden.de	IFW Dresden
Roy	Shiloh	roy.shiloh@fau.de	Chair of Laser Physics, FAU-Erlangen
Tim	Smith	Tim.Smith@cern.ch	CERN
Helmut	Soltner	h.soltner@fz-juelich.de	Forschungszentrum Jülich
Dongsheng	Song	d.song@fz-juelich.de	Ernst Ruska-Centre for Microscopy and Spectroscopy with Electrons Research Center
Nahid	Talebi	N.Talebi@fkf.mpg.de	Max Planck Inst. for Solid State Research
Amir Hossein	Tavabi	a.tavabi@fz-juelich.de	FZJ
Peter	Tiemeijer	peter.tiemeijer@thermofisher.com	Thermo Fisher Scientific
Luiz	Tizei	luiz.galvao-tizei@u-psud.fr	CNRS
Shai	Tsesses	tsesses@campus.technion.ac.il	Technion - Israel Institute of Technology
Wouter	Van den Broek	vandenbroek@physik.hu-berlin.de	Humboldt-Universität zu Berlin
Kangpeng	Wang	wangkangpeng@msn.com	Technion
TU	Wien	philipp.haslinger@tuwien.ac.at	Technische Universität Wien- Atominstitut
David N.	Winkler	dwinkler@udel.edu	University of Delaware
Matteo	Zanfrognini	186905@studenti.unimore.it	Consiglio Nazionale delle Ricerche
Yue	Zhang	yue.zhang@maastrichtuniversity.nl	Maastricht University
Robert	Zimmermann	robert.martin.zimmermann@fau.de	FAU Laserphysik

ッ